Western Australian School of Mines (WASM): Minerals, Energy and Chemical Engineering

Ore-Body Delineation using Borehole Seismic Techniques for Hard Rock Exploration

Felix Menu

This thesis is presented for the Degree of
Doctor of Philosophy
of
Curtin University

December 2018

Declaration

To the best of my knowledge and belief this thesis contains no material previously published by any other person except where due acknowledgment has been made.

This thesis contains no material which has been accepted for the award of any other degree or diploma in any university.

Signature: 

Date: 12th December 2018

Abstract

Globally, the exploration for and exploitation of mineral resources is moving to greater depths. To meet the ever-increasing demand for base metals requires the use of advanced imaging technologies to supplement the traditional exploration methods to provide improved lateral and vertical resolution of deep seated ore-bodies for targeted mining. Accurate geological model improves mine design and ore extraction. Hence in the last decade we witnessed an increased frequency in the application of 3D seismic reflection method. Where there exist elastic impedance contrasts between the ore-body and the surrounding rock units the imaging power of this method exceeds any other geophysical technique. However, in number of cases surface seismic is faced with the task of imaging sub-vertical structures in an overly complex geological environment. This is practically impossible to achieve from the surface unless very strong velocity gradient is present which is rarely found in a hard rock environment. An alternative way of forming images of steeply dipping complex structures is to utilize boreholes. This study investigates the potential of the crosshole seismic reflection technique to provide high-resolution and high-quality data in complex geological environments and at greater depths that can be used for ore delineation and improved reserve estimate. The same approach could be utilized to de-risk mine development such as shaft placement and design of underground working by imaging fine structures and faults that can be hazardous to such operations.

The number of available crosshole survey case histories is vanishingly rare. The results produced were clearly not sufficient to inspire more frequent application of this method for mineral exploration objectives. Hence the main objective of this study is to demonstrate the true potential of this method and in that way promote its further development through subsequent field studies.

To evaluate the potential of crosshole reflection imaging I designed an extensive set of numerical geological models that are all based on the well-known exploration and mining cases studies. Where possible, the numerical results were evaluated against

field studies. The power of the crosshole imaging approach is compared to much more established 3D surface seismic and Vertical Seismic Profiling results.

To achieve the objectives set in this study, I considered several geological cases involving mineral deposit of the Yilgarn Craton-type (Western Australian) and Rosebery-type (Tasmania). Each of the modelled deposits has one or a combination of the following geological factors: (i) regolith preventing useful high frequency information being recovered; (ii) highly conductive banded iron formation hosted barren sulphide unit in the proximity of steeply dipping and/or deep seated target; (iii) dipping conductive targets concealed by thick, conductive black shale horizon; (iv) deposits located in areas with severe topographical issues; (v) steeply dipping and buried massive sulphide ore-bearing structures; and (vi) buried, low-volume high-grade localized deposits. All of the selected cases challenge the performance of any known geophysical method.

Numerical simulation of these models produced often excessively complex results that involved testing different processing and imaging strategies in order to recover initial geology. These extensive studies enabled me to properly evaluate crosshole method and infer its strengths and weaknesses. The results point to the high potential of this method and the necessity for its further development through field application. I hope that this study will inspire geophysical and mining community to utilize this method to help discover down-dip extensions of the known mineralized bodies and in that way expand mining operations and prolong mine life.

Acknowledgements

First and foremost, I would like to thank the Ghana Education Trust Fund (the GETFund) for the sponsorship for this programme. I remain forever grateful to you.

Associate Professor Milovan Urosevic, I wish to express my heart-felt gratitude to you for taking me to the end of this research. You have been very instrumental and provided useful suggestions since your Assistant supervisory time. Whenever I approached you, even your smiles and words of encouragement alone made me to keep going strong in this journey.

Professor Anton Kepic, even-though you were unable to see me through to the end, I am grateful to you for your positive criticism, continual advice, motivation and knowledge which provided the momentum for me to push through this research work.

Dr. Andrew Greenwood, my Assistant Supervisor, you have been of immeasurable help to me. Even before you became official member of my supervisory panel, you were available to offer your assistance. Through you I have gained a lot more field experience. I would like to thank you also for the technical editing.

Dr. Eric Takam Takougang, I am grateful to you. Apart from official duties as my onetime Assistant Supervisor, you were much concerned of my total wellbeing for which I will remember you.

And you, Dr. Christian Dupuis, all started with you. You were so much approachable and accommodating and always ready to listen and attend to any problem I brought to you irrespective of the time and nature of the problem.

I gratefully acknowledge Mr. Mike Whitford of Independent Group NL for his assistance with the VSP data acquisition and other pieces of information provided on McLeay magmatic nickel sulphide deposit. I also gratefully acknowledge the assistance of MMG Limited and HiSeis Pty Ltd for pieces of information provided

on Tasmania Rosebery VMS deposit and in the provision of petro-physical data which were used to help constrain my Rosebery VMS modelling.

This work has been supported by the Deep Exploration Technologies Cooperative Research Centre (DET CRC) whose activities are funded by the Australian Government's Cooperative Research Centre Programme.

My thanks go to DECO Geophysical (RadExPro) and Tesseral Technologies Inc. for provision of software under their University licensing agreement programmes.

To both the academic and non-academic staff of the Department of Exploration Geophysics, I say thank you for assisting me in diverse ways. My very good friend, Dr. Henny Suzana Mediani and the family, I owe you a lot of gratitude. My colleagues, especially Muhammad Shahadat Hossain, Kevin Kai Fu Ung, M. Javad Khoshnavaz, Mohammed Ali Garba, Zubair Ahmed, and Mateus Meira, you are amazing. Beyond supporting each other by deliberating over our problems and findings, we also happily talked about things other than just our papers.

To my wonderful family members, both close and external, and my little boy Aseye, in particular, whom I have left at such a tender age, and all my well-wishers, it is your prayers that have sustained and led me this far. Thank you for being there for me.

Table of Contents

Table of Figures

List of Tables

List of common abbreviations and definitions used

3C	Three component geophone
AGC	Automatic gain control
BIF	Banded iron formation
CDP	Common depth point
CSR	Crosshole seismic reflection
CUU	Central Ultramafic Unit
CUU-FV	Central Ultramafic Unit-Felsics volcanics
DAS	Distributed Acoustic Sensing
DHTEM	Downhole time-domain electromagnetic
DNiS	Disseminated NiS
EUU	Eastern Ultramafic Unit
FBP	First break pick
FD	Finite difference
FE	Finite element
FPRB	Fully-populated receiver borehole
FV	Felsic volcanics
FVU	Felsic Volcanics Unit
FWI	Full Wave Inversion
FWS	Full Waveform Sonic
HR	Host rock
MHM	Maggie Hays Main
MHN	Maggie Hays North
MNiSM	Massive NiS mineralization
MVSP	Multiple/multi-offset VSP
NiS	Nickel sulphide
OVSP	Offset VSP
PSDM	Pre-stack depth migration
PSTM	Pre-stack time migration
RVSP	Reverse VSP
RFE	Radio Frequency Electromagnetic
SNR	Signal-to-noise ratio

TEM	Time-domain electromagnetic
UM	Ultramafic
UM/B	Ultramafic-basalt
Vp	P-wave velocity
Vs	S-wave velocity
VMS	Volcanogenic/volcanic-hosted massive sulphide
VSM	Virtual source method
VSP	Vertical Seismic profile/profiling
VSP-CDP	Vertical seismic profiling to common depth point
WUU	Western Ultramafic Unit
WVSP	Walk-away VSP
ZVSP	Zero-offset VSP

1. General Introduction

1.1. Prologue

Mining is the process of extraction of mineral deposits from the surface or beneath the surface of the earth. This activity represents one of man's earliest undertakings reaching back into Palaeolithic times. More so, it is an activity that has been undertaken worldwide throughout history (Bell and Donnelly, 2006). As such, it has played an important role in civilization development. In spite of this early activity, Telford et al. (1990) and Azcue (1999) noted that the first ever scientific record of mining and its associated search for metals was dated in 1556 by Georgius Agricola exposition publication named *De re Metallica*. The dependence of primitive societies on mineral products is evidenced by the terms Stone Age, Bronze Age, and Iron Age. These terms refer to a sequence of ages that indicate the increasing complexity of the relationship between mining and society (Bell and Donnelly, 2006). With time, the uses of minerals have increased in both volume and variety to meet the expanding thirst and a greater range of purposes by society. Every material object in society can be claimed to be either directly derived from a mineral or is produced by means of mineral derivatives such as steel, energy or fertilizers (Bell and Donnelly, 2006). The mining industry provides direct and indirect employment to a large number of people.

While the above points are true, the raw materials are finite. To meet ever-increasing demand, conscientious efforts are being made to increase the number of discoveries as cost effectively as possible. This involves turning our attention to unconventional deposits that are less attractive to mining including steeply dipping ore-bearing structures situated at greater depths and small but high-grade ore deposits located at intermediate and great depths.

Over recent years, seismic methods have emerged as potential geophysical imaging tools for mineral exploration and exploitation. Different seismic methods and techniques have since advanced for this purpose, such as high resolution 2D and 3D surface seismic, Vertical Seismic Profiles (VSP), and crosshole surveys. In general, surface seismic can provide us with good quality 2D and 3D images. Borehole based

methods, VSP and crosshole geometry, provide us with a shorter wavelet and, therefore, with better resolution by recording data closer to the target. This avoids partial (in the case of VSP) or full (in the case of crosshole geometry) devastating effect of the near surface onto our wavelet. However, since both methods are tied to boreholes the images produced are limited in spatial extent. But obtaining high-resolution surface seismic data to delineate ore-bodies under some geological environments can be a challenge. VSP application is equally challenged in some similar cases. This is often caused by geometrically-induced blind illumination zones characteristic for 2D and even 3D surface seismic and conventional VSP surveys (Urosevic, 2000). Under such environments, crosshole seismic reflection (CSR) could be an alternative technique to acquire high-quality and high-resolution seismic data to image the subsurface ore-bearing structures. Crosshole seismic surveys provide us with an ideal case where both sources and receivers are placed close to the target under investigation. Such recording geometry produces by far the highest resolution out of all seismic methods. Seismic waves are excited in one borehole and wave disturbances are received in the adjacent borehole, possibly not far away to retain the signal quality and, as we will see later, to reduce imaging uncertainties. For a practical application, a crosshole seismic survey is required to provide a cost-effective image of complex geological structures at depth. While this seems like a straightforward solution to accurately delineate our targets there are many caveats that need to be addressed and overcome. Consequently, case histories involving crosshole seismic in the mining sector are vanishingly rare. Various issues accompanying crosshole seismic surveys need to be addressed, analyzed and well understood for crosshole seismic technique, particularly when implemented in the reflection mode to become a viable exploration technology for exploration of mineral resources. For this reason, I embarked on the road of investigating the potential of crosshole seismic reflection surveys for ore and mineral exploration by analysing several, geologically well-defined mineral deposits through a series of numerical experiments. The simulations of crosshole seismic reflection surveys presented in this work are hoped to form the basis for future work and eventually be adopted and integrated into the local and global hard rock exploration tools for exploring specific types of ore deposit.

1.2. Why and when crosshole seismic reflection (CSR)?

The current trend of increasing demand for ore resources is confronted with the decline of most of economic mineral deposits. Moreover, the rate of discoveries of a highly profitable giant or even large size near-surface ore deposits is in a sharp decline. In addition, the trend of exploration and exploitation of mineral resources is moving to greater depths (Schodde, 2011). Conscientious efforts are being made for applying new methods and advancing technology to explore for deeper targets as well as delineating small but high-grade ore deposits at all depths. Potential field methods (gravity and magnetics), along with electrical and electromagnetic (EM) methods have traditionally been the main geophysical tools to identify mineral deposits. However, the resolution of these methods is generally low and reduces with depth. The situation is made worse where deposition of ore-bodies has occurred below conductive horizons. Drilling is another exploration tool but is expensive and the risk of not intersecting economic deposits is high. In increasingly complex environments at greater depths, acquiring high-resolution and higher-quality data is a common challenge for the application of familiar, surface geophysical methods in mineral exploration (Malehmir et al., 2012).

In recent times, tuned versions of the century-long hydrocarbon exploration seismic methods adapted to hard rock environments have emerged as technique capable to provide high-resolution images at depths where potential field methods fail. However, highly heterogeneous regolith, inaccessibility due to thick vegetation cover, difficult mountainous terrain, old workings and/or current mine operations are likely to make the application of surface seismic challenging. The CSR technique seems a better alternative to surface seismic and vertical seismic profiling under such conditions. CSR survey requires the availability of only two boreholes (at a time) and can be applied in restricted areas. Using the boreholes, both the source and receivers are placed below the weathered layer in competent rock. In brown fields numerous boreholes may already be available and safe to implement downhole surveys such as CSR. This will of course come at some extra cost but this method has the potential to provide very high resolution, higher signal-to-noise ratio (SNR), and precise imaging due to waves not travelling through the regolith. Enabling data generation and recording at depth below the regolith, the CSR geometry minimizes

degrading of the wavelet, reduces the amount of seismic energy scattering and attenuation, and generation of other unwanted wave types (surface waves, air blast, etc). Also, the geometry enables the use of higher frequency energy source. Thus, higher frequencies can be captured to provide high-resolution images of the subsurface structures. The technique is therefore capable of delineating tiny but economically viable ore deposits that would be transparent to other seismic methods due to lack of resolution and unfavourable geometry. Indeed, in some regions such as Western Australia, we frequently encounter very rich volcanogenic massive sulphide (VMS) deposits of very limited lateral extent but of a complex shape, often steeply dipping due to their association with various structures (Urosevic et al., 2012). Clearly crosshole seismic geometry may be favourable for detecting and imaging such deposits. Another interesting application may involve imaging below the boreholes for the detection of any faults and discontinuities that may jeopardise shaft placement or advancement of mine workings. To achieve these tasks, several survey optimizations including processing and imaging improvements need to be accomplished. The reflection images can be formed at depths below the instrumented borehole segments. Hence, even shallow boreholes, typically available in abundance in brown fields, may be deployed to provide images of deeper structures. Such an approach will also overcome issues often faced with access restrictions and obstacles such as tailing dams, dumps, and mine infrastructure. The CSR technique could be more cost-effective in such cases. The issue of the size of the imaging plane or area remains. Hence the implementation of crosshole seismic cannot be persuaded without proper investigations or de-risking studies. Hence my investigations include several deposits including small-volume high-grade nickel sulphide and VMS deposits where CSR may be effective and economically viable approach for imaging.

1.3. Research directions and methods

As briefly discussed, high-grade but small size deposits may be transparent to many geophysical techniques including surface seismic. In such cases the use of CSR could be investigated. Alternatively, CSR and VSP techniques may be combined to improve target illumination. VSP can be used also in reverse mode (receivers on the surface and sources down the borehole) in which case it is referred to as reverse VSP.

The objective of this research is principally directed towards investigation of the potential of the CSR method for mineral exploration. However, some imaging aspects of its more familiar "cousin" VSP are also analyzed in relation to the imaging aspects of the two methods.

The use of CSR to image ore deposits is very rare. The question is why? Is it too expensive and/or too difficult to use? Is it impractical? Does it provide any useable information? This research is aiming to give answer to most if not all of these questions. I believe one of the possibilities is that the method has been rarely used and that these questions were never thoroughly addressed. Even-though many trials were conducted over 20 years ago in hard rock mines with results showing different levels of success (and some results not encouraging at all), many of these results were not published in open literature but in project reports. For example, as contained in Fullagar et al. (1996; 1996a), "Application of Geophysics to Mine Planning and Operation, 1996 AMIRA Project P436" results were not published in open literature but in project reports. The reports are on geophysical methods for exploration of Australian VMS deposits mainly in Scuddle (Western Australia), Hellyer and Rosebery (Tasmania), and Mt Isa Mines (Queensland). But the geophysical prospecting methods employed mainly include induced polarization (IP)/resistivity, gravity/magnetics, and electromagnetics including crosshole tomographic Radio Frequency Electromagnetic (RFE) methods for resolving ore-body boundaries, and hence establishing ore continuity between drill-holes. In a subsequent section, I elucidated that the scanty report available on crosshole seismic application in hard rock environments is even skewed towards crosshole tomography than crosshole seismic imaging. Hence of my particular interest is to investigate the applicability of CSR for imaging deeply seated, complex mineralized bodies where other geophysical technologies are less effective or completely ineffective.

Alongside this, I need to investigate the geometry of survey, relationship of borehole distribution and deviation path with respect to the ore geometry, source and receiver disposition, their spatial separation, fold, recording parameters, etc. Imaging algorithms need to be analyzed and optimized as well as their analysis in terms of efficiency and imaging quality. The principal imaging technique I will be using is based on the Kirchhoff integral solution (Dillon, 1978) as it provides high flexibility

when it comes to the recording geometry. It is also well suited for imaging highly complex geology; that is, it can utilize a highly complex velocity field for imaging.

All the investigations will be conducted through numerical experiments. Only then we can truly assess the potential of CSR imaging method for exploration of mineralized targets that may be missed or difficult to delineate by any other geophysical technologies. I hope that the results of my study will encourage more frequent use of CSR in mineral exploration practice. This will also allow us to fully evaluate this method through the future case histories. This would require many different data sets due to vastly different geological settings, alterations, reflectivity, crosshole orientation and geometry and many other factors. Hence this work is only the beginning of the road towards finding the right role of crosshole seismic methods in mineral exploration practice.

1.4. Early seismic applications in hard rock environments

Contrary to its application in the hydrocarbon search, seismic techniques are not routinely applied in hard rock mineral exploration. The geological structure, lithology and depositional environment for oil and gas differ vastly from hard rock environments, as such, the petroleum seismic methodologies cannot be directly applied to mineral exploration. Typically, hard rock environments comprise of igneous and metamorphic rocks, they often have very complex geological structures including a high number of steeply dipping to vertical faults and structures, alterations, fractures, granitic intrusions, shear zones, a varying thickness heterogeneous layer and rugged topography (Harrison, 2009; Greenwood et al., 2010). Such environments have a combination of effects that absorb, distort, and scatter seismic energy (Harrison, 2009). While absorption of seismic energy causes attenuation of the seismic signals (Hardage, 1992; Mari and Coppens, 2003), distortion and scattering of seismic energy in hard rock environments complicate processing and interpretation of seismic data (Harrison, 2009). In addition, hard rock units in contact often exhibit, invariably, similar elastic properties with no significant velocity and density contrasts. Lack of significant velocity and/or density contrast, result in low reflectivity from rock boundaries of interest (Salisbury et al., 1996), posing a challenge to seismic data processing, imaging, and interpretation

(Greenwood et al., 2010). For these obvious reasons the acceptance and full application of the seismic reflection method by the mining industry has been slow, although the potential of the method has long been acknowledged by several authors (Malehmir et al., 2012).

Most early published works of hard rock seismic exploration are from the 1980s. Notable among them are surveys conducted in South Africa, Canada, and Australia, with a few other investigations from European countries.

In South Africa, early hard rock seismic exploration involved the collection of a large volume of a two-dimensional (2D) vibroseis data acquired across the Kaapvaal Craton by Anglo America Corporation from 1983 and beyond. The results showed a high level of success with the method but the data were found inadequate to resolve shallow, more complex structure(s) (Campbell, 1990; Pretorius et al., 2003). Other early works include: the most likely first approach by Pretorius et al. (1989) to integrate seismic and petro-physical data to image main geologic structures in the South African Witwatersrand Basin, the first ever 3D seismic survey for mineral exploration and mine planning conducted in 1987 (Campbell and Crotty, 1990), a low fold 3D survey carried out in the Witwatersrand basin to seismically image known faults in the mining operation to within three meters and, possibly, the first time in seismic mineral exploration where seismic attributes were employed to enhance the image of faults in the processed seismic data (Stuart et al., 2000), and a research into 3D seismic imaging of a gold ore-body at Vaal Reef Gold mine (Pretorius et al., 1997). Some other seismic activities conducted in South Africa and Botswana are documented by some other authors such as Larroque et al. (2002), Haslett (1994), Stevenson et al. (2003), and Cosma et al. (2007).

Among the early studies with seismic imaging in Canada were those on the near-surface sedimentary hosted mineral deposits (Wright, 1981), faulted and sub-horizontal fracture environments in the Canadian Shield for nuclear waste sites characterization (Green and Mair, 1983), and for base metal exploration in the eastern part of Canada (Wright et al., 1994). As part of the Lithoprobe project, Salisbury et al. (1996) carried out intensive petro-physical laboratory measurements (to study P-wave and density relationships) of common sulphides and crystalline

rocks. The laboratory measurements revealed strong reflective character of massive sulphide deposits against their host rocks (Salisbury et al., 1996; Salisbury et al., 2003). This singular finding spurred the application of seismic reflection method in search for sulphide-bearing ore deposits in Canada and other aforementioned parts in the world. Other seismic activities in Canada include an extensive research on 3D methods done to image nickel-copper deposits on the Sudbury Igneous Complex (Milkereit et al., 2000), a large survey undertaken to confirm the presence of massive sulphides through the Manitouwadge Greenstone belt, Ontorio (Petrie and Salisbury, 2003; Roberts et al., 2003), and the first reported successful 3D seismic delineation of a blind massive sulphide deposit in the Halfmile Lake area at about 1.2 km depth (Matthews, 2002). Some other high-resolution seismic surveys conducted in Canada include 2D exploration surveys at Shea Creek (Gyorfi et al., 2007) and McArthur River (White et al., 2007), and 2D and 3D seismic profiles acquired over Flin Flon mining camp (Malehmir and Bellefleur, 2010; Cheraghi et al., 2011; White et al., 2012).

From available information, Europe has witnessed early demonstrations of (both refraction and reflection) seismic methods. A lot of seismic methods were employed extensively in a number of the then Soviet Union (USSR) countries to study crystalline basement, investigate ore deposits and map vertical structures (Malehmir et al., 2012). In Sweden, the seismic reflection method was applied to image faults and fracture zones within the Precambrian crystalline rocks in the Finnsjon area (Juhlin et al., 1991), and to characterize radioactive waste storage sites (Juhlin, 1995). Furthermore, the method was used to study large-scale structures hosting mineral deposits as well as to provide seismic reflection profiling in the Urals (Juhlin et al., 1995). Still in Sweden, successful experiments were carried out over other granitic rocks (Juhlin and Palm, 1999). In Finland, between 2001 and 2005, a high-resolution reflection seismic data for ore exploration were acquired under the Finnish reflection seismic experiment, FIRE, Projects (Kukkonen and Lahtinen, 2006; Kukkonen, 2011a). Similar high-resolution seismic survey projects were undertaken under project code named “high resolution reflection experiment”, HIRE, between 2006 and 2010. As part of the outcome, the result of the seismic data motivated the deep-drilling programme at the Outokumpu site (Kukkonen et al., 2011b).

In Australia, there has been significant research into the application of 3D seismic surveys for coal mining (Urosevic et al., 1992; Hatherly et al., 1994) and the Southern Sydney Basin coal experiment to study propagation of seismic wave as applied to seismic imaging (Urosevic, 2000). Through the efforts of Geoscience Australia over some years now, thousands of kilometres of 2D seismic refraction profiles and deep crustal seismic reflection data were acquired, some across major mineral outlying areas such as Mount Isa in Queensland, Eastern Goldfields province in Western Australia, and in Tasmania. In the 1990s, several 2D regional seismic lines were conducted in the locality of existing gold mines in the Yilgarn Craton (Drummond et al., 2000). These surveys were under the sponsorship of Geoscience Australia (GA) and the Australian National Seismic Imaging Resource (ANSIR). From these results, 2 km deep structures suitable for mesothermal fluid flow and gold mineralization were imaged. However, the data were found inadequate to resolve shallow, more complex structure(s) of interest necessary for mineral exploration (Stolz et al., 2004). This observation was attributed to the acquisition parameters and processing procedures employed. A follow up high-resolution survey conducted in 2002 with dense acquisition parameters and with improved data processing procedures focused on targeting shallow structures. Results indicated strong reflections associated with complex stratigraphy from a shallow depth of about 200 m to a required depth and were in agreement with detailed geological sections constructed from drilling and mining data (Urosevic et al., 2005). Encouraged by these results, the earlier data were re-processed and re-analyzed. The quality of the re-processed data was vastly improved albeit limited by the sparse acquisition parameters. Later, at the request of Barrick Gold, other seismic exploration activities were performed across Sunrise Dam gold mine. Again, structural features of high-resolution were imaged and interrelated well with several years of drilling and geological information.

In 2004, the M363 Project was initiated by the Centre of Excellence for High Definition Geophysics (CHDG) in the Exploration Geophysics department, Curtin University of Technology. This was supported financially by the Western Australia State Government through Minerals and Energy Research Institute of Western Australia (MERIWA), with sponsorship from four gold mining companies. The experimental programme acquired approximately 150 kilometres of high-resolution

2D seismic data that crossed six gold mines in the Yilgarn Craton. The purpose of the surveys was to seismically image gold-bearing complex structures in the depth range of 100-1500 m within the mines vicinity (Urosevic and Evans, 2007; Urosevic et al., 2007). In 2006, a 2D high-resolution seismic line was acquired across the Archaean greenstone stratigraphy hosting the Prospero and Tapinos nickel sulphide deposits in Western Australia. This was sponsored by Jubilee Mines and the CHDG and monitored by Southern Geoscience Consultants (SGC). The research project was experimented for nickel exploration and aimed to test the seismic response in a complex hard rock environment in the presence of high ambient noise definition below Prospero in the depth range of 500 m to 2 km. The resulting seismic images showed reflection events down to 4 km which appear to be associated with the main geological features (Meyers and Uroservic, 2007).

After these break throughs, a few more mining companies were encouraged with the outcome of this seismic exploration and, in turn, supported larger scale 2D and 3D seismic surveys within Kambalda and Norsemen-Agnew-Wiluna provinces of the Yilgarn Craton Greenstone belt. Harrison and Urosevic (2008) and Harrison (2009) reported using seismic and sonic log data to characterize rock for mineral exploration. There was an extensive study on 3D seismic reflection survey on Lake Lefroy, Kambalda region, aimed towards direct targeting of nickel sulphide and the mapping of complex, deep structures associated with Kambalda Dome which yielded very impressive results (Urosevic et al., 2012).

Along the line of its implementation, the CHDG programme has diversified in the types of ore and mineral deposits to target (e.g., gold, diamonds, nickel, zinc, iron ore, copper, and uranium) (Urosevic et al., 2007). Now under the Deep Exploration Technologies Cooperative Research Centre, DET CRC[1], research is focused on advancing, in general, integration of seismic techniques and a range of geophysical methods for mineral exploration in hard rock environments (Urosevic et al., 2017).

[1] The DET CRC was established in 2010 under the Australian Government's CRC program. The CRC program provides funding to build critical mass in research ventures between end users and researchers to deliver significant economic, environmental and social benefits across Australia (open source, www.tetcrc.com.au). All the CRCs across Australia have been established to address major challenges that require medium to long-term collaborative efforts.

1.5. Borehole seismology in hard rocks

High-resolution seismic data can be obtained if it is possible to acquire the data below the highly attenuating and scattering regolith zone typically found in ancient hard rock environments. In hard rocks near surface zone comprised of transported sediments referred to as regolith can be excessively complex resulting in very high scattering, loss of high frequencies due to absorption, mode conversion, mode splitting, etc. This fact, to some extent, inspired the investigations of hard rock borehole seismology.

The vertical seismic profiling (VSP) method is frequently used in oil sector and is becoming more used in the mineral sector although most frequently in its simple form, which is zero-offset geometry or ZVSP. For this implementation only one source position, close to the borehole mouth is used in recording. When the energy source is deployed in the borehole and the receivers deployed along the surface, the method is termed reverse VSP (RVSP). A comprehensive literature review of VSP can be found in Hardage (1983) and Hinds et al. (1996). The usefulness of VSP, the various types of surveys such as zero-offset, offset and walk-away VSPs, and advancement made in its applications are widely published for example by (Hardage, 1983; Balch and Lee, 1984; Christie et al., 1995; Hinds et al., 1996; Mari and Coppens, 2003; Blackburn et al., 2007; Mari et al., 2011).

A formal definition of crosshole seismic borehole (Hardage, 1992) assumes the case where both down-hole source(s) and down-hole receiver(s) are deployed in different boreholes, which is the focus of this research and looked at in more detail in the subsequent subsection of this chapter. Another borehole imaging technique is the virtual source method (VSM). This involves the use of two boreholes, each having receivers deployed in them, and sources at the surface. As the seismic wave passes both boreholes, the signal recorded in the first borehole is used as a virtual source for the propagation of the seismic wave to the second borehole (Bakulin and Calvert, 2004; 2006). In another consideration where both the source points and receiver locations are in the same borehole, the technique is termed single-well seismic imaging (Chabot et al., 2002). Crosshole method in its conventional specification utilizes only two boreholes. With fast development of the Distributed Acoustic

Sensing (DAS) this conventional thinking may be revisited and changed in the future.

As in surface seismic, borehole seismology has been predominantly developed and applied in search for hydrocarbon deposits more so than in mineral exploration. Only a few publications discuss its application in hard rock environment. The technique has also been developed and applied for engineering and environmental purposes including waste disposal. With the single-well seismic imaging, Hornby (1989) utilized an experimental acoustic well-logging tool which was equipped with one monopole source and a multi-receiver sonic tool to image near-borehole features to a distance of 18 m from the borehole wall. Chabot et al. (2002) used the conventional well-logging tool to examine the acoustic and elastic wave propagation in and around an open borehole for reservoir characterization. Enescu et al. (2003) carried out VSP investigations at Olkiluoto site, Finland, for detailed site investigation programme for the final disposal of spent nuclear fuel. A 3-component geophone chain and VIBSIST-1000 – a time-distributed swept-impact source that produces signals with levels of energy comparable to explosives – were used for VSP surveys. Pretorius et al. (2011) employed 3-components (3C) downhole sensors to acquire a high-resolution VSP data so as to utilize both the P- and S- reflected waves in attempt to obtain high-resolution images with improved resolution over surface seismic data. Greenwood et al. (2010) demonstrated the use of hydrophone arrays as an alternative to 3C shuttles to generate high-resolution images away from a borehole wall and with a resolution comparable to that of a 3C data. Using similar approach, Greenwood et al. (2012) noted that the S-wave converted at the borehole wall to a pressure wave could be collected for use by the hydrophone receivers. These experiments by Greenwood et al. (2010) and Greenwood et al. (2012) also included measures to suppress cable and tube waves. Few other (successful) applications and challenges in the use of VSP in mineral search are captured by Malehmir et al. (2012).

1.6. Crosshole seismic surveying

As implied in conventional seismic surveying, “crosshole or crosswell seismic surveying” is used to describe four discrete stages of crosswell seismology. They

are: survey planning and design, acquisition, processing, and interpretation of crosswell seismic data. In general, crosswell seismic surveying falls under borehole seismic surveying with a source-receiver geometry quite similar to that of Fessenden's 1917 patented work. A more general description of crosswell seismology and crosswell seismic surveying are captured by many authors such as Stewart (1991), Hardage (1992), and Mari and Coppens (2003).

The development and application of crosswell methods may benefit from availability of numerous, closely spaced (less than 50 m) boreholes in proximity of a known target or above a deeply seated and yet unknown mineralization. In crosshole seismic surveying for mineral exploration, inter-borehole spacing for any two adjacent boreholes to utilize can be as short as 25 m and as wide as over 100 m (Rowbotham and Goulty, 1993; Cosma and Enescu, 2003; Enescu et al., 2003; Greenhalgh et al., 2003) and possibly to 200 m (Enescu et al., 2003). The choice for boreholes separation should be informed by the purpose of the survey and, therefore, the downhole source to be used. They should, however, be separated enough to enable separation of wavefields (Enescu et al., 2003). In its conventional application for imaging inter-borehole space, crosswell source-receiver geometry permits generated seismic signals to travel a short distance from the source to the receiver in the subsurface thus preserving the signal wavelet character from much deformation and with high energy level (Stewart, 1991). As mentioned earlier, by placing the shot and receiver locations below the strongly attenuating near surface zone, much higher frequency energy source can be employed leading to exceptionally high-resolution data acquisition (Hardage, 1992; Mari and Coppens, 2003). The dominant frequency in crosshole surveys can be an order of magnitude higher than encountered in surface reflection seismic.

Crosswell seismology has two related aspects: crosswell tomography and crosswell seismic reflection methods. Hardage (1992) refers to tomography as any image reconstruction method based on calculating a series of line integrals of some image-sensitive parameter through the region of interest/space of observation. The basic idea behind tomographic imaging is the ability to use the data measured outside an object to deduce the interior properties inside that object (Stewart, 1991). Tomography is well established in medicine (radiology) and other sciences such as

biology, global geophysics, plasma physics, astrophysics, and material science. In exploration geophysics, tomographic imaging uses seismic energy sources that generate seismic waves for probing a geological target of interest. The technique is standard in crosswell (usually the preferred term used in hydrocarbon sector) analysis and it is also being used for velocity analysis with surface or borehole or both data (Stewart, 1991). On the other hand, if the imaging processing technique of the subsurface geology involves the use of scattered and reflected wavefields and other late arrivals then the method is called crosswell seismology (Hardage, 1992) or crosswell reflection imaging (Li, 1994). Whether crosswell tomography or crosswell seismic reflection, Sheriff and Geldart (1995) referring to Wong et al. (1987), Rutledge (1989), and Lines (1991) stated the objective of crosswell studies is to learn about the region between the boreholes. A number of authors including Herman (1980) and Deans (1983) have provided historical background of tomography but its development relevant to geophysics is given by Stewart (1991). CSR method on the other hand can provide information not only between the boreholes but also from much greater depths, far below the total depth of the boreholes utilized for the survey. CSR can also utilize inverted tomographic velocity field to form an initial reflection image (Urosevic, 2000), subsequently updating the field in an iterative manner.

The development of crosswell seismic took place virtually alongside VSP development from around the 1910s. Reginald A. Fessenden's patented method and apparatus applied in 1917 for locating ore-bodies can be quickly linked to the present day crosswell reflection method and seismic. However, it was not until the 1950s that first crosswell seismic surveys trials were performed in Colorado, United States of America, by Ricker (1953) and McDonal et al. (1958), and in France by Bois et al. (1972). Their work seems to be the earliest attempt to combine crosswell acquisition geometry technique with that of tomographic inversion for seismic imaging. Crosswell seismic research, in both crosswell tomographic inversion from direct arrivals and crosswell reflection imaging to correlate geology, have been concentrated largely in oilfield development, coal-seam delineation, and in geotechnical engineering studies. It has a long history and many examples of successful applications. A detailed account, based on the above mentioned areas, has been provided by Li (1994). Good examples of use of crosswell imaging with

tomography and migration applied to field data for hydrocarbon related search were presented by Cai and Schuster (1993) and Qin and Schuster (1993). Enescu et al. (2003) carried out crosshole investigations. alongside VSP, at Olkiluoto site, Finland, for site investigation programme in crystalline rocks for nuclear fuel disposal. A hydrophone chain and VIBSIST SPH54 – a piezoelectric borehole source based on the Swept Impact Seismic Technique of Park et al. (1996) which operates on the same principle as the surface VIBSIST source – were used for the crosshole surveys. Both tomographic inversion and reflection imaging were done for the crosshole survey. Reflection imaging outside the crosshole area was performed using what they referred to as Image Point migration technique.

From available literature, there is no significant report on crosshole (usually the preferred term in mineral sector) seismic application in hard rock environments. The scanty report available is (even) skewed towards crosshole tomography than crosshole seismic imaging. I provide below a collation of some of the available reports.

Cao and Greenhalgh (1995) successfully delineated ore lodes with crosshole tomography using 240 m deep boreholes separated by 28 m. Greenhalgh et al. (2000) performed both crosshole tomography and VSP reflection imaging at the underground Hunt mine in Kambalda, Western Australia. They successfully delineated ore lodes with the tomographic approach but not so successful with reflection VSP imaging. Noranda Technology Center acquired a crosshole data over massive sulphide ore deposit in Ontario, Canada, with the aim of delineating the boundaries of a shallow ore-body between two slanting boreholes using both traveltime tomography and seismic reflection techniques (Meng and McGaughey, 1996). It was found out that both traveltime tomogram and the migration image showed satisfactory results, however the migration imaging produced a more reliable image of the ore-body. Even then, the sharpness of the pre-stack depth migration image was found low and could not accurately represent the actual boundaries of the ore-body. Furthermore, the migrated image of the ore-body did not intersect the borehole walls. Wong (2000) conducted crosshole seismic tomography test survey of a near-surface, thick, steeply dipping massive sulphide ore-body at the McConnell site, Canada, using first-arrival times. A high-resolution tomography image was

obtained but the high level of success associated with this has been attributed to the massive nature of the deposit and its relatively simple geometry. With three pairs of near vertical diamond drill-holes, Cosma and Enescu (2003) employed a piezoelectric source – VIBSIST SPH54 seismic source – and a string of 24 hydrophones for p-wave velocity tomography and crosshole reflection surveys for inter-borehole imaging of massive Ni-Cu sulphide mineralization at Voisey's Bay, Labrador, Canada. The reflection imaging technique was based on Image Point transform (Cosma et al., 2002; Cosma et al., 2010).

My research is not concerned with the geological cases where surface seismic is likely to be effective. Rather I am looking into specific case histories that potentially could only be resolved with the use of CSR method. This, perhaps, is the case when CSR is likely to be a cost-effective method in gathering geological information of vital importance for delineation of deep targets and hence extension of mining operations and, therefore, prolong mine life. De-risking shaft placement and underground workings could be also addressed by the application of the CSR method.

1.7. Terminology

Many terms have appeared in the geophysical literature to describe the geometry involved in data acquisition whereby the seismic signals generated in one borehole is measured in the second borehole. Various terms such as "borehole-to-borehole", "crosshole", "cross-borehole", "interwell", and "crosswell" are commonly used. While the terms such as "well", "crosswell", and "interwell" are usually referred to in the hydrocarbon and coal exploration – "well" mainly adopted because of the relative large size of the drill-hole, terms such as "borehole" and "crosshole" are usually used in mineral exploration – "hole" mainly referring to the small size of the diamond drill-hole compared to that of the hydrocarbon search. Nevertheless, the terms can be and are being used interchangeably. And until now in this manuscript, the terms have been used interchangeably.

From now on in this thesis, the terms "borehole", "borehole-to-borehole", and "crosshole" will mostly be adhered to. Also, in this thesis, I will refer to the image

reconstruction approach as the crosshole seismic reflection method or, simply, crosshole seismic reflection or CSR.

Direct or forward or normal approach: The term "direct approach" or "forward approach" or "normal approach" as used in this thesis describes synthetic CSR data acquisition geometry whereby the source borehole is located up-dip the slope of a dipping reflector and the receiver borehole located down-dip the slope.

Reverse approach: Similarly, the term "reverse approach" as used in this thesis refers to the synthetic CSR data acquisition geometry whereby the receiver borehole is located up-dip the slope of a dipping reflector and the source borehole located down-dip the slope.

1.8. Thesis configuration

The thesis is composed of seven chapters, configured in the following order.

Chapter 1. Summarizes the state of current knowledge of seismic methods with respect to their application in the mining sector. The motivation and research methodology of this research is outlined. Some terminological terms conclude the chapter.

Chapter 2. This chapter recalls the principles of reflection seismology and discusses how ore-body resolution dependency factors turn to favour crosshole geometry. The chapter highlights the importance of forward modelling and utilization of synthetic data. The concept of the origin of reflection points in crosshole seismic reflection is demonstrated. Also, the chapter discusses crosshole seismic reflection data processing and the imaging algorithm employed in this work.

Chapter 3. The chapter discusses some general characteristics of hard rock environment suitable for the application of crosshole seismic reflection. Some perceived factors influencing crosshole seismic reflection ore-body image recovery are also pointed out. Kinds of mineral deposits located in Australia to be examined with crosshole seismic imaging in the thesis are highlighted in this chapter.

Chapter 4. This chapter deals with the plausibility of the crosshole seismic reflection as hard rock exploration tool. To be used as a tool for reflection seismology, discussion on the method will involve its ability to record, discriminate, and separate out different wavefields. Then the imaging capability of the method will be tested by comparing its pre-stack depth migration images with those of multiple-offset VSP for known structures associated with McLeay magmatic nickel sulphide mineralization.

Chapter 5. The Maggie Hays nickel sulphide type ore-body delineation with crosshole seismic reflection will be looked at. With synthetic results, the effect of source-receiver boreholes location on the extent of target surface area and depth recovery will be examined.

Chapter 6. This chapter discusses the application of crosshole seismic reflection to delineate Rosebery volcanogenic massive sulphide (VMS) ore lenses. First, Rosebery ground conditions response to crosshole seismic reflection will be tested. For economical purposes, source-receiver boreholes separation and source density effects on crosshole geometry resolution will also be tested. Then, the capability test of the crosshole seismic reflection method to image cluster of VMS ore lenses in a complex geology will end this chapter.

Chapter 7. This chapter presents the general summary, discussions and conclusions of this research. A number of suggestions are made for future consideration to improve the crosshole seismic reflection imaging capability for hard rock exploration.

The manuscript ends with a full list of cite references followed by appendices.

2. Principles of crosshole seismic reflection for hard rock exploration

2.1. Introduction

Reflection and transmission of seismic energy at the interface assumes continuous and approximately planar interfaces. However, the interfaces in hard rock environments are seldom planar but rather characterized by abrupt structural and lithological changes and frequent discontinuities at all scales which will produce excessive scattering of the incident seismic energy (Keary and Brooks, 1991). The reflectivity of hard rocks is still not fully understood. Apart from the "conventional" impedance difference, the reflectivity seems to be also caused by other factors such as fine textural changes, alterations, and micro alignments of different origin (Urosevic et al., 2017). Very high reflectivity of shear zones often observed in Yilgarn Craton (Greenwood, 2013) remains unexplained as it is not supported by sonic log measurements. Tuning effect and/or anisotropy are thought of two most probable causes.

2.1.1. Seismic application for hard rock exploration

Until recently, geophysical exploration for ore and mineral deposits has not generally incorporated seismic techniques as hard rock environments were considered unfavourable for reflection seismic due to complex geology and low acoustic impedance (Salisbury et al., 1996). However, to detect reflection event above background noise requires a minimum reflection coefficient of 0.06 (Yilmaz, 2001). The main issue is the geological complexity of hard rock environments, then sparse borehole information and hence lack of calibration and rare petro-physical measurements rather than lack of reflectivity (Salisbury et al., 2003). Measurements of densities and velocities of a large suite of common silicate and mafic rock samples of known composition show that, generally, the average velocities of the silicate and mafic rocks increase with density, but the velocities and densities of the mafic rocks tend to increase more with increase in metamorphic grade. Measurements made to compare the velocity and density values of ore minerals and their host rocks show

that ore minerals could have substantial higher density values and a wide-range of velocity values than their host rocks (Salisbury et al., 1996). A plot of velocity values of the various rock types against their density values using Nafe-Drake curve (Nafe and Drake, 1963) is shown in Figure 2-1. Clearly the velocities of silicate and mafic rocks tend to increase with density with the Nafe-Drake curve (Salisbury et al., 1996). It was also noticed that reflection coefficient of 0.06, the minimum value equivalent to an acoustic impedance contrast of 2.5 x 10^5 g /cm^2s in mafic rock unit (Z = 20 x 10^5 g/cm^2s) and felsic rock unit (Z = 17.5 x 10^5 g/cm^2s), with the Z-values indicated by lines of constant acoustic impedance in Figure 2-1, is sufficient enough to give strong reflections between felsic and mafic rock layers (Salisbury et al., 1996; Salisbury et al., 2003). With the modern 32-bit instruments and very high data fold this condition could be further relaxed.

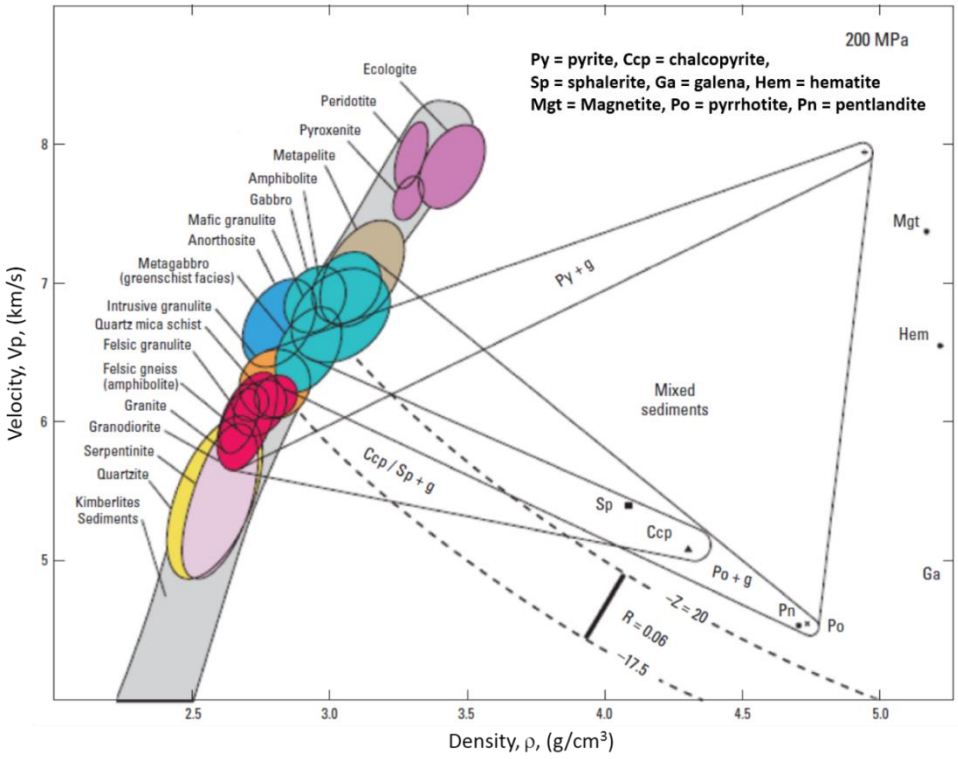

Figure 2-1: P-wave velocity versus density plot for common crystalline rocks and ores at 200 MPa confining pressure. Lines of constant acoustic impedance (Z) and the Nafe-Drake curve (shown in grey) for common rock types are superimposed within field. The constant acoustic impedance for felsic (Z = 17.5 x 10^5 g/cm^2s) and mafic rocks (Z = 20 x 10^5 g/cm^2s) are shown as dotted lines; an impedance contrast of 2.5 x 10^5 g/cm^2s cause a reflection coefficient R = 0.06, a minimum value required to give a significant reflection. On the velocity-density cross-plot, g stands for gangue. (The figure is modified from Salisbury et al. (1996), Salisbury et al., (2003), and Salisbury and Snyder (2007)).

Velocity and density values of sulphide-bearing ore minerals were found to have variable velocities ranging from around 8000 m/s for pyrite, to around 4680 m/s for pyrrhotite, with respective specific gravity values in the vicinity of 5020 kg/m^3 and 4630 kg/m^3 (Salisbury et al., 1996). Figure 2-1 also displays Vp-density relationship for common sulphides. Salisbury et al. (2003) noticed that the sulphides lie far to the right of the Nafe-Drake curve in the Vp-density fields and are controlled by the end member properties of pyrite, pyrrhotite, chalcopyrite, sphalerite, pentlandite, hematite, galena, and magnetite. The far right side locations on the Nafe-Drake curve of the sulphides in the Vp-density fields is caused by the high density which, in turn, is induced by the mean atomic weight of their constituents minerals (Wyllie et al., 1958; Birch, 1961; Eaton et al., 2003). Noticed also on the Vp-density fields that the massive sulphides rich in a noneconomic sulphide mineral–pyrite tend to have higher velocities with increasing densities whereas pyrrhotite-chalcopyrite, and sphalerite-dominated massive sulphides typically have velocity values that decrease with increasing density (Salisbury et al., 1996; Salisbury et al., 2003).

The above studies provide good guidance for the seismic exploration of mineral deposits (Salisbury et al., 1996). The acoustic impedances and elastic properties of massive sulphides differ substantially from those of most common host rocks. Hence using seismic reflection technique in different modes, adjusted to the specifics of the target, it should be possible to detect massive sulphide deposits at all scales (Salisbury et al., 2000; Salisbury et al., 2003). This prediction has been confirmed by surface seismic and VSP case histories (Salisbury et al., 2000; Salisbury et al., 2003; Malehmir et al., 2012). Direct detection of VMS deposits is also possible through utilization of specialized interpretation techniques (Urosevic et al., 2012).

In simplistic terms ore-body delineation with seismic reflection techniques depends on the vertical and horizontal resolution. Vertical resolution, with respect to seismic waves, can be considered as how far apart, in time or space, two interfaces must be to be seen as separate reflectors (Sheriff, 1978; Sheriff and Geldart, 1995; Salisbury et al., 2003). In ideal situation, the minimum "layer" thickness, h_{min}, required is predictable from the quarter-wavelength criterion (Widess, 1973), given as:

$$h_{min} = \frac{1}{4}\lambda = \frac{v}{4f} \qquad \textbf{(Eq- 2.1)}$$

where λ is the dominant wavelength of the seismic wave, v is the seismic velocity and f is the dominant frequency of the wavelet. For a given formation velocity (v), a reflector considered to be of small thickness at a certain frequency may not be considered same at a higher frequency. As the source(s) and receivers are placed below the most weathered layer in crosshole geometry, the geometry enables the use of higher acquisition source frequencies. From equation (Eq-2.1), the higher the frequency of the source, the higher the resolution of the target. While the reflector's thickness cannot be varied, data acquisition source frequency can be varied or increased by using higher acquisition frequencies.

In reality, the resolving power of a "noisy" seismic data is 1/3 to 1/2 of the dominant seismic wavelength. Surface seismic resolution in hard rock environments is generally on the low side. There are two reasons for it: very high rock velocity and attenuative near surface (regolith). In Yilgarn, Western Australia, we typically have v = 6000 ms^{-1} and, for surface seismic, dominant frequency f = 50 Hz, creating a dominant wavelet or our measuring "stick" 120 m long. Hence, depending on the case, our resolving power is in the order 40-60 m for surface reflection data. If we place either source or receiver below the regolith we could double our resolving power as reported by Greenwood (2013). If both source and receiver are below the regolith the resolving power will be even better, potentially quadruple in comparison to the surface seismic as competent hard rocks have typically very high quality (Q) factor (Urosevic, 2018, personal communication). In fact, the dominant wavelength, λ, is likely to be even shorter due to the fact that borehole sources typically produce very high dominant frequency. For example, a sparker source produces seismic pulse from 1 KHz to several KHz at larger depths (refer to Appendix A).

Lateral seismic resolution is conventionally defined by the diameter of the first Fresnel zone, d_f, which is defined by Sheriff (1978) as:

$$d_f = \sqrt{\frac{2zv}{f}} \qquad \textbf{(Eq- 2.2)}$$

where z is the depth of burial of target and other symbols have same meaning as defined in equation (Eq-2.1). Once below the regolith, the effect of depth is negligible due to low attenuation (high Q) so the equation (Eq-2.2) may be approximated with $z = 1$. That would shorten the zone to couple of metres rather than 100 m plus. Perhaps the realistic value could be in 10's of metres. In any case the diameter of this zone is order of magnitude smaller compared to surface seismic. Notwithstanding the above analysis, some theoretical comparison is made later on with crosshole geometry and surface seismic in terms of vertical and lateral resolution using typical example from Salisbury et al. (1996).

Claerbout (1971;1985) defined the first Fresnel zone as the distance across the reflection hyperbola at the time when the first arrival has just changed polarity (Figure 2-2). This implies constructive response will come from a zone defined before 180^{o} phase reversal.

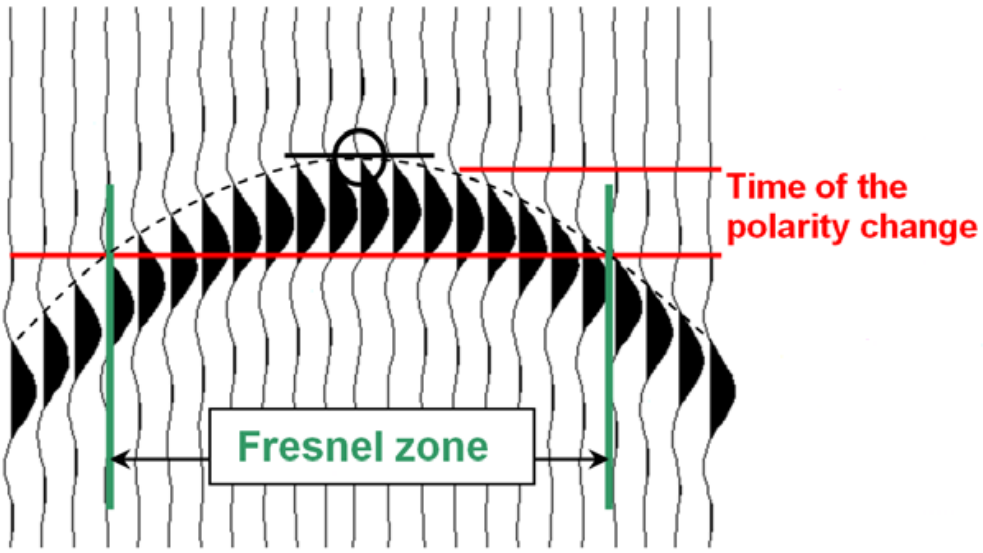

Figure 2-2: Claerbout's definition of the Fresnel zone (after Bancroft, 2007).

Equation (Eq-2.2) relates the Fresnel zone diameter as a direct proportion to the depth of the target (from the surface) and the velocity of the medium, and as indirect variation to the frequency of the source. The velocity of the medium cannot be controlled but the source frequency can be by the choice of the downhole energy

source. Crosshole geometry favours the use of high energy source that can lead to diminishing Fresnel zone.

Consider a typical example from Salisbury et al. (1996), for a surface seismic geometry, as compared with crosshole geometry. If a target depth is 1000 m and the formation velocity is 6000 ms^{-1}, then using a source with 100 Hz peak frequency for surface seismic geometry, theoretically, it is possible to image an ore-body of 15 m thickness or about 350 m lateral extent or both, from equations (Eq-2.1) and (Eq-2.2) for the respective parameter. Now by means of a crosshole geometry with the same formation velocity as above, using acquisition source peak frequency of 250 Hz, and assuming even for the same target depth, then theoretically, it is possible to image an ore-body of 6 m thickness or about 219 m lateral extent or both (from (Eq-2.1) and (Eq-2.2) for the respective values). Increasing the source peak frequency to say 500 Hz (see Appendix A for available downhole source peak frequency range), it is then possible to image an ore-body of 3 m thickness or about 155 m lateral extent or both.

What is more? The geometry has added advantage as the exploration boreholes are used to take seismic sources and receivers into the rock mass. The source and receiver points are thus literally brought closer to the target of interest and therefore reducing the target depth. With shorter target depth, the minimum resolvable thickness and diameter values obtained earlier with (Eq-2.1) and (Eq-2.2) in crosshole geometry will even be smaller. For example, let the target's average depth be 570 m. Then in the first case (with the 250 Hz), from equation (Eq-2.2), theoretically then, the Fresnel zone is diminished to 165 m, while in the second case (with the 500 Hz), it is diminished to 117 m, even-though from equation (Eq-2.1), the minimum resolvable thickness remains 6 m and 3 m respectively for the 250 Hz and 500 Hz peak frequency energy source application.

In all then, the higher the source dominant frequency or the shorter the target's depth or when both occur, as should be the case in the crosshole geometry, the smaller the Fresnel zone diameter needed and the higher the chance for lateral resolution. As Yilmaz (1987) puts it, a smaller Fresnel zone results in a higher spatial resolution.

The individual and combination of the above factors are favourable for CSR application for ore-body delineation. Thus, within favourable geological environment, the CSR method may be suitable to produce vertical and lateral high-resolution images even for small-volume, high density deposits at depth.

Generally, seismic is in fact very powerful in detecting rather than resolving lateral changes in reflectivity that may be related to structures, reflection terminations, small size reflectors ("point bars" or scatterers), etc. But the CSR geometry has the potential for improved resolution. This will be analyzed later in numerical studies.

2.2. Location of reflection points in CSR method

In surface seismic, the origin of a reflection point is established by Snell's law or more practically by using the virtual source image located as a mirror image across an interface: virtual rays are then drawn from the source image to the receivers. A reciprocal ray tracing is also valid (receiver image). This simple concept is valid for finding the point of reflection for VSP and crosshole seismic (Greenwood (2013). This simple concept is illustrated in Figure 2-3 to Figure 2-6. These are idealized simple illustrations for CSR geometries. In the simplest possible case of vertical boreholes and horizontal interface(s), such as in Figure 2-3, the distribution of reflection points is readily identified. For a (gently) dipping layer and a set of boreholes orthogonal to the layer, part of the space or the reflector surface area between the source and receiver boreholes cannot be illuminated by the rays emanating from the source due to the geometry (Figure 2-4). In the case of a dipping layer and non-orthogonal boreholes the illumination area is extended in up-dip direction away from the shallower borehole (Figure 2-5(a)). The total illuminated area is enlarged if the boreholes are spread further apart (Figure 2-5(b)). Finally adding the curvature to the borehole trajectories extends the up-dip illumination area (Figure 2-6). In borehole seismic, up-going reflected waves from targets can only be received and recorded by borehole receivers which are situated above the reflecting interface, at points where the waves intersect the receiver borehole path (Hardage, 1992; Mari and Coppens, 2003). Where part of the space between the source and receiver boreholes cannot be illuminated by the rays emanating from the source(s) it results in the creation of shadow zones, such as indicated in Figure 2-6. However, in

practice the complexity of reflection interfaces will be much higher causing seismic energy to travel along other paths that are much less predictable (Telford et al., 1990; Mussett and Aftab-Khan, 2009).

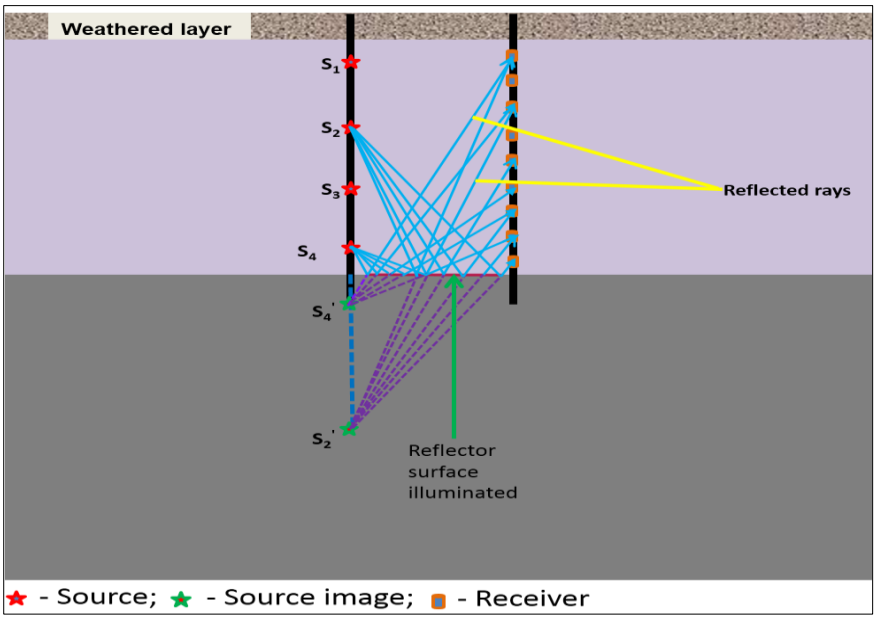

Figure 2-3: The origin of points of reflection (with ray-diagrams) for horizontal reflector and vertical boreholes with source image and reflection points shown for source points 2 (S_2) and 4 (S_4). The deep blue broken line is the normal to the surface. Distribution of reflection points is readily identified.

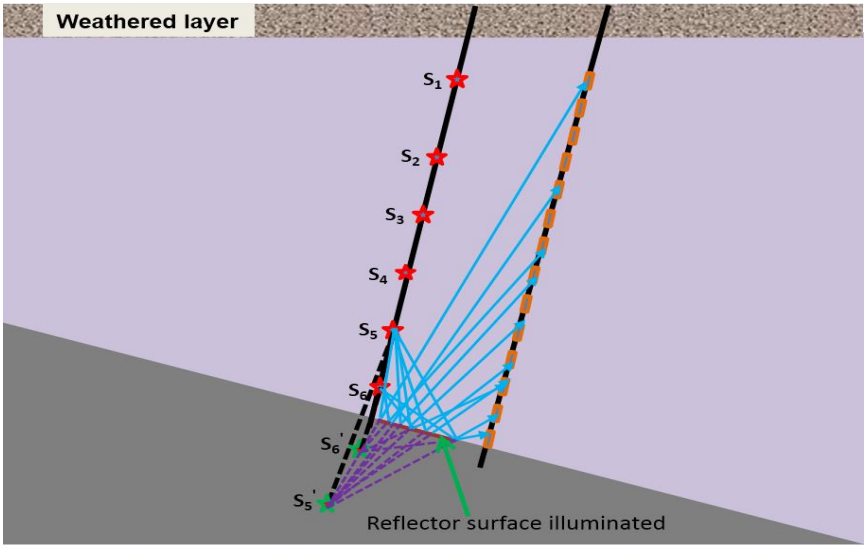

Figure 2-4: Origin of reflection points for slightly inclined reflector when the boreholes trajectory to the incline plane surface is near-orthogonal. The source image and reflection points are shown for source points S_5 and S_6. The black broken lines lie normal to the inclined plane.

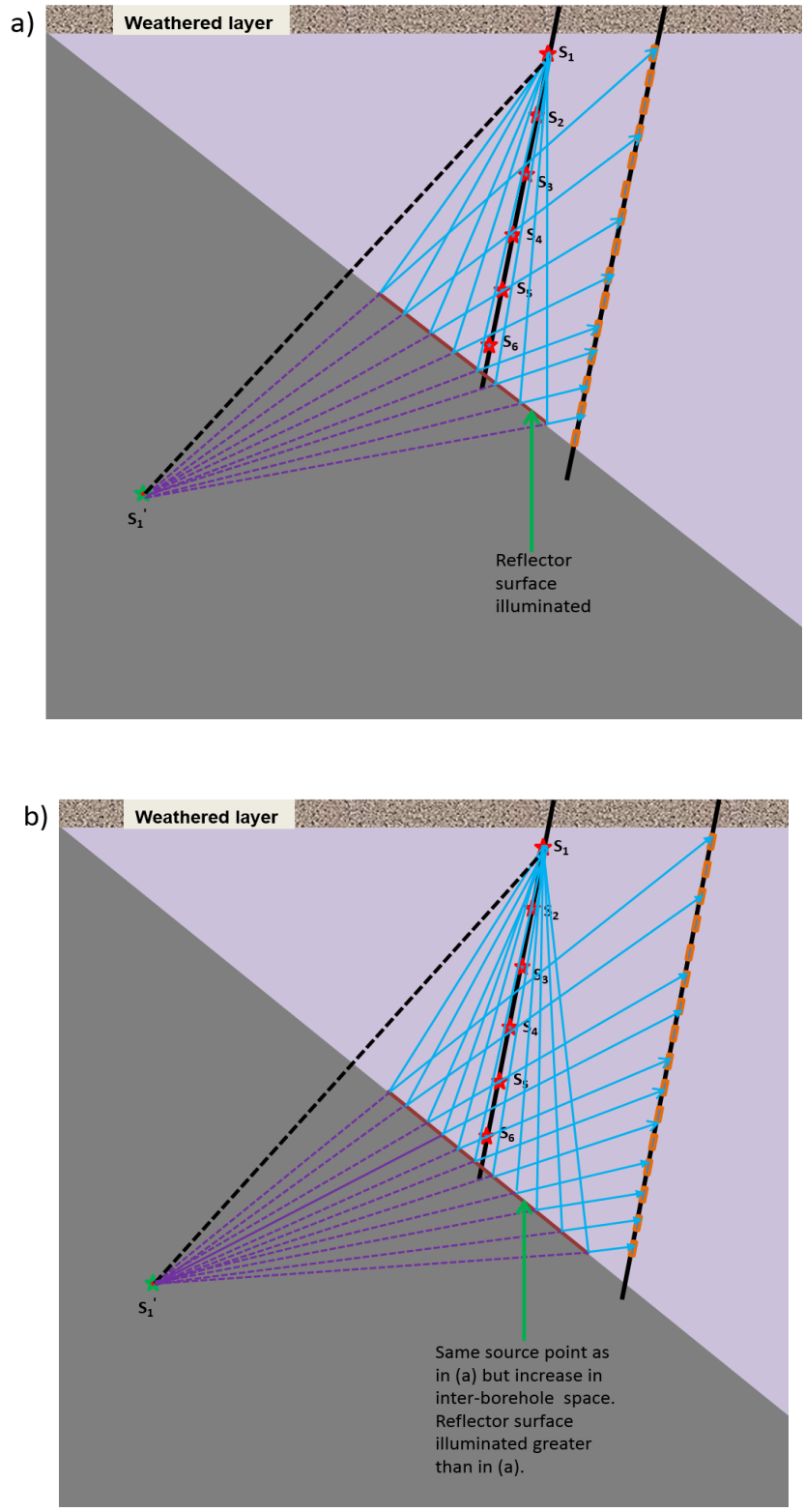

Figure 2-5: (a) Reflection points origin for about 45 degrees dipping reflector with non-orthogonal boreholes. Source image and reflection points are shown for source point S_1. (b) Same conditions as (a) but increase in inter-borehole spacing leading to a larger reflector surface area illumination.

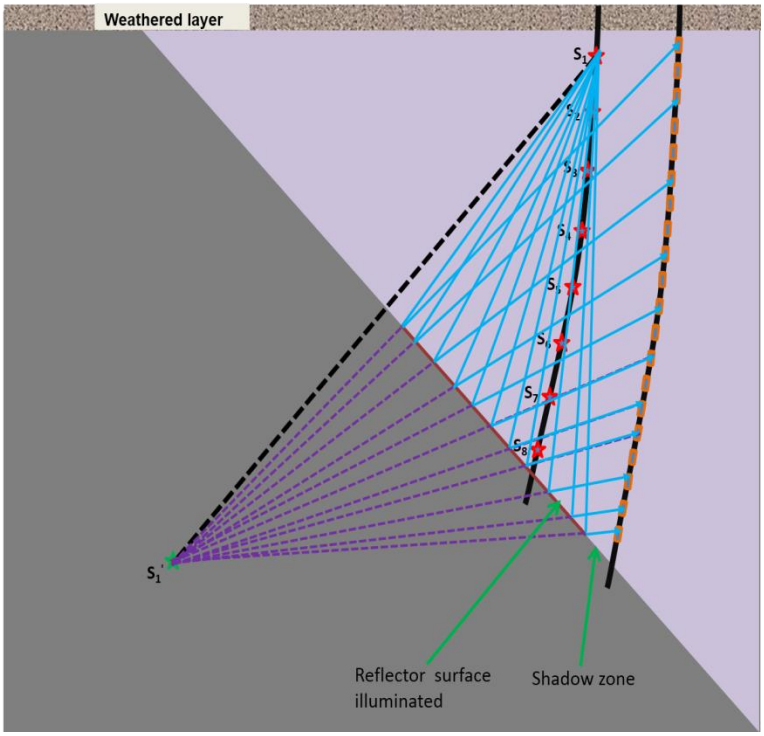

Figure 2-6: Reflection points origin for a steeply dipping reflector (> 45 degrees) and stronger angular boreholes. Source image and reflection points are shown for source point S_1. Indicated also are the reflector surface area illuminated and the shadow zone.

2.3. Introduction to the borehole reflection imaging

One of the main problems with borehole-based seismic imaging is that the illumination area changes significantly with small changes in target geometry. This leads to the presence of "blind" zones from which we do not get information back to the receivers. This is characteristic for 2D VSP illumination and imaging so that only a small area of the structure is illuminated compared with the surface seismic method (Hardage, 1992; Mari and Coppens, 2003). With this restricted illumination, there will be some uncertainty in structure estimation in VSP surveys (Wiggins et al., 1986). For a CSR method, target surface area illumination and consequent image recovery will depend on a number of factors. These include: angle at which boreholes intercept target of interest, inter-borehole spacing and location of borehole relative to the target, target geometry, and trajectory of boreholes. Furthermore, the amount of reflector surface area recovery depends on the source-receiver array length and array spacing (Rowbotham and Goulty, 1993), and migration aperture (Wiggins et al., 1986; Rowbotham and Goulty, 1993).

Considering that many geometrical variables enter into the CSR the expected seismic response from a given geological structure should be modelled to optimize survey acquisition parameters. In practice many additional factors will be equally important for conducting a successful CSR survey. Some are listed below:

- Borehole conditions: not entire length may be available due to instability or wedging (sharp changes in direction)
- Source type and signal strength (may require repetitive excitation to increase SNR through vertical stacking)
- Receiver type and separation (geophones, hydrophones, Distributed Acoustic Sensing (DAS), etc): some may be prone to variable coupling, patchy deployment due to pure borehole conditions, noise (tube waves) and nominal wide spacing causing signal aliasing
- Side sweeps: related to 3D nature of the geology and/or unfavourable borehole geometry

In this research I will concentrate on the effect of geometrical factors onto image quality rather than field component of CSR and in situ implementation.

2.4. Generation of seismic image in CSR

Mineralized zones are often related to structures (faults and shears) that are often sub-vertical. As illustrated in Figures 2-4 to 2-6, such dipping structures cause reflected seismic events to be laterally and vertically displaced with respect to their true subsurface locations. Lateral velocity variations would further amplify dispersion of reflection points (Yilmaz, 1987; 2001; Bancroft, 2007; Robein, 2010). Thus, the CSR survey geometry must be optimized to obtain true images of the dipping reflectors for which very high precision is required. That can only be achieved by the application of Kirchhoff pre-stack depth migration (PSDM) which is the most common method of pre-stack depth imaging in reflection seismics. This is discussed later in the thesis.

2.4.1. VSP and CSR mapping

Crosshole imaging can be considered as a multi-offset VSP data problem where source is placed not just at one position but at many different positions down the

borehole. Hence it is of interest to consider the reflection point distribution for an offset VSP survey that allows us to create a CDP-equivalent surface gather by mapping VSP-reflection point into it. The mapping of the acquired VSP data from the time-depth domain to offset-depth domain can be performed by so called vertical seismic profiling to common depth point (VSP-CDP) transformation or pre-stack migration (Wiggins et al., 1986). The VSP-CDP transformation is widely accepted because it is an initial, simplistic step in image creation. Strictly speaking, it is exact only for a single horizontal interface. The transformation, however, cannot map reflections from more than one point arriving at a given time on a given trace to their correct locations. This is a big setback to the approach (Wiggins et al., 1986).

Wyatt and Wyatt (1981) described a "VSP-CDP stack" procedure to convert time-depth offset VSP data to an offset-depth image similar to depth migrated surface seismic sections. Their procedure tried to correct for the shortfall in the VSP-CDP transformation. A comprehensive study was published by Dillon and Thomson (1984) on how multiple VSP acquisition geometries such as offset, walk-away and deviated well could be employed to illuminate the subsurface structure using the VSP-CDP stack approach. Dillon and Thomson (1984) VSP-CDP stack transform can be described as a mapping technique which calculates velocity from VSP direct arrivals and then determines the origin (in terms of depth and offset) of reflected and scattered wavefields and other late arrival events from the velocity and geometry of the source and receiver. The principle of the transformation technique for a constant velocity is outlined in Figure 2-7. This simple mapping technique is for that of a single-channel process and thus not depend on the structure of the data. Despite this short coming, the VSP-CDP mapping is considered a very useful tool in VSP image processing because of the previously mentioned advantageous points. In addition, the mapping technique is robust in the presence of noise. The popularity of the method has one time been extended to the imaging of crosswell reflection data for hydrocarbon search (Van Schaack and Costa, 1996).

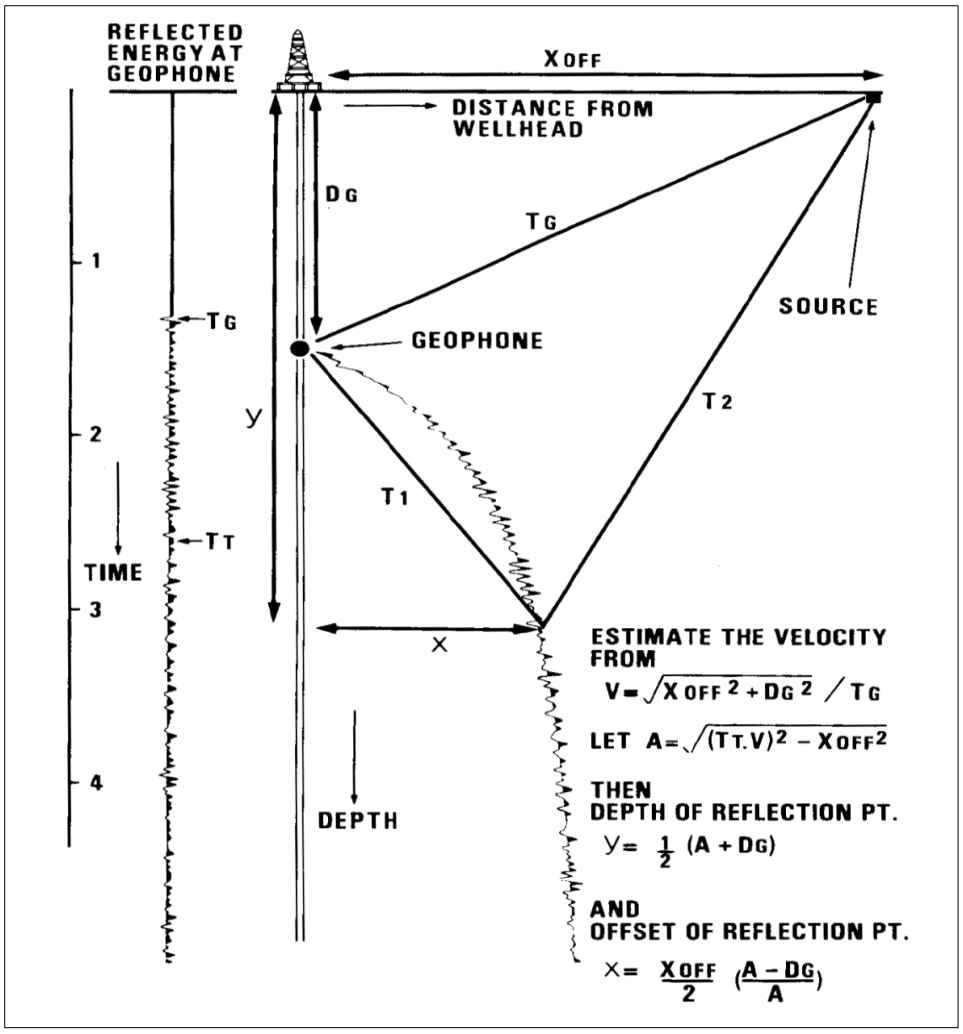

Figure 2-7: Graphical illustration and mapping formulae of VSP-CDP transform for constant velocity model and application to a single offset-VSP trace (Dillon and Thomson, 1984).

2.4.2. VSP and CSR imaging

A number of VSP imaging algorithms exist presently but the most commonly used is based on Kirchhoff integral (Kirchhoff diffraction formula) that was utilized for seismic waves by French (1975) and Schneider (1978) and presented by Dillon (1988) as:

$$U(\boldsymbol{r},t) = \frac{-1}{2\pi}\int dS_o \frac{\partial}{\partial n}\left[\frac{U(\boldsymbol{r_o}, t + {}^{R}/_{C})}{R}\right] \qquad \textbf{(Eq- 2.3)}$$

where $R = |\boldsymbol{r} - \boldsymbol{r_o}|$, $U(\boldsymbol{r},t)$ is the wavefield to be calculated at some point $\boldsymbol{r}$, $U(\boldsymbol{r_o},t)$ is the wavefield measured over the surface S_o, and $\boldsymbol{n}$ is the normal to the elemental surface area dS_o at $\boldsymbol{r_o}$. C is the speed of sound in the wave medium and,

hence, R/C is the propagation time from **r** to $\mathbf{r_o}$. Equation (Eq-2.3) is a form of the Kirchhoff integral and allows one to see the effect of the non-planar observation geometry clearly (Wiggins, 1984). The above integral expresses Schneider's equation (4) in Schneider (1978) as a reverse-time extrapolation, with the directional derivative obtained for specific geometries – for a near-planar vertical surface and for a vertical well – as shown in Figure 2-8 by Dillon (1988). This generalized equation can be expressed explicitly in terms of sources and receivers (Dillon and Thomson, 1984).

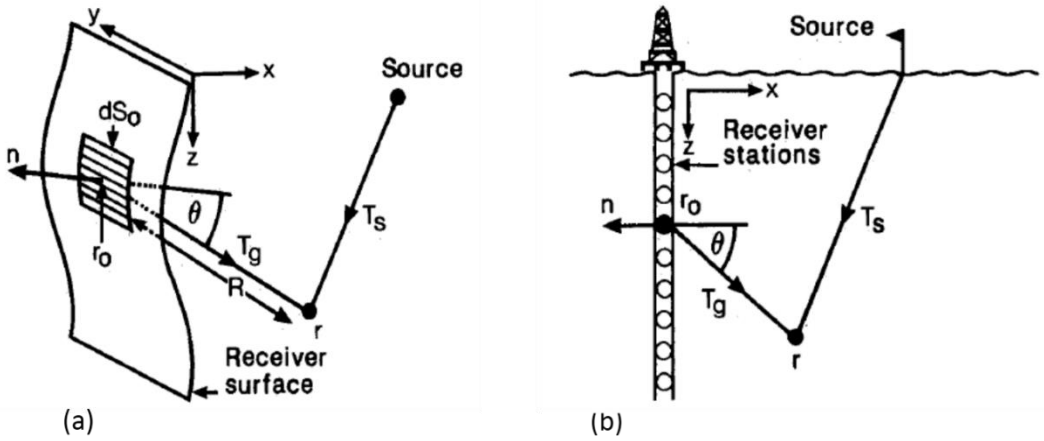

Figure 2-8: Wavefield extrapolation and imaging. (a) Geometry for wavefield measured on a near-planar vertical surface. (b) Geometry for wavefield measured at a vertical well (after Dillon, 1988).

Kirchhoff migration is usually expressed by evaluating the receiver extrapolation integral at the time when the source pulse reaches the reflector (Schneider, 1978). The result of the integral for each source is then summed to yield the migrated image. By not performing the Kirchhoff integral over sources, one does not achieve the reciprocal symmetry between sources and receivers and, more importantly in practice, does not include the geometrical weighting factors related to the source geometry (Wiggins, 1984; Dillon, 1988).

Equation (Eq-2.3) gives the wavefield at point r for all time. For the purpose of forming an image of the subsurface, Dillon (1988) restricted the interest in this wavefield to the time at which the source energy excites the diffractor at r according to Claerbout's (1971) imaging principle. The details on this are given by Wiggins (1984) and Dillon (1988). Greenwood (2013) summarized it in a more simple form

as follows: “Migration by Kirchhoff integration for a chosen scatterer or depth sample (image space or geology) involves (1) computing the travel-time for each source-receiver pair using a given velocity model; (2) extracting the sample value (amplitude) for a given time from the time section (seismic traces); (3) applying obliquity and spherical divergence for amplitude correction; and then (4) collecting the results in the image space for a chosen depth (for image gather).” In the integration, the weights are chosen according to the incidence angle. The summation process is restricted by the aperture angle which, itself, is determined by the maximum dip angle expected of the subsurface geology in the area.

The remarkable thing about the Kirchhoff integral is its generality: it can be used to handle cases where the velocity changes (whether vertically or laterally depending on time or depth migration application) by introducing a procedure of root-mean-square (rms) velocity scaling to correct for propagation anisotropy; it is capable to handle almost any source-receiver geometry configuration, irregular spacing of receivers, and dip up to 90º. More so, the Kirchhoff migration readily opens itself to external control. This control proves to be a significant advantage when migrating borehole seismic data (Dillon, 1988) as it creates room for optimizing the migration by controlling the aperture of migration.

2.5. Forward modelling and synthetic data generation

Seismic forward modelling involves simulating elastic wave propagation through a specified subsurface model. In its simplest form, it involves only acoustic case where model parametrisation requires only P-wave velocity and density.

The importance of synthetics cannot be over-estimated. Anderson and Cardimona (2002) stated the usefulness of synthetic seismic records in a succinct way as follows: “To determine if an intended or expected geologic target will generate an interpretable signature on output processed reflection seismic data, synthetic seismic records are generated before field acquisition. Synthetic records generated after acquisition and processing of seismic field data facilitate the interpretation of the processed field data, particularly if the corresponding geologic models were proximal borehole sonic and density logs.” Synthetics can also be a valuable tool

with respect to the design of an acquisition programme – field acquisition parameters, sources, receivers, fold, and so on.

Three important categories for seismic forward modelling are: integral equation approach (based on Huygens' Principle), ray-tracing method (based on Snell's Law for ray parameter calculation), and direct methods (based on time and space derivatives) (Carcione et al., 2002). I employed the direct methods for this study. In direct methods, the time and space derivatives of the wave equation, expressed in a continuous function, are discretised to a discrete function (Bording and Lines, 1997) which is suitable for numerical evaluation and implementation. Direct method codes use finite difference (FD) or finite element (FE) algorithms to solve the wave equation. Direct methods are often termed full waveform modelling techniques for the obvious reason that the solution implicitly gives the full wavefield (Bording and Lines, 1997; Carcione et al., 2002). Modelling with direct methods is the closest, among the categories, to the wave propagation process, which can be easily visualized as an animated series of snapshots (Carcione et al., 2002).

With the above in mind, the main purpose of this research is to test the viability of CSR imaging with exploration borehole geometries typical of mineral exploration. For that purpose, a number of modelling experiments over realistic geological models were conducted. Full waveform modelling is performed using Tesseral-2D modelling package. Within Tesseral-2D software package, the seismic source can be set as either a directional (horizontal or vertical) monopole or dipole, or as an omni-directional source. The source wavelet frequency can be determined by the user and the type of wavelet can be either chosen from a list of pre-set wavelets (example; Ricker, Single, Double) or user defined. The observation time-series assumes particle displacement amplitudes similar to that recorded by a geophone.

For seismic ray tracing, a 3D ray tracing method should be used to generate more realistic results although dealing with a 3D geology, for a proof of concept, I used a 2D ray tracing method. Using a 2D ray tracing method in modelling for this purpose is more convenient as we can readily visualise, easily comprehend and evaluate the outcome of the modelling. In reality the seismogram recorded is likely to be more complicated and contain off plane events. The target reflection will be present and

also favoured by the crosshole geometry since in brown fields most of the boreholes are oriented orthogonal to the dip direction. It is the matter of data analysis how to verify primaries and/or attenuate side events. Thus to stay focussed on this methodology I deployed 2D modelling which avoided the risk of spreading this research over very wide territory.

2.6. CSR data processing

The purpose of seismic data processing is to generate an accurate image of the subsurface geology (Dragoset, 2005). The ideal input to the migration programme should be the acoustic reflection response of the subsurface devoid of all multiples and transmission effects. Since data acquired is far from the ideal, it must be processed to mitigate these effects. Crosshole geometry is similar to offset VSP geometry (Hardage, 1992; Mari and Coppens, 2003) and borehole-to-borehole seismic reflection data set is processed in essentially the same way that offset VSP data are commonly processed (Hardage, 1992; Mari and Coppens, 2003). For this reason, synthetic CSR data processing sequences employed in this work are generally analogous to those applied in VSP wavefield separation and seismic imaging. In all the cases considered in this thesis acoustic modelling was used, so S-wave energy and converted waves were not present. Also, noise was not added to the data. As such, wavefield separation was relatively straight forward. In general, the data processing and wavefield separation involved the following steps:

- Assigning geometry to the data
- Spherical Divergence Correction
- First break picking
- Removal of direct wave – by muting or by frequency-wavenumber (F-K) filtering or by 2D-trace median filtering
- F-K filter of (all) down-going wavefields (with quadrant block unless otherwise stated)
- F-K or 2D median filtering of coherent linear wavefields
- Band pass filter Ormsby band-pass (cut-off points vary from data to data)
- Trace killing of channels below the borehole-interface intersection
- Top muting above the first arrivals to remove filter artefacts
- Imaging (typically Kirchhoff depth migration)

It has been said earlier in Chapter 1 that the choice for boreholes separation should be informed by the purpose of the survey and, whenever possible, they should be separated enough to enable separation of wavefields. It is important to add that in CSR real data processing, great attention must be paid to the wavefield separation when the spacing between the two boreholes is short as difference between the direct and reflected waves may be small particularly for low frequency waveforms.

2.7. Summary

The adoption of seismic methods and techniques for mineral exploration has been slow because of the geological complexity associated with hard rock environments. High acoustic impedance contrasts and high signal-to-noise ratios (SNRs) are generally lacking in hard rock environments. However massive ore may have a distinct seismic signature (Milkereit et al., 1996; Salisbury et al., 2000; Urosevic et al., 2012). A strong seismic signature in crosshole environments is however likely to be less critical than for surface seismic as the ambient noise is very low and signal clarity and transmission properties very good.

Predicting the illumination patterns of borehole imaging in complex geology is not trivial. For that reason, I utilized simple ray-diagram illustrations of CSR geometries to analyse illuminated regions for different borehole geometries and different geological models. From the modelling results it became apparent that it is possible to produce high-resolution images of a dipping reflector up-dip of and away from exploration holes. The higher the source point location is in the borehole, the greater the up-dip illumination of the target. In general, the size of the illuminated area depends largely on the source aperture and receiver array length. This is important to remember as CSR geometry has generally a shorter lateral source aperture than the counterpart multi-offset VSP geometry.

Migration of CSR data does not require a new migration algorithm. A standard VSP Kirchhoff migration can be used. Care, however, must be taken to extend the velocity field to accommodate imaging away from the boreholes as the initial geological model may not be a priori known or correctly assumed.

3. Where to consider the use of the crosshole seismic reflection method

3.1. Introduction

Generally, the subsurface image recovery provided by CSR is over (relatively) a small area and very near the boreholes whereas 3D VSP or 3D surface seismic can provide an image of the subsurface structure over a much larger area. Also, the application of the CSR to provide high-resolution images of dipping structures has not been unconditionally proven. We could consider CSR as a method that can be used as complementary to potential field methods, 3D surface seismic and/or 2D/3D vertical seismic profiling (VSP) methods. The CSR method could be, in some geological settings, used as alternative exploration method where electrical and electromagnetic (EM) methods have limited resolving ability as typical of deeper targets. An untested combination may include integration of downhole EM and CSR that could be of interest for detection and delineation of VMS deposits. To determine the feasibility of the CSR method, some critical questions need to be considered:

1. Is it suitable for the geological setting under investigation? One of the favourable situations would include massive (high-grade), deep seated ore-bodies that may not be detectable by any surface method.
2. Is very high resolution that CSR provides required for the objective of the study? For example, the case of small but rich ore-bodies containing high ore concentration, as is often the case with nickel pods in Kambalda region, WA.
3. Does it financially make sense to perform CSR to obtain extra information? For example, high definition of a limited area required for shaft planning would be helpful in de-risking potentially hundreds of millions of failed investments.

3.2. Typical suitable hard rock environment for CSR survey

The “best case” for application of CSR has not been evaluated either in the modelling study or through case studies as there is only a few of those reported in the literature. Perhaps the CSR method could be considered for delineating

geologically complex and physically difficult located ore-bodies that are problematic to delineate with surface seismic or VSP methods. The CSR method is relatively expensive and is likely to be used for high economic value targets as add on value. Like any seismic reflection method, the CSR method detects elastic impedance contrasts between rock units. Hence it is to expect that the method is more effective for the case where strong contrast in elastic properties exists. However, we could consider exactly opposite case where the ore-body is practically transparent to the surface seismic method due to very low reflectivity. Would this pose a problem for the application of CSR method? This is not clear yet and will be found out with time where below the regolith the sensitivity of seismic measurements will greatly improve the data generated as well as the resolution. Similarly, a highly irregular shaped ore-body may result in excessive energy scattering. The CSR geometry may be favourable for data recording of such ore-body, but other conventional seismic recording geometries may not be found suitable.

The actual potential of CSR technique has not been established until now neither in recent exploration history nor in general methodical considerations. But the method could be useful and a valuable technique for hard rock exploration where any of the following geological or physical factors or a combination of them exists: (i) thick heterogeneous overburden cover - regolith attenuating high frequencies and causing significant time delays that could seriously degrade seismic images (ii) deposits under a thick conductive zone; (iii) buried, low-volume but high density deposits located within small or localized area; (v) buried, steeply dipping ore-bearing structures; (vi) deposits located in areas with severe topographical issues or thick vegetation cover or both, (vii) active mine sites with no access to surface receivers and shots.

3.3. Selected ore deposits for CSR feasibility study

In this study, I have identified several deposits that may be difficult to delineate by surface geophysics and modelling of CSR imaging performed on a number of them. The modelling was performed to investigate:

1. The potential of the CSR method to produce high-resolution seismic images with angled boreholes in complex hard rock environments.

2. How ore-body image recovery is affected by the factors such as: structural dip, angle at which boreholes intercept target of interest, inter-borehole spacing, location of borehole relative to the target, and trajectory of boreholes.

The principal geological settings in this study are of Australian hard rock environments prospective for base metals. Two broad based types of mineralization – the komatiite-hosted nickel sulphide deposits of Yilgarn Craton, Western Australia, and the volcanogenic (or volcanic-hosted) massive sulphide deposits of Rosebery, Tasmania – are considered. Specific depositional styles are considered for these broad-based types of mineralization. What they all have in common is their small size, complexity, and inability to be characterized properly from the surface due to low resolution. Their 3D shape may best require either both 3D surface seismic plus CSR or even 3D surface seismic plus CSR and 3D VSP combinations.

A. Komatiite-hosted nickel sulphide deposits with typical depositional styles considered include:

(a) McLeay nickel sulphide ore deposit at Kambalda, Western Australia.

Ore deposits of this kind are magmatic massive nickel sulphide mineralization. They are narrow, steeply dipping, ribbon-like accumulations of deposit with varying thickness regolith that prevents high frequency information from being recovered. However, high elastic impedance difference exists between such mineralized zones and their host rock in the region (Urosevic et al., 2012).

(b) Maggie Hays nickel sulphide deposit style. This includes Maggie Hays North and Maggie Hays Main nickel sulphide deposit styles.

(i) The Maggie Hays North nickel sulphide deposit style is steeply dipping, elongated deposit overlain by a highly conductive banded iron formation hosted barren sulphide (Peters and Buck, 2000; Williams et al., 2012).

(ii) The Maggie Hays Main nickel sulphide deposit style is vertical in geometry, blind to the surface seismic with the top of the main disseminated sulphide zone beginning at a depth of about 200 m beneath the surface and the main massive sulphide zone at a depth of about 350 m beneath the surface (Peters and Buck, 2000). The disseminated nickel sulphide zone is in contact with the massive nickel sulphide zone and

both jointly formed vertically oriented nickel sulphide mineralized zone. The thick cover layer of the nickel ore deposit has varying degree of conductivity. Also, close to the ore deposit lays a highly conductive banded iron formation hosted barren sulphide zone.

(c) Small size but dense (clustered) nickel sulphide deposits of Yilgarn Craton:

The small-volume nickel sulphide ore deposits associated with komatiitic rocks in the Archaean Greenstone belt of the Yilgarn Craton of Western Australia are mostly remobilised, high-grade deposits. Most of these deposits are located at depth, hidden by deep, heterogeneous and often-conductive regolith sequence, and hosted in steeply dipping structures (Urosevic et al., 2012). They are extremely challenging exploration targets.

B. Volcanic-hosted massive sulphide deposits, Rosebery complex ore lenses, Tasmania, Australia:

These are strata-bound individual and clustered polymetallic ore lenses. The deposits are buried at depth and hosted by dipping structures. The ore lenses are mostly elongated in shape with most having down dip extensions of tens to hundreds of metres but nearby to the host rock, and stretching as the host rock, is a conductive horizon (Solomon et al., 2004). In addition, there is severe topographical issues coupled with thick vegetation cover that restrict surface geophysical exploration methods.

Thus my study will model crosshole seismic response over the selected deposits all of which are challenging for exploration by surface geophysical methods. These complex numerical geological models will be probed by a variety of recording geometries to investigate the imaging potential of crosshole method.

The first case study is presented in Chapter 4 and draws comparison between the new CSR method with a more conventional multi-offset VSP. The underlying model represents the McLeay nickel sulphide deposit from Western Australia. For the purpose of comparison, the chapter presents synthetic datasets for each of the examined methods. Attempts are made to analyze the results in a detailed and comprehensive manner. In addition, a comparison of the synthetic results to a real

VSP field data is drawn to confirm the synthetic studies and, therefore, to authenticate the CSR method.

Having established the CSR method in the previous chapter, Chapter 5 continues the series of synthetic case studies with an analysis of CSR capability to image and delineate Maggie Hays nickel sulphide ore zones buried at depth within Yilgarn Craton of Western Australia. The chapter investigates the two different deposition styles – Maggie Hays Main and Maggie Hays North nickel sulphide deposit styles – which are modelled and analyzed separately.

The third and final case study being Tasmania Rosebery-type VMS complex ore lenses is presented in the sixth chapter. The capability of the CSR method to delineate some very complex geological structures under cover is demonstrated with CSR synthetics. In addition, a comparison between the synthetic results and a 3D acquired field data is drawn.

Velocity information for model construction is provided in various ways: logs, core tests, borehole information and mapping. Synthetic CSR imaging in this study utilizes constant velocity of the ore hosted rock layer. In reality, to perform CSR imaging requires a depth-variable velocity function derived from the layers of the earth. The velocity-field can be obtained in different ways. Using the available borehole(s) the velocity model can be derived from ZVSP first break pick (FBP) and then, in turn, used in the migration process. Alternatively, optimal velocity field is required. An initial intra-borehole velocity field is provided by the tomographic reconstruction of the velocity. This field is used for the first run of pre-stack depth imaging (Kirchhoff integral solution). Initial image may need to be followed by several iterations involving subtle modification of the velocity field. An optimum image will be then estimated based on the image coherency, resolution, continuity, and amplitude intensity. The velocity field for this optimum image becomes the optimal velocity field and then be used for the CSR imaging. A more sophisticated procedure would involve Full Wave Inversion (FWI).

3.4. Summary

From available literature, the actual potential of CSR technique to provide high-resolution images of dipping structures outside the exploration hole has not yet been established until now neither in recent exploration history nor in general methodical considerations. But the technique could be useful and valuable for hard rock exploration either as alternative or, in some geological settings, as complementary to potential field methods, conventional surface seismic and/or 3D surface seismic and/or 2D/3D VSP methods.

Undoubtedly, the subsurface image CSR can provide is over relatively a small area and near the borehole compares with the size of image area a 3D VSP or 3D surface seismic can provide. Nonetheless, the CSR method could be considered for delineating very rich mineral deposits located in geologically complex and physically difficult areas that are problematic to delineate with surface seismic or VSP or both and other conventional potential field methods. I have presented two (2) broad based types of mineralization – namely the magmatic massive nickel sulphide mineralization and the volcanogenic massive sulphide mineralization – with different depositional styles where the CSR method is envisaged to be very useful and valuable in gathering (useful) information than surface seismic, VSP, and other surface potential field methods. These deposits are utilized in the subsequent chapters to test the feasibility of the CSR method.

4. Feasibility of crosshole seismic reflection for imaging Kambalda style deposit: McLeay nickel sulphide deposit

4.1. Introduction

The plausibility of the CSR method has been briefly analyzed in Chapter 2 by comparing its imaging capability with that of the VSP method. The two have different geometries suggesting both could be used in the imaging process to complement each other. More thorough analysis is presented here using a well-known geological model of the McLeay magmatic massive nickel sulphide ore deposit at Kambalda, Western Australia. Numerical simulation of multi-offset VSP (MVSP) data has been compared to the field results. Subsequently CSR study was conducted. CSR image was compared to MVSP synthetic and field data results to validate the CSR method.

4.2. Geology of the McLeay ore deposit

The McLeay ore-body is owned by Lightning Nickel Pty Ltd which is itself, a fully owned subsidiary of Independent Group NL, IGO. IGO acquired the Long Operation mine in Kambalda, Western Australia, from BHP Billiton Nickel West Pty Ltd (BHPB) (formerly called WMC Resources Ltd) in September 2002. The mine was re-commissioned in October 2002 and has been in operation successfully and safely ever since (Independent Group NL, 2014). The McLeay ore-body forms part of the Long Operation ore-bodies (Long, Moran and Victor South ore deposits) near the Kambalda Dome that are commonly referred to as the Lightning Nickel Long Victor Complex. The general geology of the Kambalda dome is shown in Figure 4-1. The Long, Moran, Victor South, and McLeay deposits are typical Kambalda-style nickel deposits. They consist of narrow, steeply dipping, shallowly south-plunging, ribbon-like accumulations of massive and semi-massive (matrix) with minor disseminated sulphides. The mineralization is located at the base of Archaean komatiitic ultramafic flows at the contact with an underlying tholeiitic basalt unit. The massive sulphide is overlain by matrix then disseminated mineralization, with the bulk of the

nickel mineralization being massive and matrix in nature. The host rocks and associated contacts have been subjected to lower amphibolite facies metamorphism, structural modification, and intrusion by multiple felsic to intermediate igneous dykes and sills (Independent Group NL, 2013; 2014). It is reported that the McLeay ore-body remains open to the south. However, a swarm of porphyry dykes stopes out mineralization at the southern limit of the existing resource and creates difficult drilling conditions that have thus far prevented effective testing of the prospective contact further to the south. Mine development has now reached the current southern end of the McLeay ore-body and this development will be used to test for the continuation of the McLeay ore system (Independent Group NL, 2013).

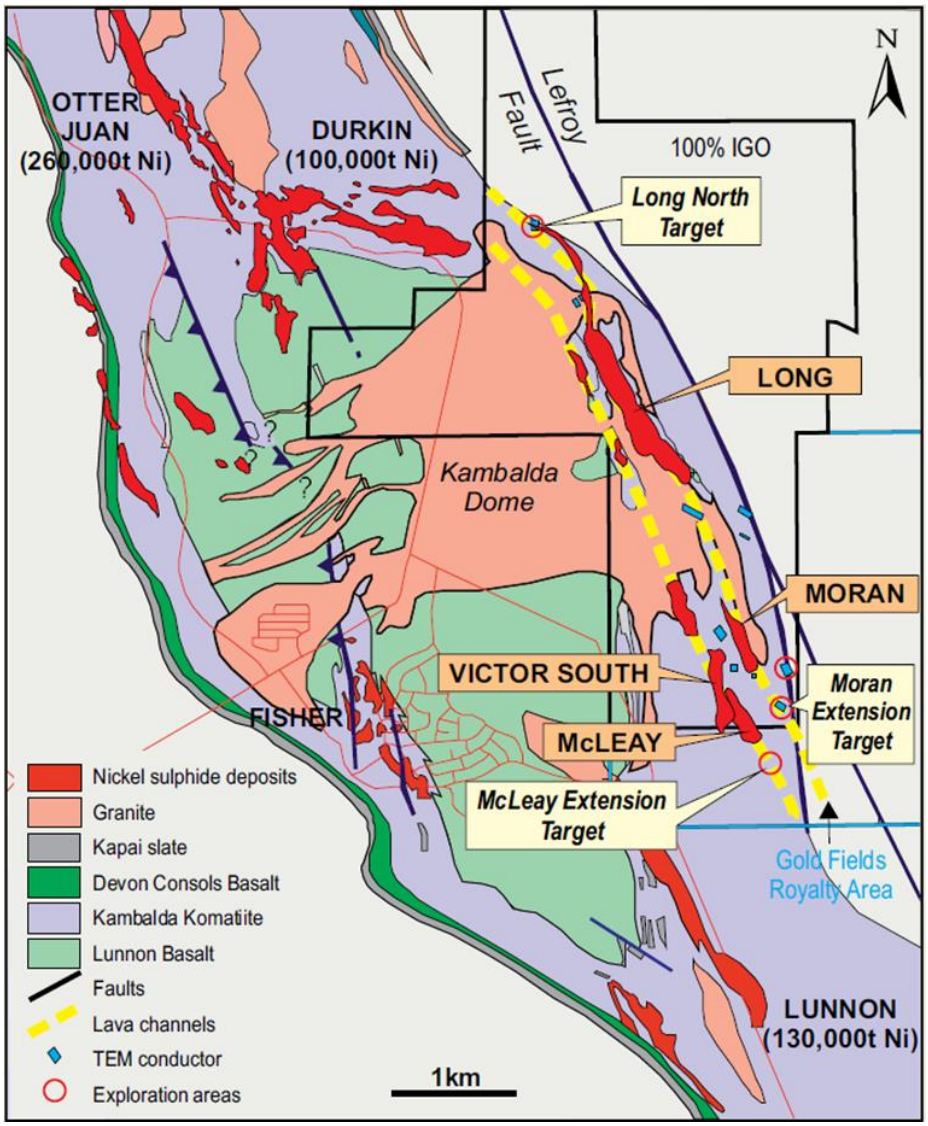

Figure 4-1: Regional geology, tenure, nickel shoots and targets shown on part of the Kambalda Dome. (Courtesy: IGO Annual Report 2013). The ore shoots shown are in plan projection.

4.3. Geologic model for VSP and CSR data generation

Figure 4-2 depicts a 2-D geological model of McLeay. The drill-hole LNSD-063 is used as the receiver borehole in the VSP experiment. Shown also are the drill-hole LNSD-062 and the surface shot point locations indicated by triangles. Boreholes are angled to intersect the dipping lithology as close to near normal incidence as practicable (Greenwood, 2013). The drilling of LNSD-063 however was restricted by surface access on Lake Lefroy constraining the collar location to the same drill pad LNSD-062. LNSD-063 was drilled to test deeper mineralization, as such it is opposed in direction to that of LNSD-062 (Figure 4-2). LNSD-063 intersected nickel sulphide mineralization at 5.4% Ni at a depth of 997.5 m with a true width of 4.4 m (IGO 2014 Annual Report). The zone of nickel mineralization has not been incorporated into the model.

The petro-physical values assigned to the various rock units are presented in Table 4-1. These values, apart from those assigned to the faults, are average values obtained from LNSD-063, LNSD-062, and from values obtained from ultra-sonic pulse-transmission testing of rocks units in the vicinity. The velocity and density values assigned to fault-1 and the Kambalda fault have been estimated. The velocity and density values of fault-1 were chosen such that a significant acoustic impedance contrast (of reflection coefficient > 6%) exists between it and the host rocks.

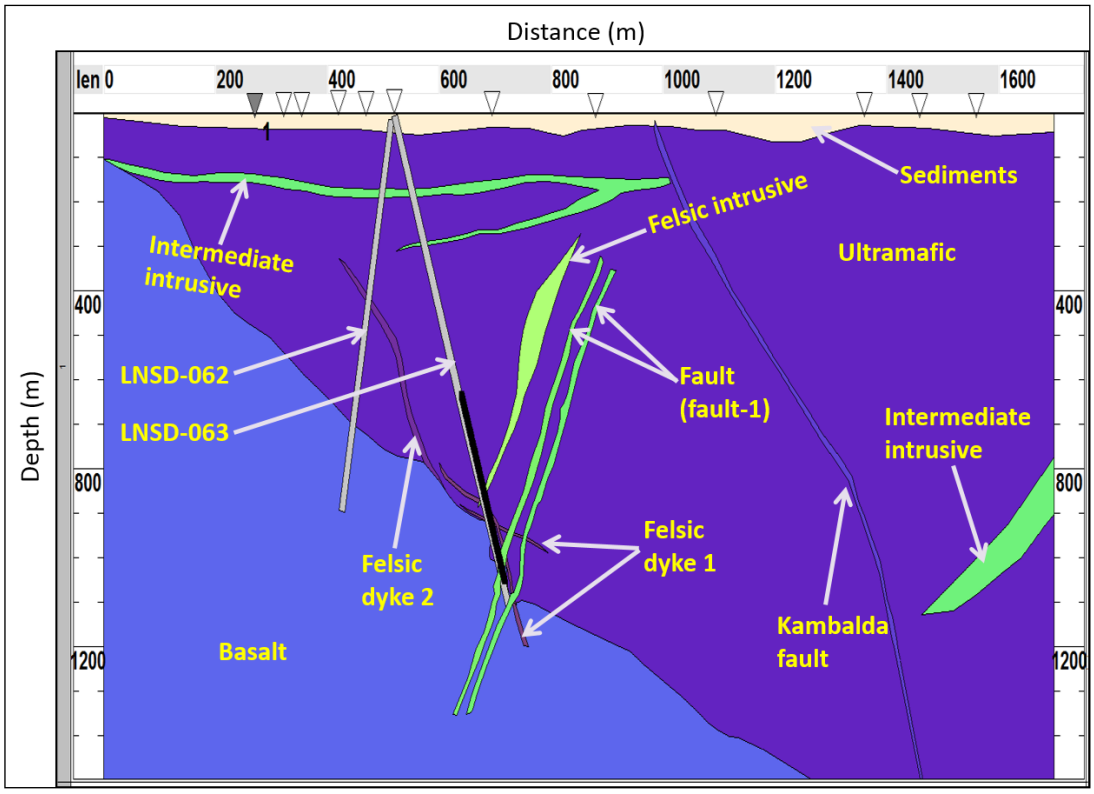

Figure 4-2: The McLeay geological model with drill-holes LNSD-062 and LNSD-063. Shown also are receivers original array (in black) and the multiple-offset vertical seismic profile (MVSP) shot points (shown by triangles).

Table 4-1: Velocity-density table for McLeay geological model with reference to: (Stolz et al., 2004; Turner et al., 2007; Urosevic et al., 2012; Williams et al., 2012; Greenwood et al., 2014).

Rock layer	Vp (ms^{-1})	Vs (ms^{-1})	ρ (kgm^{-3})	Acoustic impedance, ρ * Vp x 10^6, ($kgm^{-2}s^{-1}$)
Sediments	4030	2298	3142	12.7
Ultramafic (UM)	5460	3150	2810	15.3
Basalt	5700	3470	2958	16.9
Fault-1	4880	2529	3980	19.4
Felsic intrusive	5740	3445	2763	15.9
Felsic dyke 1	6015	3660	3025	18.2
Felsic dyke 2	5980	3526	3005	18.0
Kambalda fault	5900	3449	2735	16.1
Intermediate intrusive	5650	3600	2900	16.4

4.4. Ultramafic-basalt interface imaging with real and synthetic VSP

The reflector of most interest is the interface between the Archaean komatiitic ultramafic and the underlying tholeiitic basalt unit. The contact nickel mineralization zone lies at this interface. As a part of the objectives captured in Section 4.1, the real data VSP image of this interface will be compared with the pre-stack depth migration (PSDM) image obtained for the same interface using synthetic VSP.

4.4.1. Multiple-offset VSP (MVSP) survey

In June 2014, Curtin University acquired an experimental zero-offset VSP (ZVSP) and multiple-offset VSP (MVSP) using borehole LNSD-063. A 24-channel hydrophone string with a 2-m channel interval was deployed between 1060 to 634 m depth. Small 150 gm explosives were used as the seismic source. The explosives were placed into shot holes drilled to 1.3 m depth and stemmed with water. PVC lining was used to ensure the shot holes remained open. Before firing, a blasting mat was placed over the shot hole to restrict the water column ejecting into the air. This helps to force the seismic energy into the ground.

The velocity model derived from ZVSP first break pick (FBP) was used in the migration process of the MVSP data. Also, acquired in LNSD-063 were Full Waveform Sonic (FWS) data. FWS logs provide direct in-situ measurements of the acoustic P-wave (compressional) and S-wave (shear) rock velocities (Greenwood et al., 2014). These physical measurements were used for rock characterization, seismic volume depth correction and seismic reflection analysis to depth correct a large 3D seismic data collected in 2008 (Urosevic et al., 2008; Greenwood et al., 2014).

Prior to the MVSP survey, seismic ray tracing was conducted utilizing the known, yet simplified geological model and drill-hole LNSD-063. The ray tracing indicated that seismic shot points needed to be both geologically up-dip and down-dip of the borehole (collar) position. The actual shot point locations used, and the ray tracing diagram are shown in Figure 4-3.

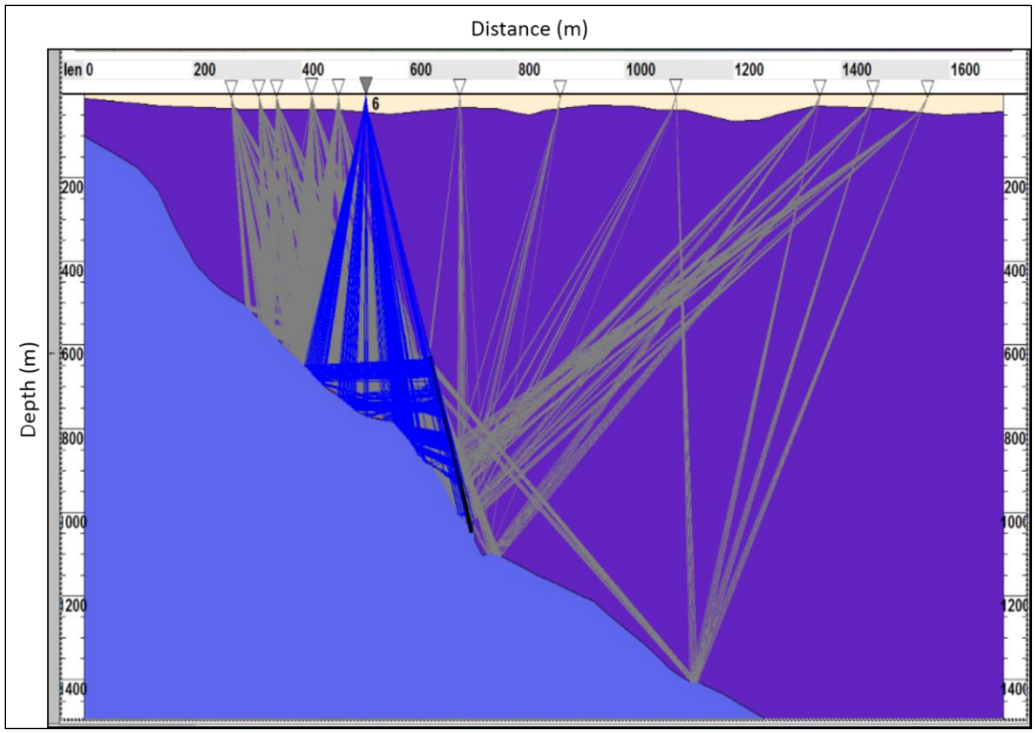

Figure 4-3: Ray path diagram of MVSP survey at McLeay for source positions: -250, -200, -165, -100, -50, 0, 175, 360, 575, 840, 940, and 1040 m; moving in a West-East trend with the western in the negative direction to the borehole collar and eastern in the positive direction. The active shot is at 0 m from borehole collar.

Due to borehole conditions, the FWS and MVSP were surveyed in two sections, a lower section from 926 – 1060 m and an upper section from 625 – 839 m. The reproduced geology log provided by the onsite IGO representative is shown in Figure 4-4. The onsite IGO representative advised it would be too risky to survey in open hole conditions due to the potential of borehole collapse. To survey the lower section, HQ drilling rods were left in the hole to a depth of 920 m and then removed after surveying. Above 633 m, PQ drilling rods were in the hole. With the 24 channel 2 m spaced hydrophone array, multiple pulls of the hydrophone string were required to obtain maximum open hole coverage. As such, multiple shooting was required at each shot point location. These shot holes were drilled in a tight nest configuration. Due to the distance between the sources and the top receiver (minimum 625 m), there was no need to correct for every individual shot in the nest. With 2 m receiver stations, data density was sufficient to avoid spatial aliasing of the tube waves (Greenwood, 2013).

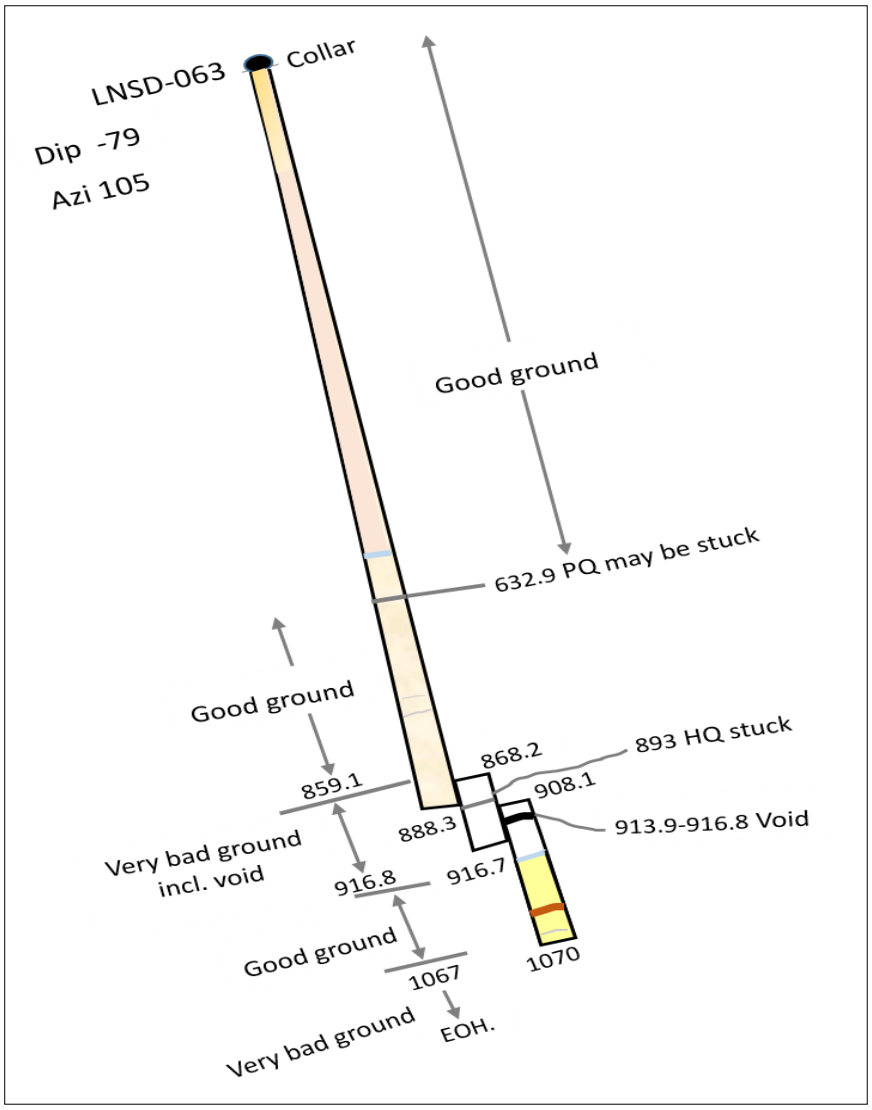

Figure 4-4: Geology log of McLeay nickel sulphide (NiS) mineralization. (Pers. commun., IGO NL).

4.4.1.1. Data processing and migration imaging

The MVSP data was processed by Andrew Greenwood (IGO, 2013, internal report). The resulting hydrophone VSP PSDM image is presented in Figure 4-5. The image is overlying a 2D slice through the SURPAC mine plan and shows drilling records for LNSD-062 and LNSD-063 and its wedges a, b and c. The left-hand ribbon, marked UM/B contact, represents the UM-basalt contact interpreted from 3D seismic and surface drilling (Urosevic and Greenwood, 2010). Kirchhoff Migration used a migration aperture of 0.5 degrees (0.5°) focused to image a 55-degree (55°) dipping structure. The main coherent blue reflector dipping from left to right, indicated by the orange arrow, correlates well with the UM-basalt contact interpreted from 3D

seismic (Urosevic and Greenwood, 2010). The two ribbons on the right, labelled FP, are fault planes also interpreted from the 3D surface seismic.

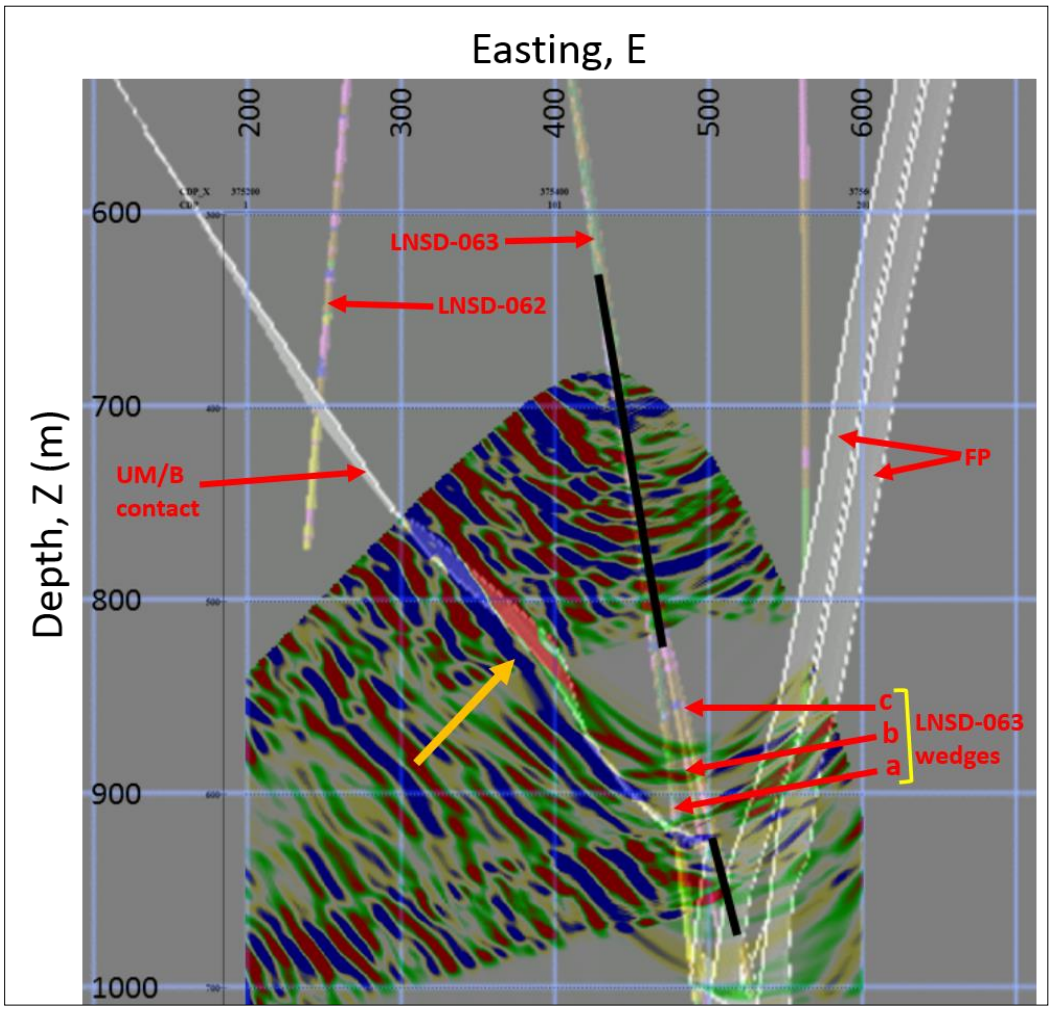

Figure 4-5: Preliminary hydrophone MVSP pre-stack depth migration (PSDM) image focused to image a 55° dipping structure of ultramafic (UM)-basalt (UM/B) interface mapped by the main coherent blue reflector dipping from left to right (marked by orange arrow). The survey has been localized to LNSD-063 wedge c. FP – fault planes.

4.4.2. MVSP synthetic modelling

Figure 4-6 shows the same model as in Figure 4-3 with parametrisation of weathered layer, ultramafic rock layer, and basalt rock layer added. The fault zone dipping to the west was removed from the model to investigate the imaging of the main interface. Same geometry as in the field experiment was used to generate synthetic data. The synthetic seismograms were generated using Tesseral-2D Full Wave modelling package. The modelling parameters used are detailed in Table 4-2.

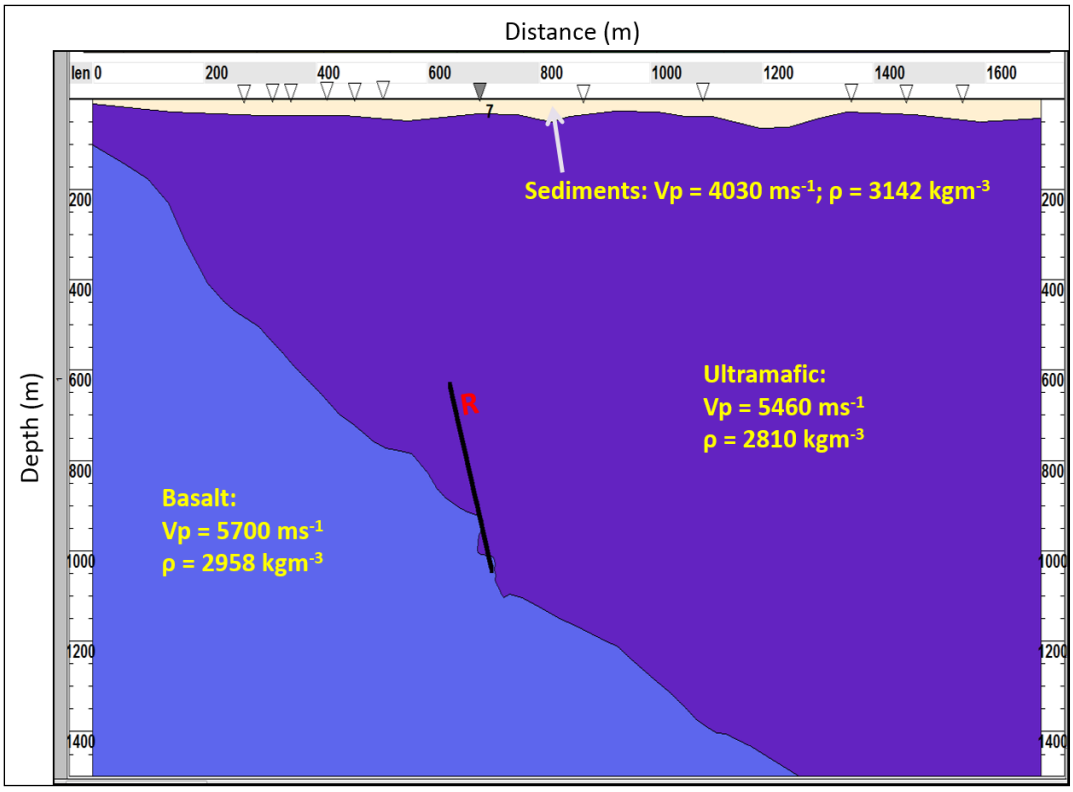

Figure 4-6: Simplified geological model with the sediments, ultramafic, and basalt rock layer parametrised. The original MVSP geometry is employed.

Table 4-2: Modelling parameters for the initial MVSP data generation.

Geometry	Parameters and values				
	Sources	**Receivers**	**Wavelet**	**Sample rate**	**Record length**
Original MVSP with regolith layer	12 variable spacing	214 at 2 m spacing	Ricker 120 Hz	0.4 ms	420 ms

A Ricker wavelet of 120 Hz was chosen for the synthetic MVSP data generation because it is close to the central frequency of the explosive source used for the real MVSP data acquisition.

Figure 4-7 displays the wavefield snap shot taken at 191 ms for shot point 7 and the corresponding synthetic seismogram. The light and deep green broken lines indicate reflections that originate from the UM-basalt contact, as the advancing direct wavefront strikes the dipping ultramafic (UM)-basalt interface at different times. As the receiver array length is short, only a small interface area generates reflected wavefields being recorded. Some up-going multiples including high amplitude

diffracted wavefields arising from the irregular interface of the UM-basalt boundary near the bottom of the borehole have apparent dips similar to the reflected wavefields of interest. The diffracted wavefields are difficult to locate on the energy propagation pane, Figure 4-7 (a), but are indicated as L on the seismogram, (b). These diffracted wavefields have deleterious effects on the bottom borehole interface reflections (yellow broken lines). The amplitude of the direct wavefield is large and overshadows other wavefields present. Reverberation and ringing caused by the low velocity layer are present.

Several raw shot records are shown in Figure 4-8 with the events labelled. The reflection from the UM-basalt is not readily identifiable. The effects of multiple down-going waves reduce with offset and they are observed at later times. The receivers very close to the UM-basalt produce little reflection information.

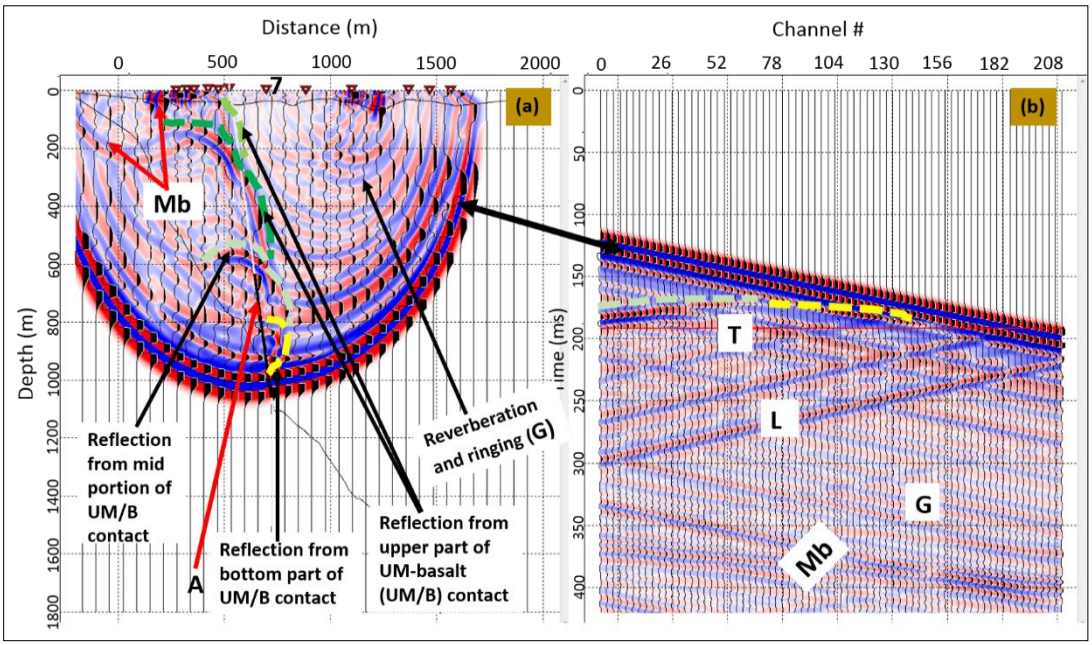

Figure 4-7: (a) Wavefield propagation from shot 7 at 191 ms of the original MVSP geometry. (b) Corresponding synthetic seismogram. Black double-arrow line – direct wave, broken lines (light green, deep green, lighter green, and yellow) – reflections from different parts of the UM-basalt interface, A – portion of the receiver array for effective recording, L - some up-going multiples, G - reverberations from the low velocity layer, and Mb - other multples. T- time-step line.

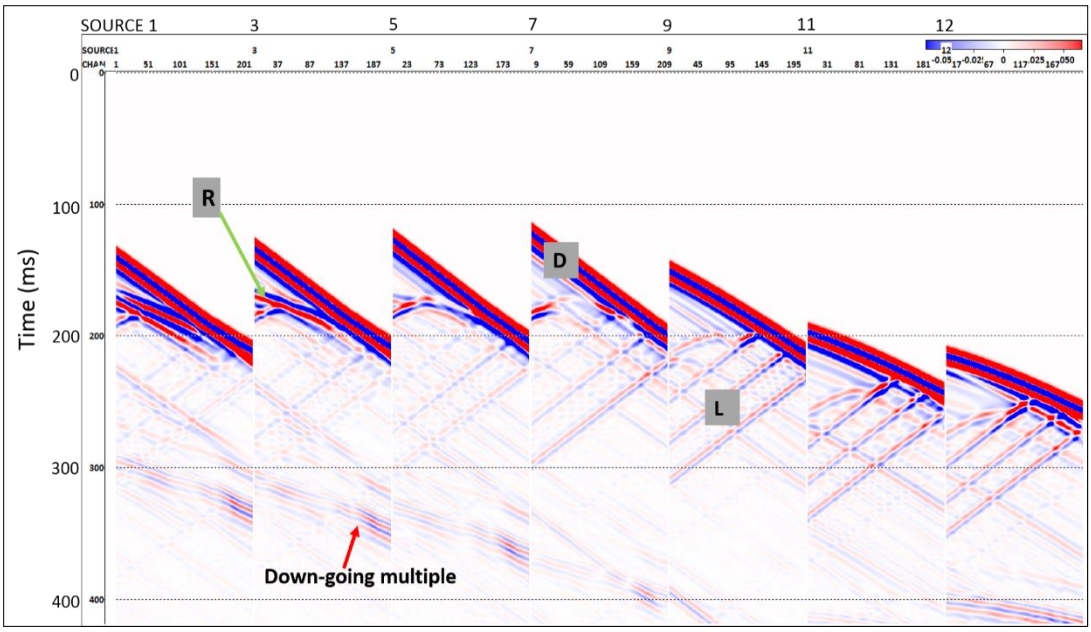

Figure 4-8: Synthetic shot records shown for every 2nd shot. R - reflected wave of interest (from the ultramafic-basalt contact), D - direct wave. Other kinds of wavefield or noise indicated in Figure 4-7 are present.

4.4.2.1. MVSP synthetic data processing and migration

For VSP data to be migrated, the ideal input to the migration programme should be the acoustic (P-wave) reflection response, with all multiple and transmission effects removed (Wiggins et al., 1986). Thus VSP data needs to be processed to preserve the reflected wavefield (Dillon, 1988). The preservation of only reflected wavefields and the removal of other unwanted waves in processing is known as wavefield separation. For synthetic data, as acoustic modelling was used, and no noise added to the data, data processing and wavefield separation processing were straight forward. Data processing and wavefield separation procedure involved the following steps:

- Assigning geometry to the data
- Spherical Divergence Correction
- First break picking
- 2D spatial filtering of direct wave and top muting of direct wave remnants
- F-K filtering of down-going wavefields (quadrant block)
- 2D spatial and F-K filtering of coherent linear wavefields
- Ormsby band-pass filter (10-35-170-250)
- Trace killing of channels below the borehole-interface intersection
- Top muting above the first arrivals to remove filter artefacts

Figure 4-9 displays results of the wavefield processing sequence. Because the borehole is so close to the reflector, the direct arrivals overlap the reflections at lower receivers. Application of F-K filter to remove the direct wave, D, will inevitably remove important detail in the primary reflection. Thus, I tried to remove the direct arrival with 2D spatial filter to recover some of the reflections. The result is presented in Figure 4-9, panel A. Unfortunately, the application of the 2D spatial filter, with varying traces, has not been very effective to remove the direct arrival. Hence, I simply muted the heavy remnants of the direct waves. The F-K filter was effective in removing all the down-going wavefields. The resulting shot records are displayed in Figure 4-9, panel B. Subsequently F-K filter was designed to remove the up-going linear multiples. The resulting wavefield separated shot records are presented in Figure 4-9, panel C. Residual noise is clearly visible.

After wavefield separation, VSP Kirchhoff migration was performed on the up-going wavefields to create depth image. The migration used constant velocity of 5460 ms^{-1}. This is the velocity of the UM layer above the UM-basalt interface. Different migration apertures were tested. Figure 4-10 (a) and (b) show PSDM images obtained respectively at 2° and 5° migration apertures at a preferential dip of 55°. The fidelity and sharpness of the migrated images are very poor and there is no near singular distinct reflection from the UM-basalt interface. Different migration aperture and migration dips were trialled before settling on what is presented in Figure 4-11 as the best image with migration parameters of 10° and 61° respectively. The fidelity and sharpness of the migrated image are far better than observed previously. However, unwanted events which were not successfully removed produced artefacts. Better focussed image towards the centre of the display was produced by using large migration aperture on the expense of diffraction smiles at the edge of the imaging space. Still this migrated image presents near singular distinct reflection from the UM-basalt interface and the dip quite matches the dip of the geologic model.

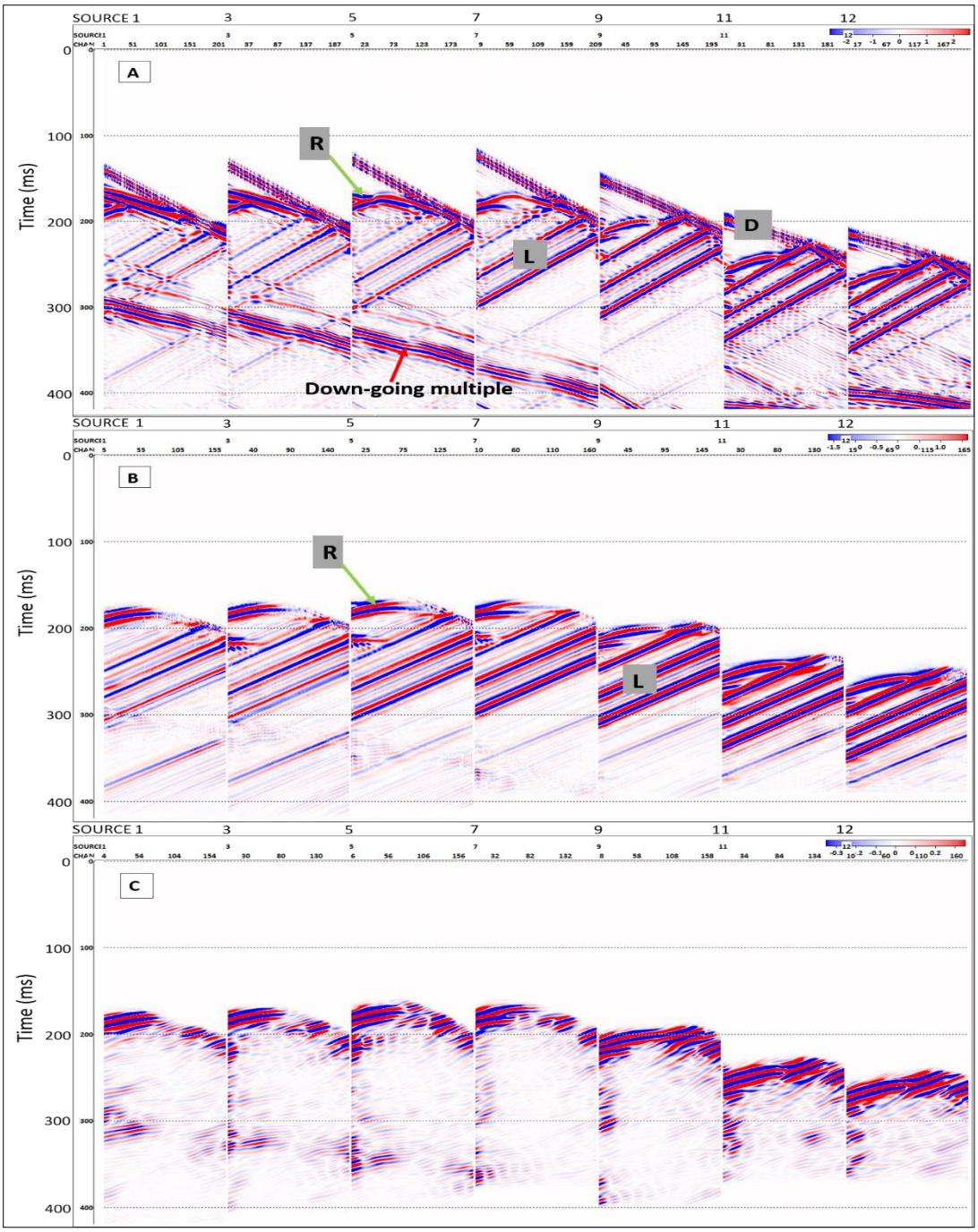

Figure 4-9: Wavefield separating processing: Panel A) 2D spatial filter application (less effect in removing the direct wave), and panel B) top muting the direct wave and F-K filter application to remove down-going multiples. Panel C) the resulting separated wavefield after further wavefield separating processing performed. For each panel, data are displayed for every 2nd shot.

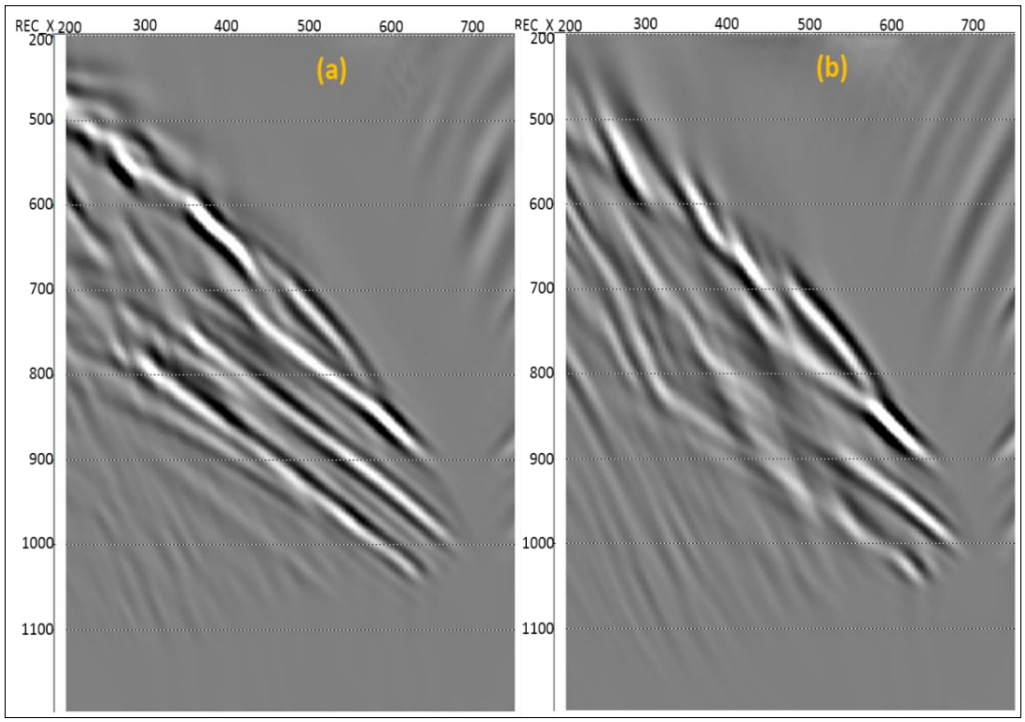

Figure 4-10: Migrated image of the UM-basalt contact at: (a) 2° and (b) 5° migration apertures and focusing dip of 55°.

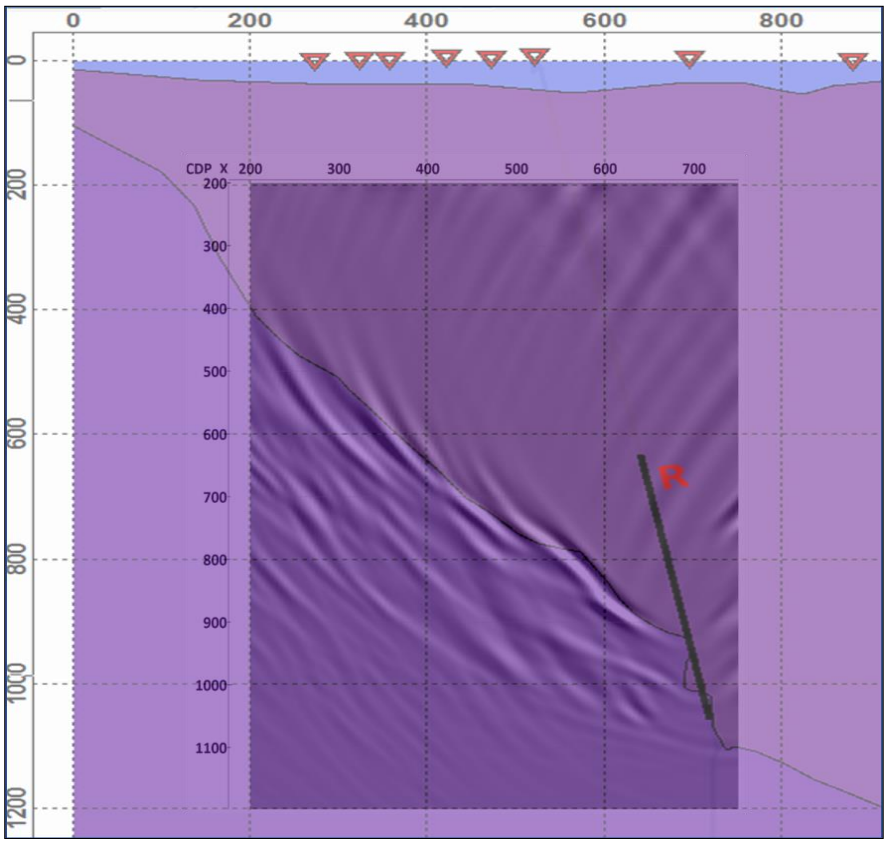

Figure 4-11: Synthetic data image in the presence of the regolith zone overlain with the geologic section. Migration aperture of 10° and 61° preferential slope were used for image generation. The image is displayed as CDP_X against depth.

4.4.3. Comparison of real data and synthetic MVSP migrated images

Figure 4-12 compares the hydrophone MVSP pre-stack depth migration (PSDM) image with the result of the synthetic MVSP image within the same depth space. Except for some differences both images show a reasonable good image of UM-basalt interface. Differences in the images can be explained by the simplicity of the numerical model and the fact that real data has generally lower SNR and includes additional events related to the more complex geological features. In addition, hydrophone data (the real data) are contaminated by tube-waves that overlap the desired P-wave reflections and requires rigorous judicial processing (Greenwood et. al 2012), which degrades the already weak underlying reflection data.

Due to the acute angles of propagation between the receiver borehole and the UM-basalt interface, the proximity of the interface to the receiver borehole as well as the irregular surface of the interface, the process of removal of the down-going P-waves is likely to affect or damage reflected waves of interest close to the borehole. Hence the image around the bottom of the borehole is of a lower quality. This is more pronounced in the real data but resultant image is similar to the modelled one. This comparative analysis confirmed the value of MVSP image and the proposed geological model at the same time.

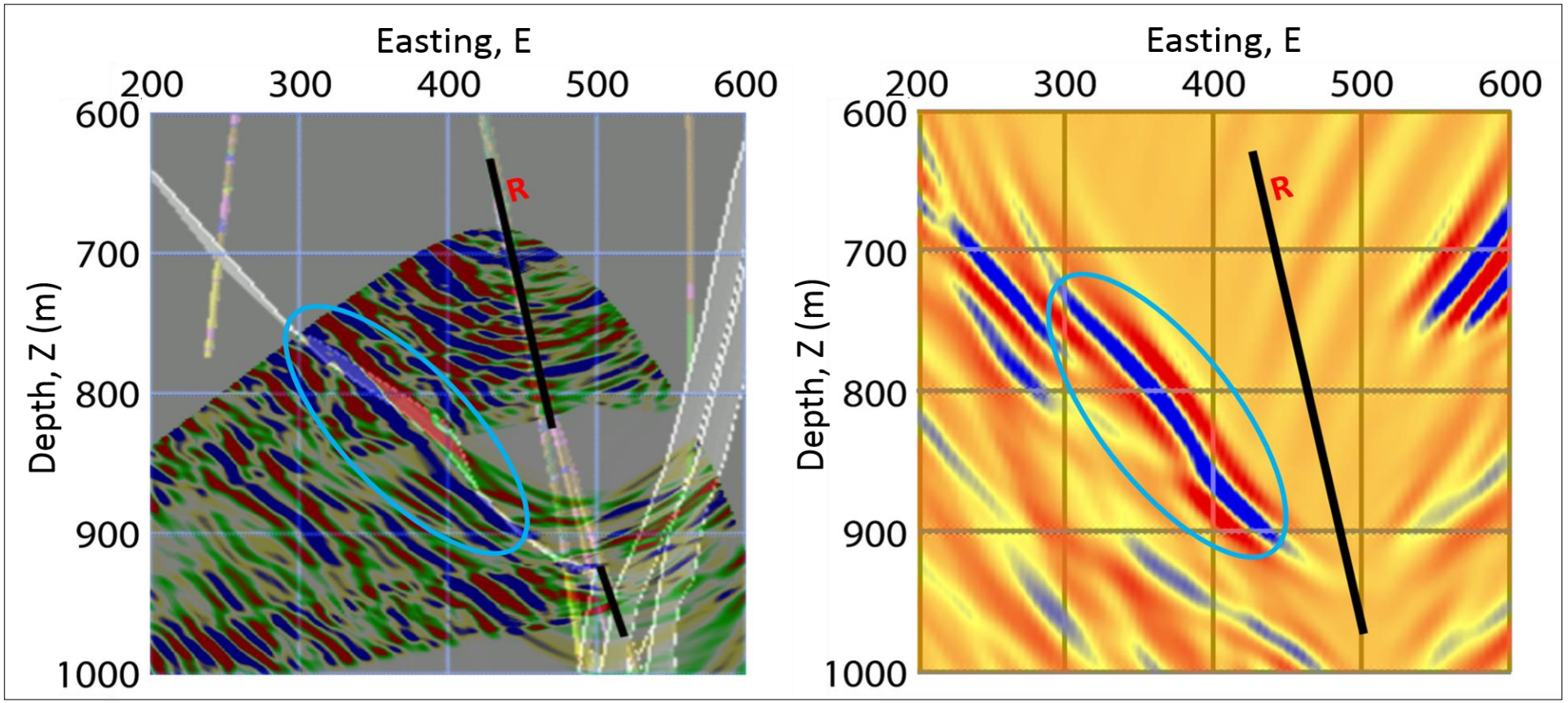

Figure 4-12: The hydrophone MVSP PSDM image (left) and the synthetic image (right) overlain onto SURPAC mine plan There is a good match at the main interface (the UM-basalt interface) as circled. Note: The real and synthetic data were processed with different processing software packages and migration parameters are different. In both images, R represents receiver borehole. Two white ribbons – fault planes.

4.5. Improved MVSP imaging - numerical modelling

It is clear from Figure 4-5 that the fault zone is not imaged in the field experiment. It is likely that this was caused by the limited receiver array. To investigate if this proposition was correct I created another synthetic model which, this time, contained the fault zone as shown in Figure 4-13. This figure is the simplified model in Figure 4-2. For simplicity, the low velocity layer is replaced by the ultramafic layer. Here, the entire length of the borehole is populated by the receivers. This geometry is termed "fully-populated receiver borehole (FPRB)" MVSP geometry.

It is also clear from Figure 4-11 that, synthetic imaging of the UM-basalt interface by the VSP method in the previous section was restricted by the limited receiver array used to mimic the IGO field acquisition. To better compare the MVSP synthetic results with the counterpart CSR results FPRB MVSP is conducted.

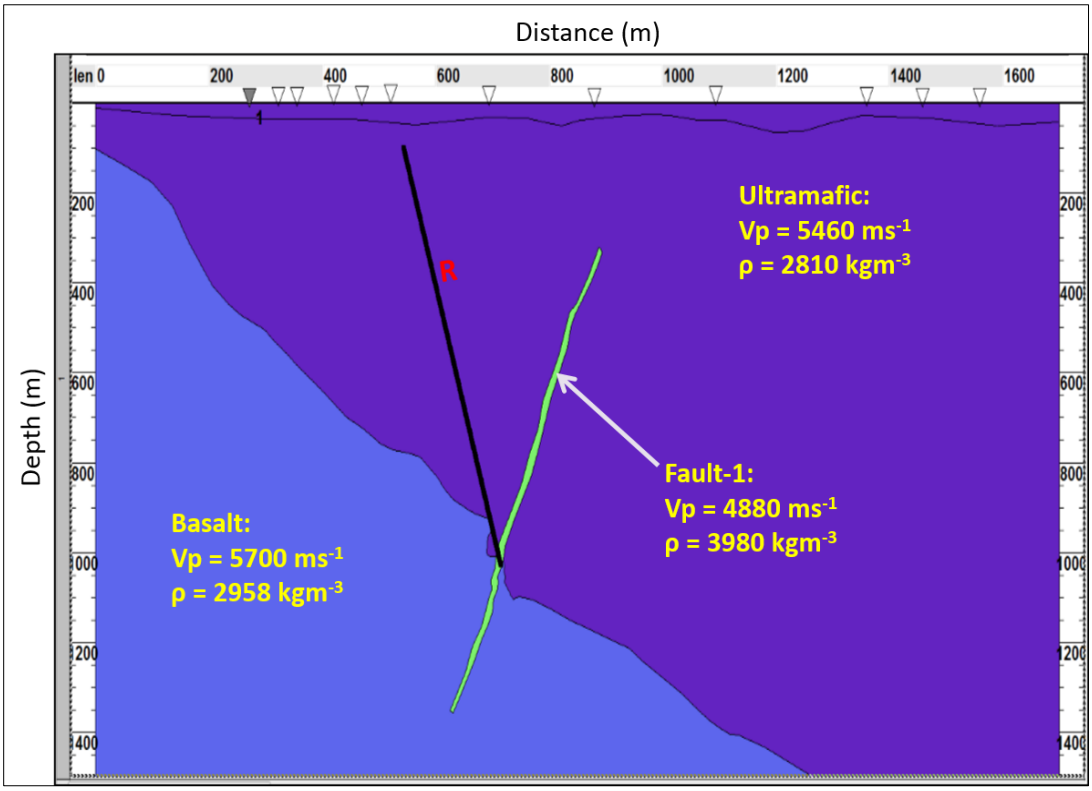

Figure 4-13: Simplified entire geological model of Figure 4-2 with the regolith totally replaced by the ultramafic layer. Shown also is a fully-populated receiver borehole (FPRB) MVSP geometry. Targets to image are the UM-basalt interface and fault-1. The elastic parameters for the modelling are as indicated against the rock layers and the fault in the model.

For convenience, the base geologic model consisting of the komatiitic ultramafic (UM) rock layer, the underlying tholeiitic basalt unit and the low velocity layer with the original receiver array length as in the previous section, Section 4.4, is referred to as MVSP Model 1. MVSP Model 2 has the low velocity layer replaced by the UM layer and has the FPRB geometry incorporated. MVSP Model 3 has everything as MVSP Model 2 but, in addition, has the fault structure incorporated.

4.5.1. MVSP acoustic numerical modelling

For the modelling experiment, I adopted a step-by-step approach by first considering modelling the UM-basalt interface with the FPRB MVSP geometry. The fully populated borehole has a total number of 481 receivers but at 2 m spacing as in the previous case. Other modelling parameters remained the same as presented in Table 4-2. In Figure 4-14, numerical shot records generated for the same surface position for MVSP Model 2 and for MVSP Model 1 (in Section 4.4) are compared.

As expected, long receiver array produced reflections from much larger area. This could have been achieved in the field experiment by successive move-up of the hydrophone string and appropriate repetition of surface shot positions.

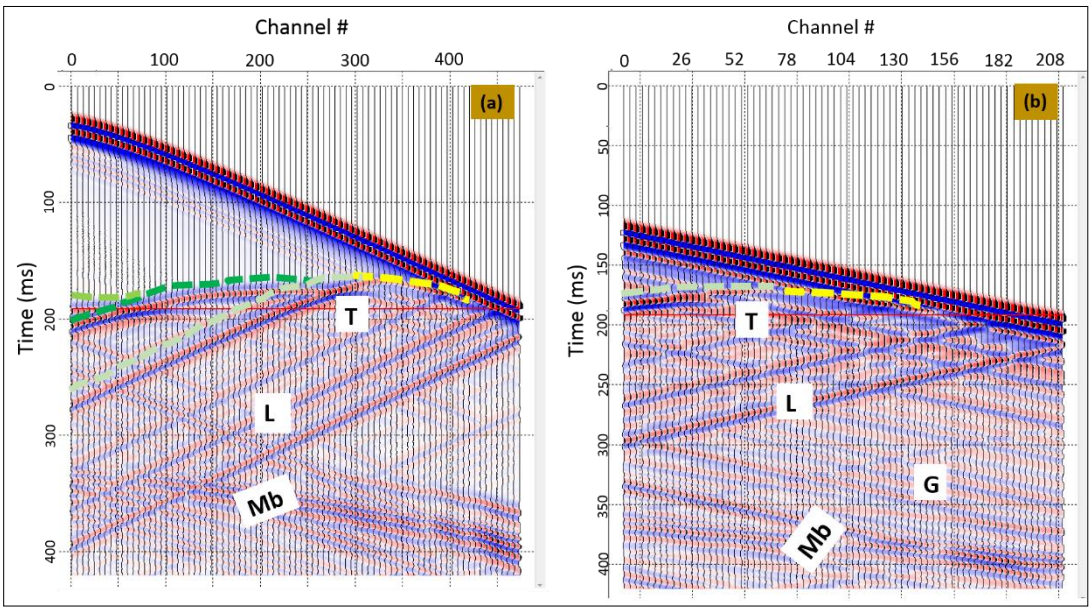

Figure 4-14: Comparison of seismograms at 191 ms from shot 7 for MVSP geometries generated with the: (a) fully-populated receiver borehole (FPRB) (MVSP Model 2) and (b) original shot receiver array (MVSP Model 1). Colour code broken lines and annotations have similar meaning as previously indicated. Note: MVSP Model 1 has the regolith hence G (reverberation and ringing from the low velocity layer). In MVSP Model 2, the UM layer replaces the regolith.

Although synthetic data can be generated for multiple targets in a single computation, the approach to add additional target was step-wise. This was to simplify the observations and understand the contributions of wavefield patterns from each target in the seismograms. Thus, my modelling experiment now considers the full migration space and fully populated borehole as in the case for MVSP Model 2 with the steeply dipping fault (fault-1) now incorporated (into MVSP Model 2). As mentioned earlier, this model is named MVSP Model 3 and is the entirety of Figure 4-13. Using the same modelling parameters as before, synthetic data were generated for MVSP Model 3 in the same manner as in the previous cases.

Mixed reflection patterns from the UM-basalt contact and fault-1 vary and are complex at certain points. The shot records of two shot points 3 and 7 located respectively in the up-dip and down-dip sides of the borehole collar are shown in Figure 4-15. Reflections from fault-1 are indicated by the orange and the dark-gold broken lines and the other colour codes indicate reflections from the UM-basalt contact. It is clear that the shot point 3 in the up-dip direction produces strong reflections from the fault. Observed fault reflection suggest that imaging could be successful in mapping it.

Migration of the wavefield separated profiles, however, was done using two different approaches and results compared. In one approach, migration was performed in two steps to separately image both the fault and UM-basalt interface. This is because the targets have different dips and yet the migration algorithm window can only have one preferential slope assigned. Thus, the first migration which targeted the UM-basalt contact used the same migration parameters in MVSP Model 1, but the migration image space has been increased from 200 - 750 m to 0 - 750 m. The fault imaging used a migration image space from 600 to 1100 m; migration aperture of 8°, and preferred image slope of 68°. The two depth migrated sections were then merged (stacked) into a single section with overall migration image space of 0 to 1100 m. The resulting image with MVSP Model 3 geologic section overlain is displayed in Figure 4-16.

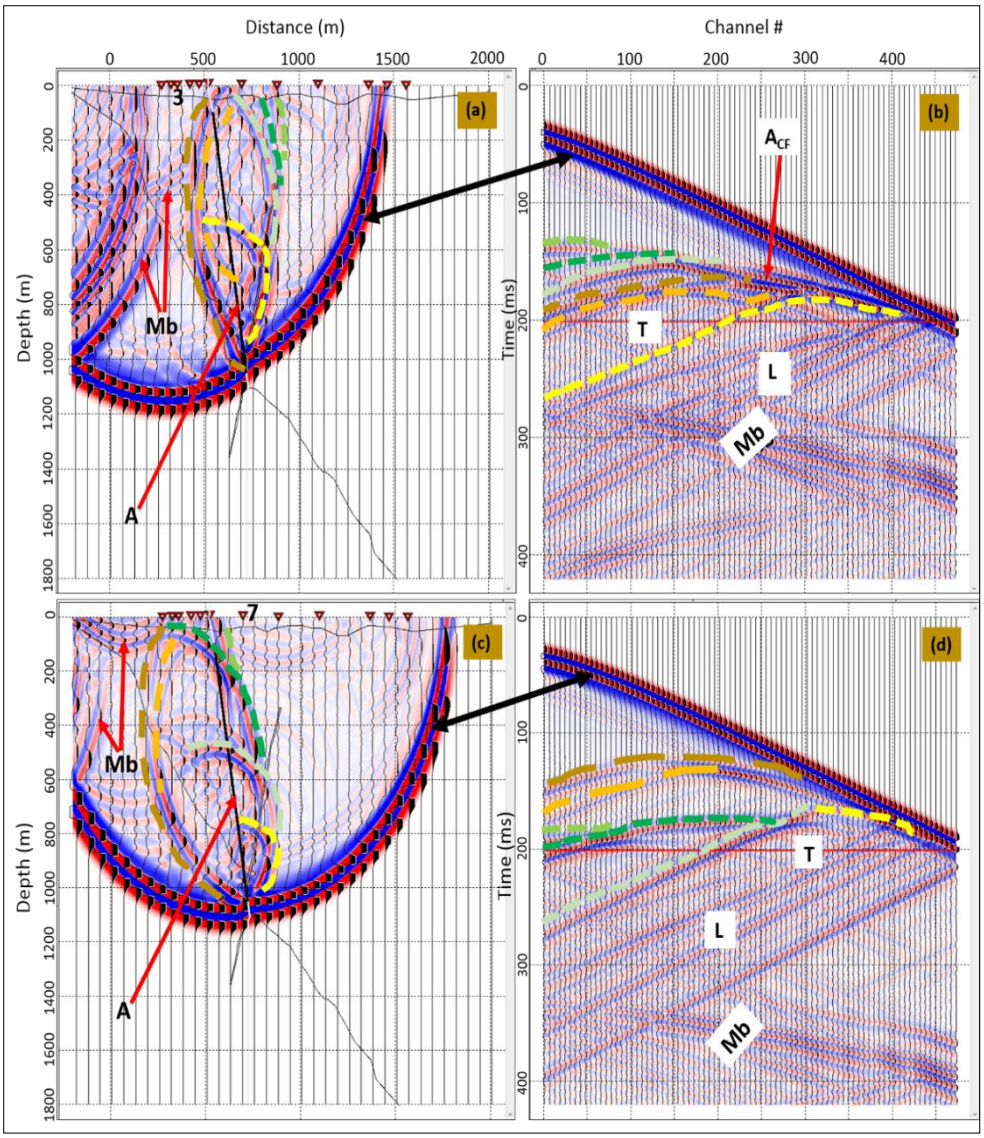

Figure 4-15: Comparison of wavefield propagation and the corresponding synthetic seismogram at 201 ms; top panel: (a) and (b) for shot point 3, bottom panel: (c) and (d) for shot point 7. Shot points 3 and 7 are located at geologically up-dip and down-dip sides respectively of the zero-offset shot point, shot point 6, location. The dark orange broken line and the dark-gold broken line indicate reflections from fault-1. Other colour broken-lines indicate reflections from the UM-basalt contact as shown earlier in Figure 4-14. A_{CF} indicates complicated overlapping reflections from both the UM-basalt contact and fault-1. All other symbols and annotations have same meaning as observed in similar sections of MVSP geometry.

The second approach intended to observe how the targets with different dips could be imaged, compared with the above, if the entire section is considered and one preferential slope is assigned to the migration algorithm. Thus, in performing migration of the wavefield separated profiles, a migration image space from 0 to

1100 m was used and to a depth of 1200 m. A migration aperture value of 12° and image focusing dip value of 66° provided the best image after different migration aperture and preferential slope tests were trialled. This image, overlain with the geologic section, is shown in Figure 4-17. Comparing Figure 4-16 with Figure 4-17, arguably Figure 4-17 displays a weakening reflected amplitude at certain parts of the UM-basalt contact imaged indicated with green arrows. Artefacts are present on the migration sections with major ones below the fault but more pronounced on Figure 4-17 as indicated with the yellow arrows. The presence of the artefacts may be due to multiple factors such as insufficient wavefield separation, late time events, and migration related issues. Smearing of the migrated images due to migration effects are red circled. These observations notwithstanding, both migrated sections mapped the geology of interest quite well.

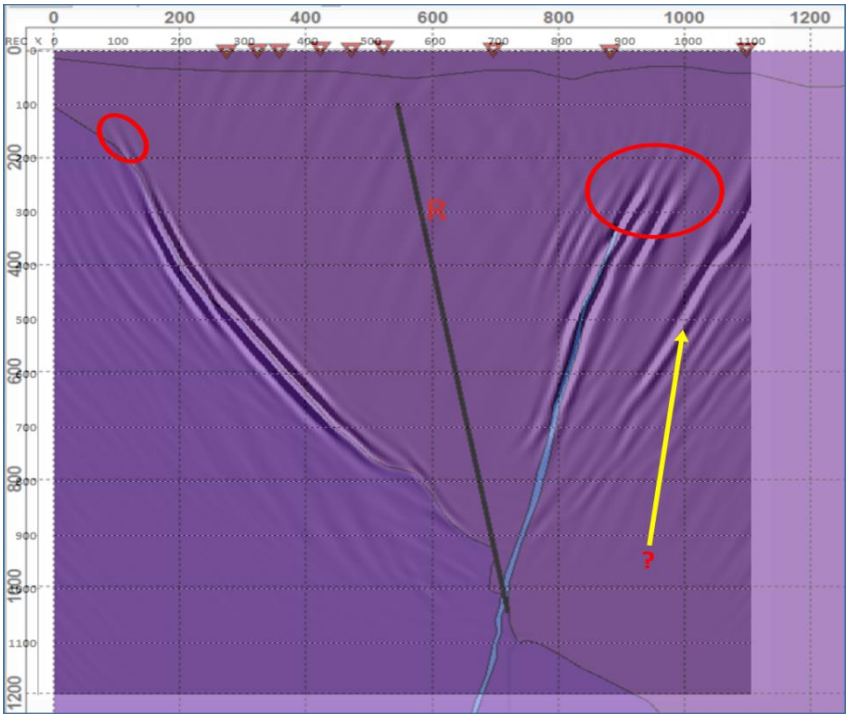

Figure 4-16: The resulting stacked image. Fault-1 image migration used image space of 600 to 1100 m; migration aperture value of 8°; preferential focusing dip of 68°, and image depth of 1200 m. UM-basalt interface image migration parameters: A migration aperture of 10° and 61° preferential slope as in Figure 4-11 (MVSP Model 1), but the migration image space is from 0 to 750 m (instead of from 200 to 750 m) and image depth from 0 to 1200 m (instead of from 200 to 1200 m). The red circled portions indicate extensions in images of targets caused by migration effects. The yellow arrow indicates a major artefact below the fault.

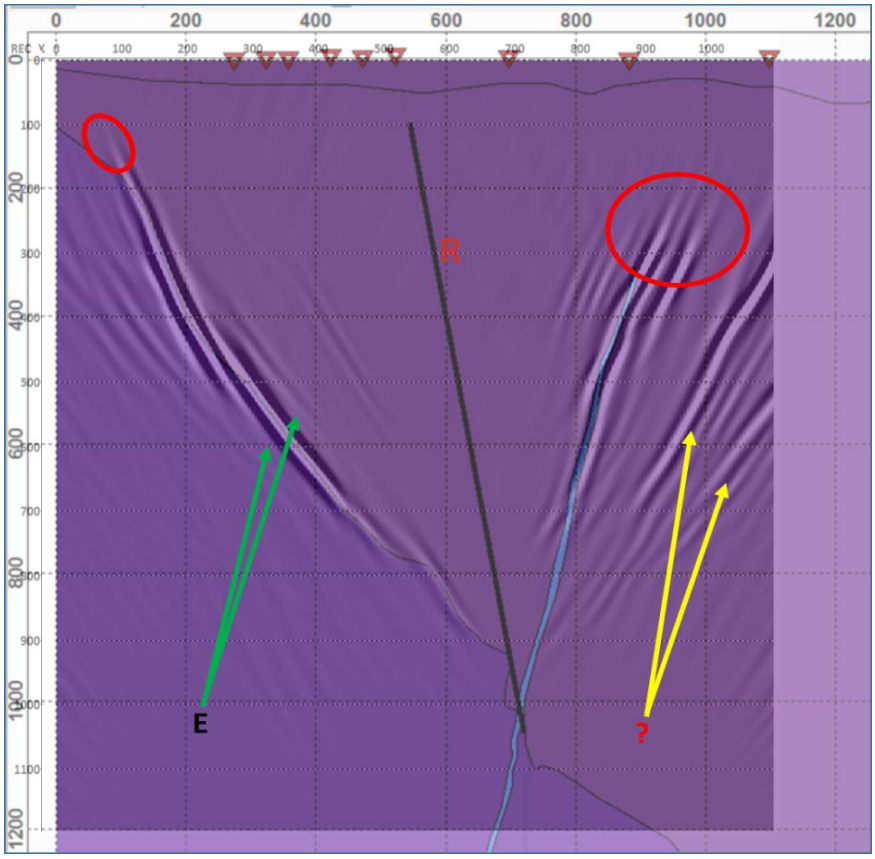

Figure 4-17: Depth image using single pass migration. Migration image space is 0 to 1100 m; aperture value of 12°; a preferential slope of 66°; and image depth of 1200 m. Green arrows (letter E) indicate weakening reflected amplitudes. Other indications have same meaning as in Figure 4-16.

4.5.2. CSR acoustic numerical modelling

The result of VSP imaging in the previous section was satisfactory despite some artefacts generated in the imaging process. It is now of interest to observe if CSR imaging can produce equally good or better image than MVSP. To test effectively the imaging capability of the CSR method and to make a proper comparison with the MVSP synthetic results, the partially and fully populated receiver borehole geometries as in the MVSP modelling were considered for the CSR modelling. To make the CSR analysis relevant to the real field investigations the eastern borehole as shown in Figure 4-2 was populated with sources for the numerical experiment. While the geometry of the boreholes does not appear favourable for CSR imaging, it resembles the real field situation. The CSR Model to be tested is shown in Figure 4-18 and shown only for the FPRB geometry. CSR results obtained are compared with the counterparts MVSP results in the next subsection. The elastic parameters for

synthetic data generation are provided on the model and the modelling parameters provided in Table 4-3.

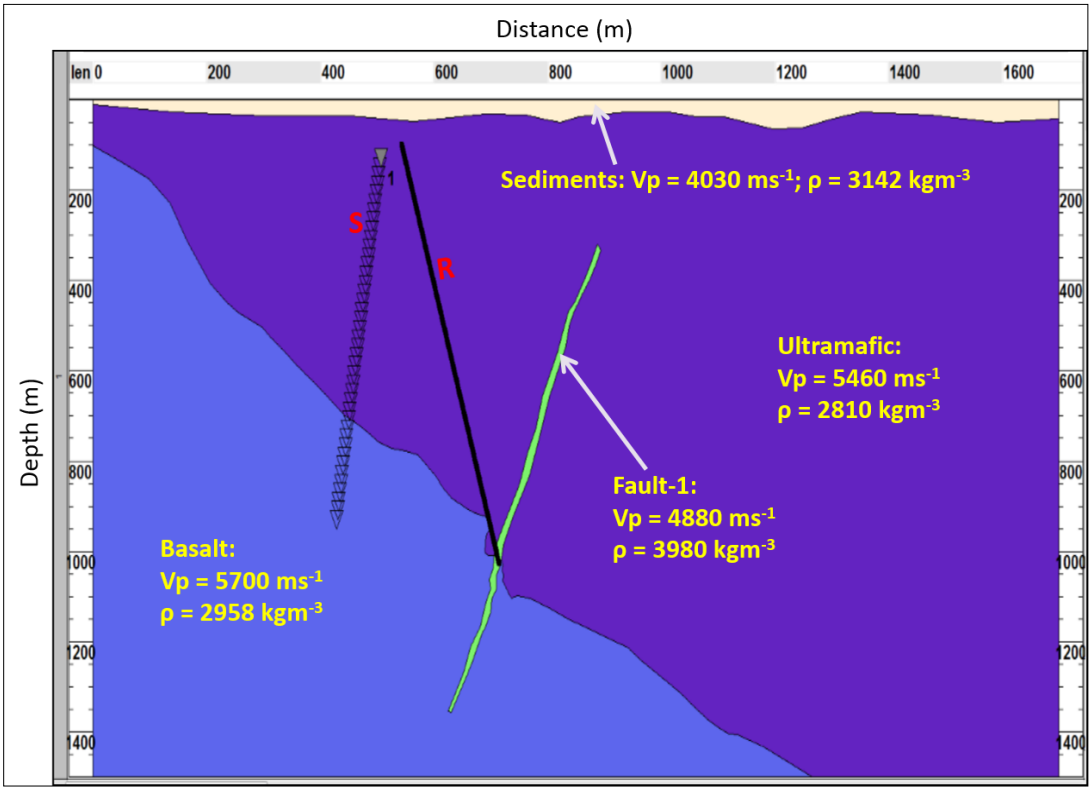

Figure 4-18: Simplified entire geological model for a fully-populated receiver borehole (FPRB) geometry for CSR Model 2 (without the fault) and CSR Model 3 (with the fault). Targets to image in CSR Model 2 is the UM-basalt interface and in CSR Model 3 are the UM-basalt interface and fault-1. The elastic parameters of rock layers and the fault are as indicated in the geologic model.

Table 4-3: Modelling parameters for all the CSR synthetic data generation. The three geometries case studies are counterpart cases considered for MVSP modelling.

Type of Geometry	Parameters and values				
	Sources	**Receivers**	**Wavelet**	**Sample rate**	**Record length**
Original CSR	41 at 20 m spacing	214 at 2 m spacing	Ricker 120 Hz	0.4 ms	250 ms
CSR with fully-populated receiver borehole	✓	481 at 2 m spacing	✓	✓	320 ms
CSR with fully-populated receiver borehole and fault-1	✓	✓	✓	✓	420 ms

4.6. CSR method authentication - MVSP and CSR pre-stack depth migration (PSDM) images comparison

Figure 4-19 compares the numerically generated wavefield propagations and the corresponding seismograms for the MVSP and CSR. These were generated with the limited receiver array used to mimic the IGO field acquisition. In the figure, (a) and (b) are the respective wavefield propagation and seismogram for the MVSP geometry for the 7th shot point at 191 ms and (c) and (d) the respective ones for CSR geometry for the 15th shot point at 106 ms. One clear difference is that the reverberation and ringing caused by the low velocity layer observed in the MVSP data are absent in the CSR section. Then, the bottom borehole interface reflections (yellow broken lines) recorded in the MVSP geometry sections (Figure 4-19 (a) and (b)) are not observed in the CSR geometry sections (Figure 4-19 (c) and (d)). The limited receiver array length restricted the amount of data recorded in both geometries but the source-receiver geometry of the MVSP geometry seems to favour (more) recording of reflections from the bottom part of the UM-basalt contact (yellow broken lines) than its upper part and the vice versa for the CSR geometry as reflections from the upper part of the interface – the deep green broken lines – are observed in the CSR geometry wavefield propagation snap and the corresponding synthetic shot record sections but absent in the MVSP geometry synthetic shot record section. This may lead to each geometry imaging different portions of the UM-basalt interface.

Figure 4-20 compares the PSDM images of the UM-basalt contact obtained with the MVSP geometry and CSR geometry using the restricted receiver array. The images are overlain with the respective geologic section. The two images compare quite well in terms of resolution as the same frequency source was used for both. But the lateral coverage and depth of the UM-basalt contact imaged by each geometry is different. The geometries imaged different portions of the UM-basalt interface according to the assertions made earlier. While the CSR geometry imaged more up-dip than down-dip part of the UM-basalt interface, the migrated image obtained with the MVSP geometry is deeper and closer to the receiver borehole than that of the CSR geometry.

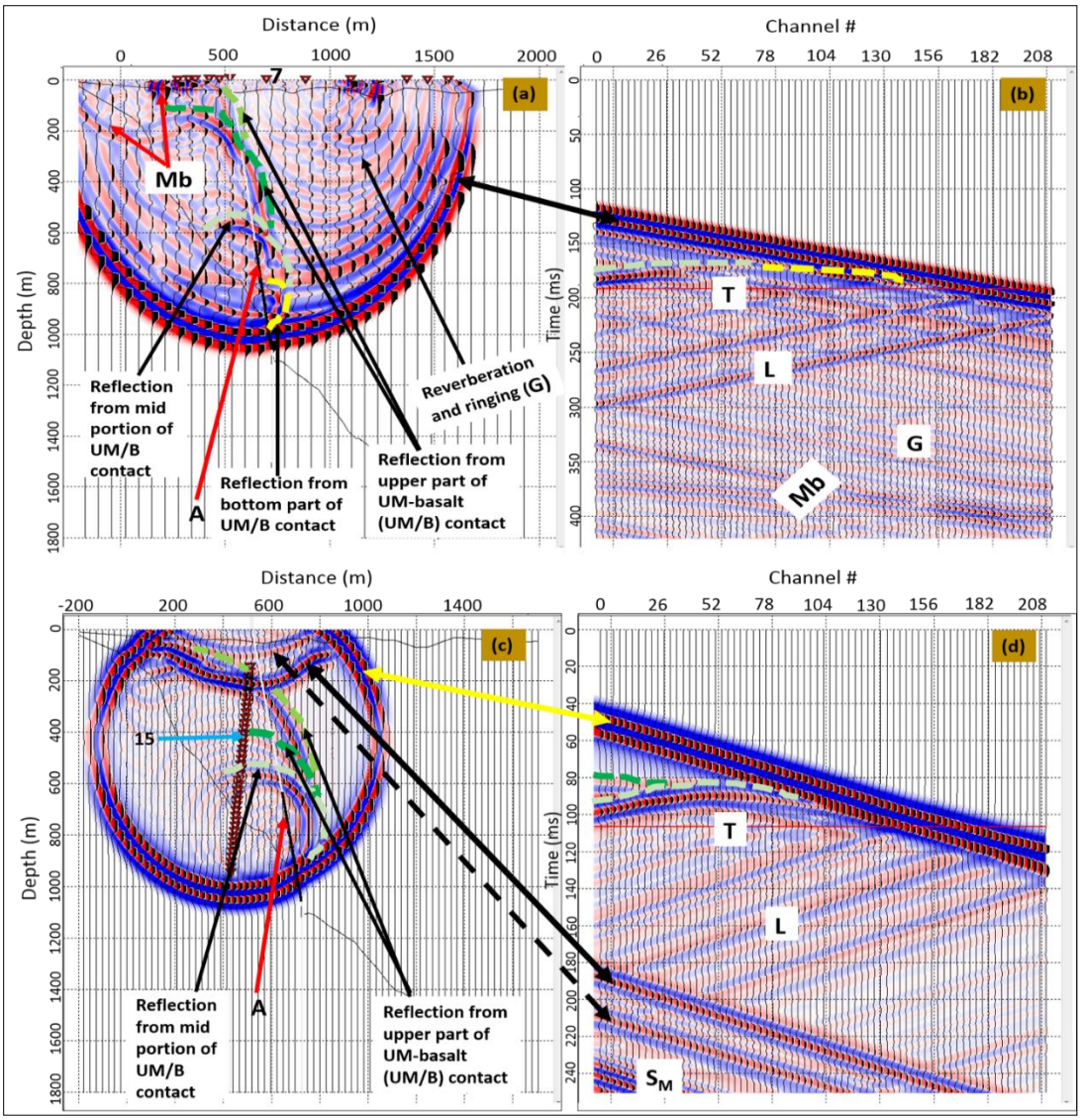

Figure 4-19: Wavefield propagation (left) and the corresponding seismogram (right) for original MVSP and CSR geometries. Top panel: MVSP geometry for shot point 7 at 191 ms; Bottom panel: CSR geometry for shot point 15 at 106 ms. For the CSR geometry, yellow double arrow line – spherically propagating direct wave, black solid double-arrow line – down-going multiples of direct wave reflected from UM-sediment interface, black broken double-arrow line – direct wave surface reflected down-going multiples, and S_M – surface reflected down-going multiples. All other broken lines and annotations in the figure have similar meaning as in Figure 4-7.

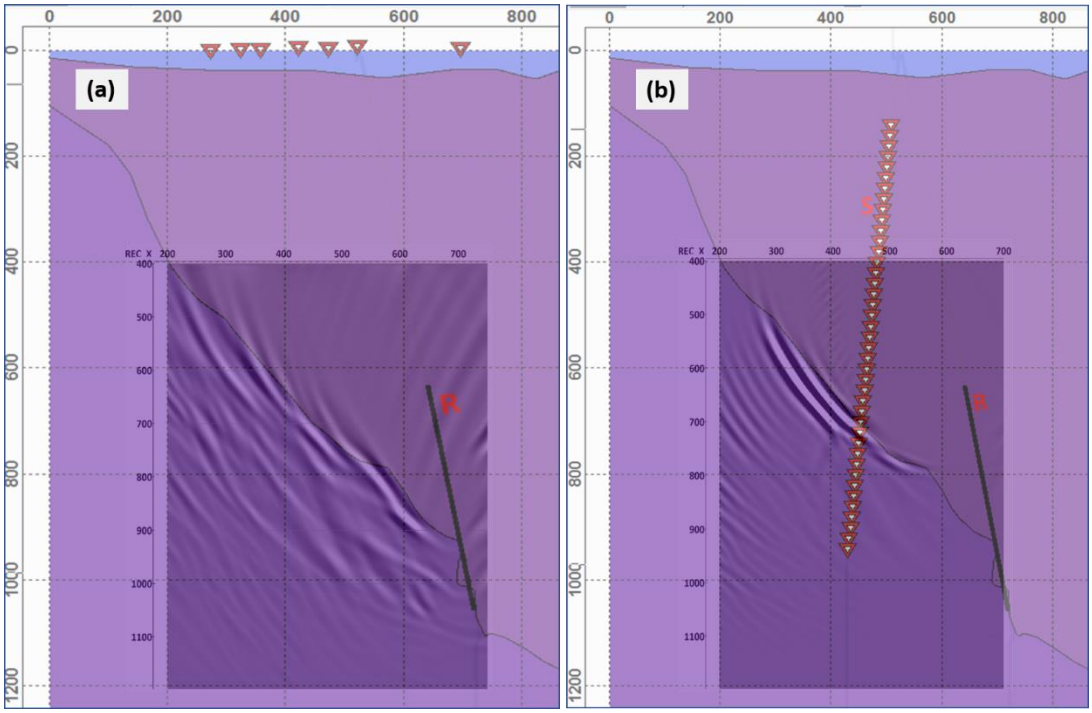

Figure 4-20: Comparison of the UM-basalt contact synthetic PSDM images with the overlain geologic models for the two different geometries. (a) With the original MVSP geometry and (b) with the original CSR geometry.

The results of the FPRB geometries are then compared in order to have a better migrated image representative of the UM-basalt interface and also to better compare the imaging capabilities of the two geometries. Figure 4-21 compares the PSDM migrated images of the UM-basalt interface obtained by the two methods with the FPRB geometries. We observe that images obtained with both geometries image the UM-basalt interface well. However, CSR image is shorter than that of MVSP but is superior and maps the UM interface very well. Finally, with the FPRB geometries, the imaging capabilities of the two methods are compared using the full migration space and single pass PSDM. The results are shown in Figure 4-22. In both methods, however, the dip and depth of the UM-basalt interface and the fault are preserved, and the migrated images contour the geology to a high degree of accuracy. But, again, the CSR geometry provides a superior migrated image that correlates and contours the UM-basalt interface and the fault structure better than that of the MVSP geometry. More migration artefacts are prevalent on the MVSP migrated section than on the CSR migrated section.

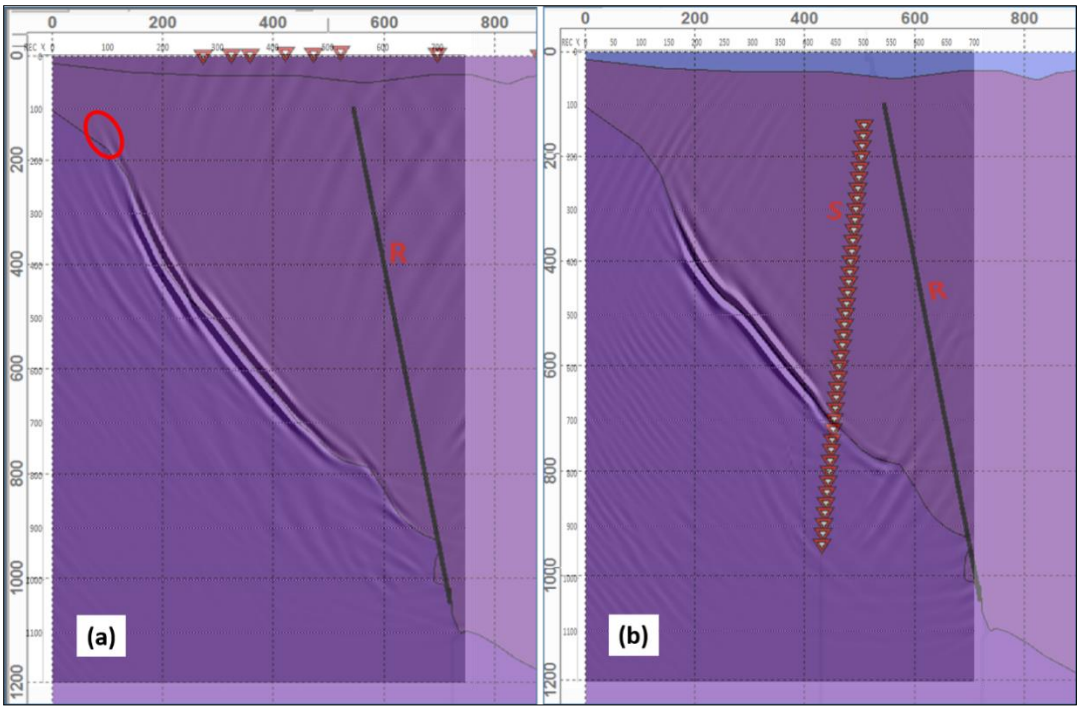

Figure 4-21: Comparison of UM-basalt interface imaged using fully populated receiver borehole geometry: (a) MVSP and (b) CSR result. The red circled portion indicates extension of image caused by migration smile.

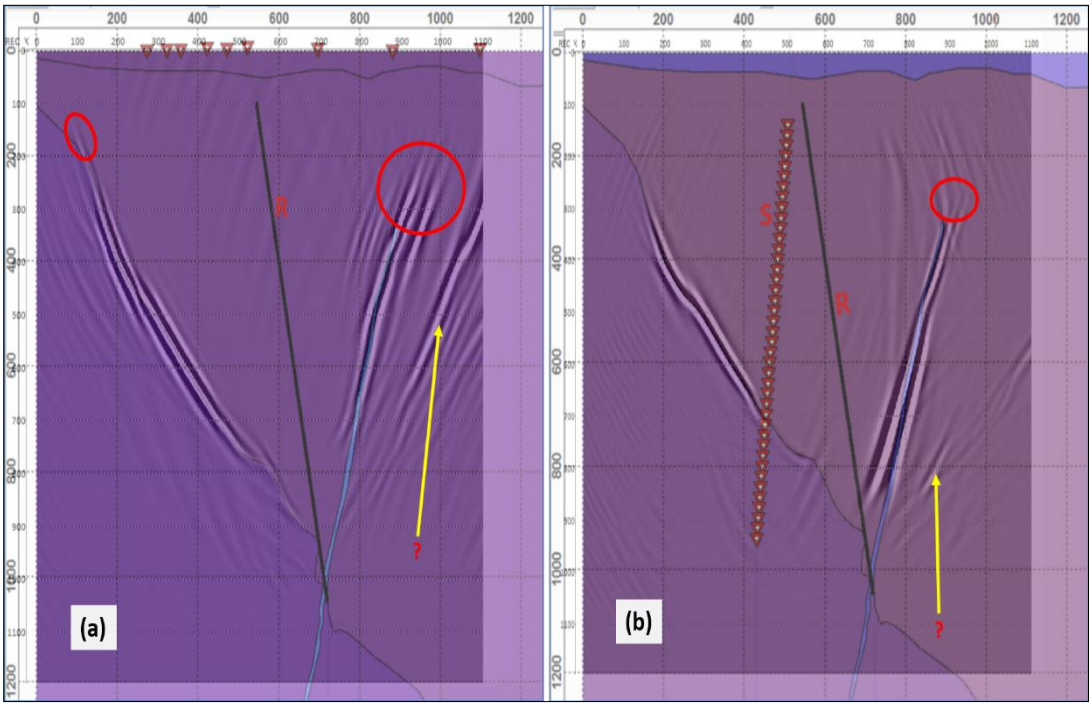

Figure 4-22: Comparison of (a) MVSP and (b) CSR migrated images for the full migration space. CSR image is by far of a superior quality despite having some imprecisions as indicated with red circle.

4.7. Summary

Both methods successfully mapped the UM-basalt interface and fault-1. The extent of CSR image is marginally shorter in comparison to MVSP but in much better agreement with the geology for the fully populated receiver borehole. The fault zone is much better reconstructed with CSR method. Migration smearing is observed in both sections but far more pronounced in the MVSP image. Imaging artefacts are much smaller for CSR result. The artefacts are most likely caused by migration of diffracted waves or from late time events or even from both. As noted for in hard rock environment, pointed and irregular/rough edges serve as energy scatters or diffraction points. The scattered energy is not focused for proper imaging. Incorrect imaging of the scattered energy and migration of late time events may manifest in the migrated section as secondary reflections. Finally, apparent multiple fault zones produced by MVSP imaging are disturbing. They could be largely result of the processing and partially successful wave separation in MVSP data.

This comparative study produces first insight into imaging capability of the CSR method. For the case history shown, the ultimate answer could be achieved by conducting the field experiment similar to the modelling study presented here. Numerical experiment results suggest that CSR method is likely to produce highly precise depth image of the underground for McLeay type nickel sulphide deposit.

5. Application of crosshole seismic reflection to delineate Maggie Hays style nickel sulphide mineralized zones

5.1. Introduction

Peters and Buck (2000) reported that the initial discovery of Maggie Hays deposit was not owed to geophysics but the discovery of Maggie Hays North and the subsequent discovery of its nearby Emily Ann massive nickel sulphide deposits were largely the results of surface time-domain electromagnetic (TEM) and downhole TEM (DHTEM) geophysical techniques application. Despite these successes, the challenges of misguided delineation of the ore-bodies and finding mineralization extensions to the existing ones are far from over.

Maggie Hays deposit and its environs have a regolith of varying thickness which exhibits variations in thickness conductivity and magnetization both laterally and vertically. In some areas, the problem is compounded by the substantial thicknesses of conductive salt-lake sediments (Trench and Williams, 1994). In addition, the Maggie Hays (and Emily Ann) nickel sulphide deposits are not outcropped but blind to discovery as they are hidden by transported cover rocks. More so, and with particular reference to the Maggie Hays deposit, the westerly laid banded iron formation (BIF) hosted barren massive sulphide zone is in close proximity to the nickel sulphide mineralization. This zone is as conductive as the massive nickel sulphides and its response (the BIF zone) to EM signals can interfere strongly the EM response from the nickel sulphide mineralization (Peters and Buck, 2000). Furthermore, the Maggie Hays style massive nickel sulphides are geometrically sub-vertical to steeply oriented making Maggie Hays extension essentially blind to EM discovery.

The seismic impedance of the massive nickel sulphide zones, however, is in high contrast to the host rock. Therefore, seismic methods could possibly be employed for the ore-bodies' delineation and extensions. But the conventional surface seismic application will have some challenges such as time delays and attenuation related to

the complex regolith. Furthermore, reflections from such semi-vertical and steeply dipping structures will not be directed to the surface for effective data collection (Greenwood, 2013) and for subsequent imaging of the subsurface reflectors although in a rare case, steeply dipping gold-bearing structures were successfully imaged by a 2D surface seismic (Urosevic et al., 2016) below a relatively thin regolith layer.

With the above factors, the CSR method may complement seismic images or even be a better alternative to surface seismic. This study, through a series of numerical experiments, aims to evaluate CSR capability for imaging and delineation of steeply dipping Maggie Hays nickel deposits.

5.2. Maggie Hays nickel sulphide mineralization: regional location and geological setting

The Maggie Hays and Emily Ann nickel sulphide deposits together with a series of smaller nickel sulphide deposits are hosted within the Lake Johnston Greenstone belt in the south-eastern portion of the Youanmi Terrane of the Archaean Yilgarn Craton of Western Australia (Swager, 1997; Cassidy et al., 2006) as presented in Figure 5-1. The two mines combined have a (pre-mined) total resource of approximately 140,000 tonnes of contained nickel (Buck et al., 1996; 1998). The Lake Johnston Greenstone belt is divided into three formations, from East to West: the Maggie Hays, Honman, and Glasse Formations (Gower and Bunting, 1976; Heggie, 2010; Heggie et al., 2012). Of the Formations, only the Honman contains komatiites. The Honman Formation itself is subdivided into three ultramafic units, from east to west: Eastern Ultramafic Unit (EUU), Central Ultramafic Unit (CUU), and Western Ultramafic Unit (WUU) (Wang et al., 1996; Heggie et al., 2012). It is the CUU and the WUU that are associated with nickel mineralization and the Maggie Hays nickel deposit is hosted within the CUU (Peters and Buck, 2000; Barnes and Perring, 2007; Heggie et al., 2012).

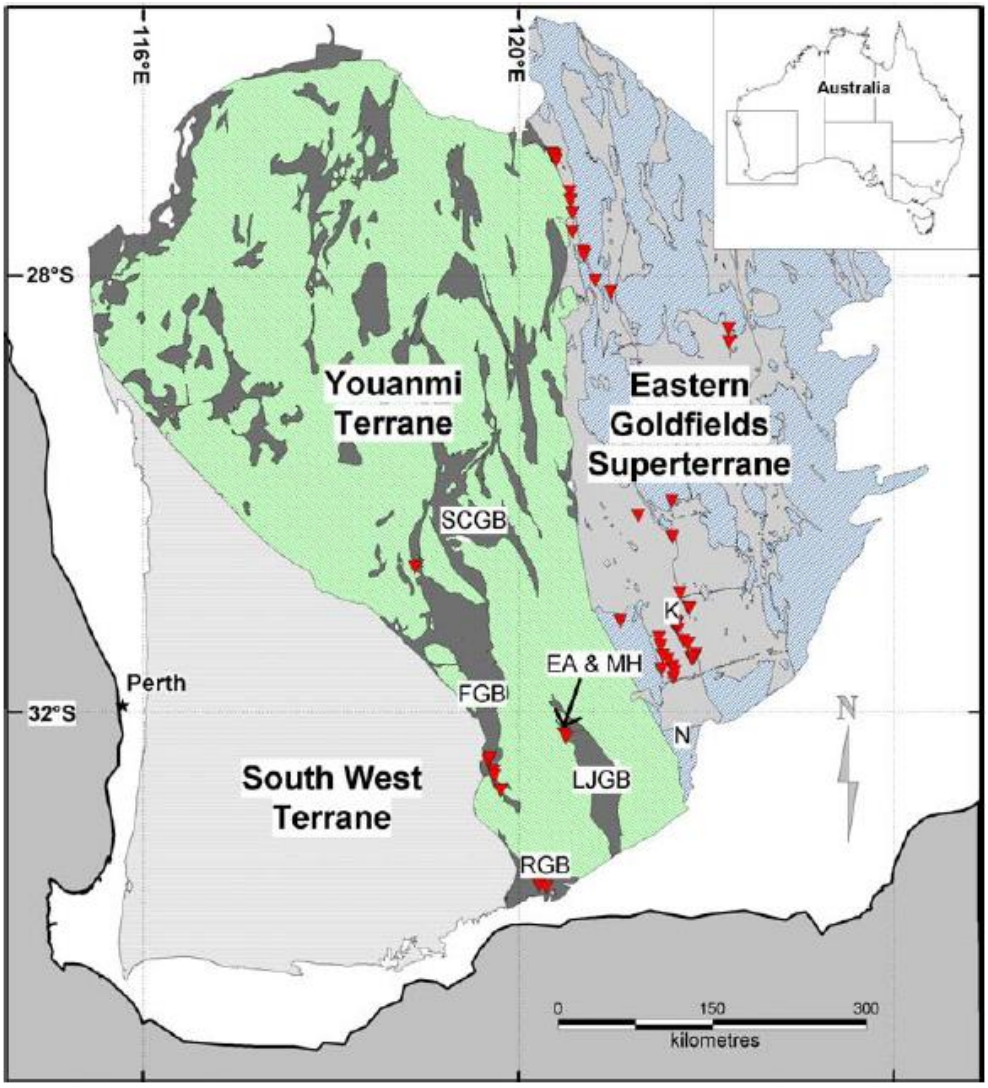

Figure 5-1: The Yilgarn Craton and some of its major subdivisions. Youanmi Terrane granite-greenstone belts include the following Greenstone belts (GB), in dark grey: Lake Johnston (LJGB), Ravensthorpe (RGB), Forrestania (FGB), and Southern Cross (SCGB). Komatiite-hosted nickel mines are shown by red diamonds. Lake Johnson Greenstone belt nickel mines include: Emily Ann deposit (EA) and Maggie Hays deposit (MH). Shown in the Eastern Goldfields Superterrane are: Norseman (N) and Kalgoorlie (K). Modified from (Joly et al., 2008) and (Heggie, 2010).

Figure 5-2 shows, among other geological features, the geological setting of the Maggie Hays and the nearby Emily Ann nickel sulphide deposits. Peters and Buck (2000) subdivided the Maggie Hays nickel deposit into three (3) styles of mineralization namely: The Northern Zone – a massive sulphide zone, the Main Zone – made up massive and disseminated sulphides, and the Southern Zone – a disseminated sulphide zone. The southern zone is located several hundreds of metres

to the south of the main deposit with nickel sulphide concentration similar to the main disseminated zone (Buck et al., 1998; Peters and Buck, 2000).

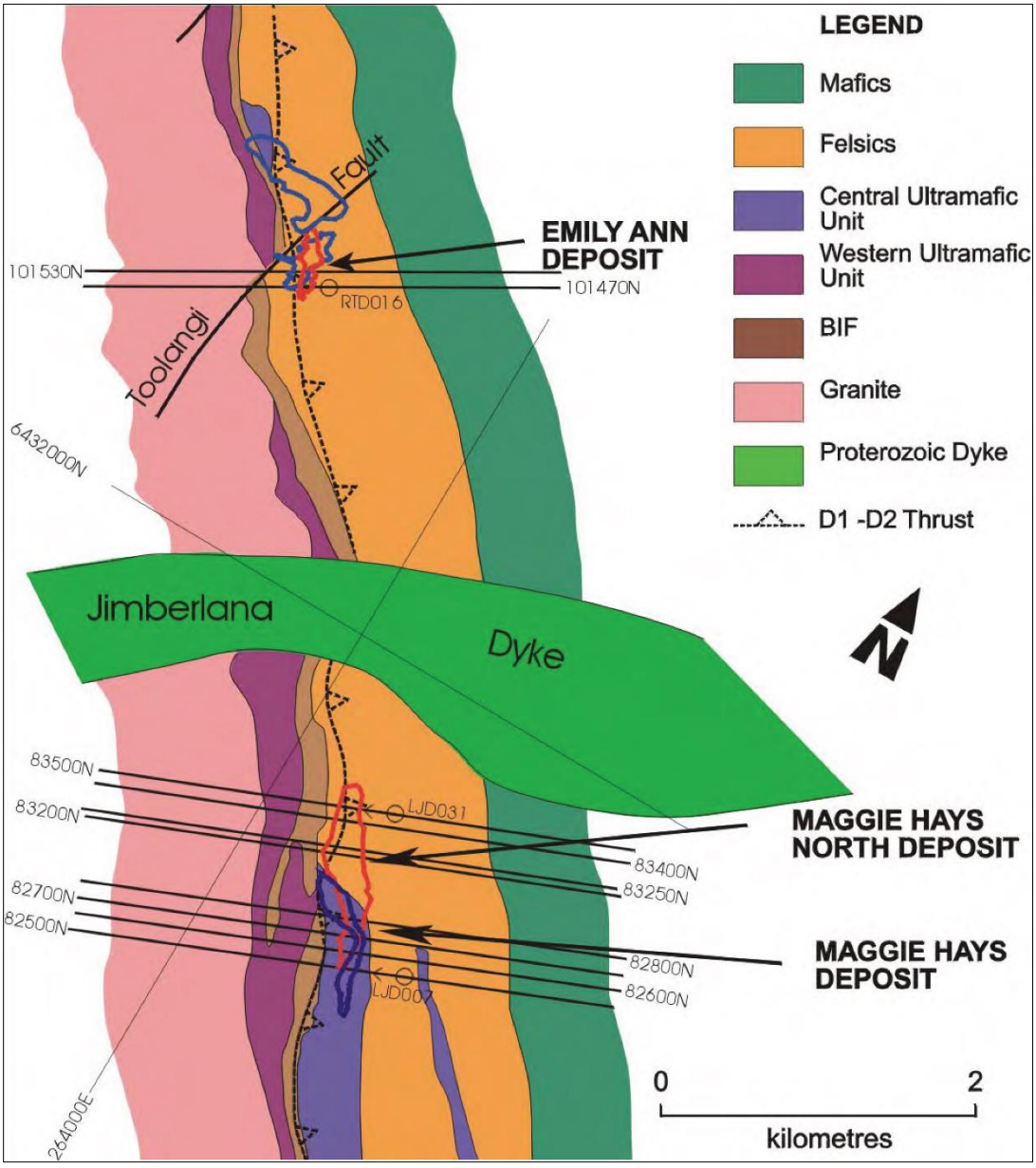

Figure 5-2: Geological setting of the Emily Ann and Maggie Hays nickel deposits. Note: The Maggie Hays deposits and the Emily Ann deposit are on different grid systems. (Geology referenced to Peters and Buck, 2000, and Williams, 2001; principally sourced from LionOre, unpubl).

5.3. CSR methodology considerations

Here, I will analyse CSR imaging capability on two different ore zones – Maggie Hays Main and Maggie Hays North nickel sulphide deposits. The two styles of

deposition are selected because, as described in subsequent sections, the strategic location of the nickel sulphide mineralized zone in each case is different, their enclosing host rock is different, they have different geometry, and they are located at different depths. Also, the ore-body geometry with respect to the boreholes is different in each case and is likely to result in different imaging challenges. With these unique differences, testing the CSR method on the two styles of deposition will evaluate its applicability at this site.

5.3.1. Maggie Hays Main ore-body delineation with CSR method

The Maggie Hays Main (MHM) is a blind, geometrically vertical ore deposit. A geologic cross section along 82700N of the MHM zone (Figure 5-2 refers) is shown in Figure 5-3. Disseminated nickel sulphide zone (beginning at a depth of about 200 m) and a massive nickel sulphide mineralization (beginning at about 350 m beneath the surface) comprise the nickel sulphide ore-body. The bulk of the deposit is located between 200 and 500 vertical metres beneath the surface and over a strike extent of 600 m.

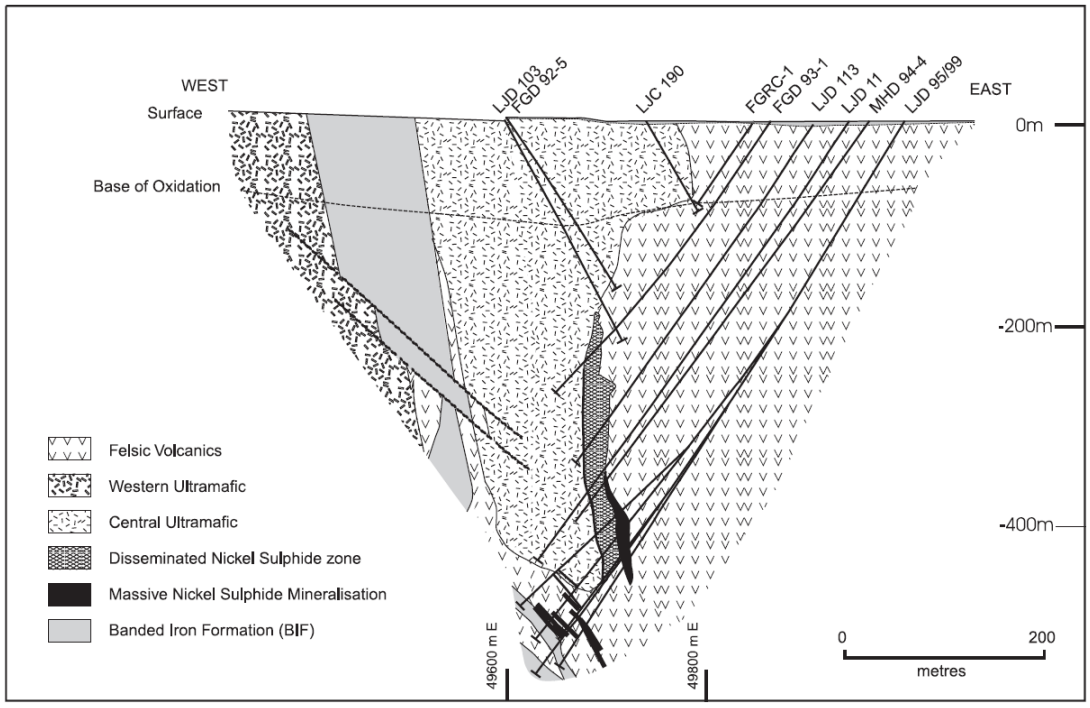

Figure 5-3: A cross section of the Maggie Hays Main zone of nickel sulphide deposit observed at 82700N (after Peters and Buck, 2000). Refer to Figure 5-2 for location.

To test the imaging capability of MHM deposit by crosshole reflection seismology, two models are created: Model 1 has both the disseminated and massive sulphides in place and Model 2 has the disseminated sulphide zone replaced by the massive sulphides.

5.3.1.1. Modelling experiment of Model 1

Model 1 is presented in Figure 5-4. The density values on core samples (obtained from the MHM deposit reported by Emerson (1995) and captured in Peters and Bulk (2000) have been assigned to the various modelled rock layers. These values are shown in Table 5-1. Where no measured density value of rock layer is available, estimated value is assigned. The accompanying velocity values are estimated average values obtained from similar rock types in the Yilgarn Craton/Kambalda nickel field of Western Australia. The modelling parameters are presented in Table 5-2. From this table it is clear that the ore impedance sits above the host rock while the massive and disseminated nickel may be difficult to separate by amplitude analysis. Two boreholes of about 100 m apart at the surface but opens to about 120 m at the point of intersecting the nickel sulphide mineralized zones, representative of two diamond-drill holes shown in Figure 5-3, are utilized as the source and receiver boreholes depicting a forward shooting crosshole borehole geometry.

Table 5-1: Velocity-density values used to parametrise model in Figure 5-4. Most of the density values are from Emerson (1995) reported by Peters and Buck (2000). Other density values and all velocity values are based on the similar rock types of Kambalda nickel field with reference to (Swager, 1997; HiSeis Pty Ltd, 2010; Urosevic et al., 2012; Greenwood, 2013; Greenwood et al., 2014).

Rock type	**Vp (ms^{-1})**	**Vs (ms^{-1})**	**ρ (kgm^{-3})**	**Acoustic impedance, ρ * Vp *10^6, ($kgm^{-2}s^{-1}$)**
Felsic volcanics	5520	3220	2690	14.85
Banded iron formation (BIF)	6100	3558	3050	18.61
Western ultramafic	6030	3524	2630	15.86
Massive nickel sulphide	4640	2688	4590	21.30
Disseminated nickel sulphide	5440	3195	3573	19.44
Central ultramafic	6350	3678	2769	17.58

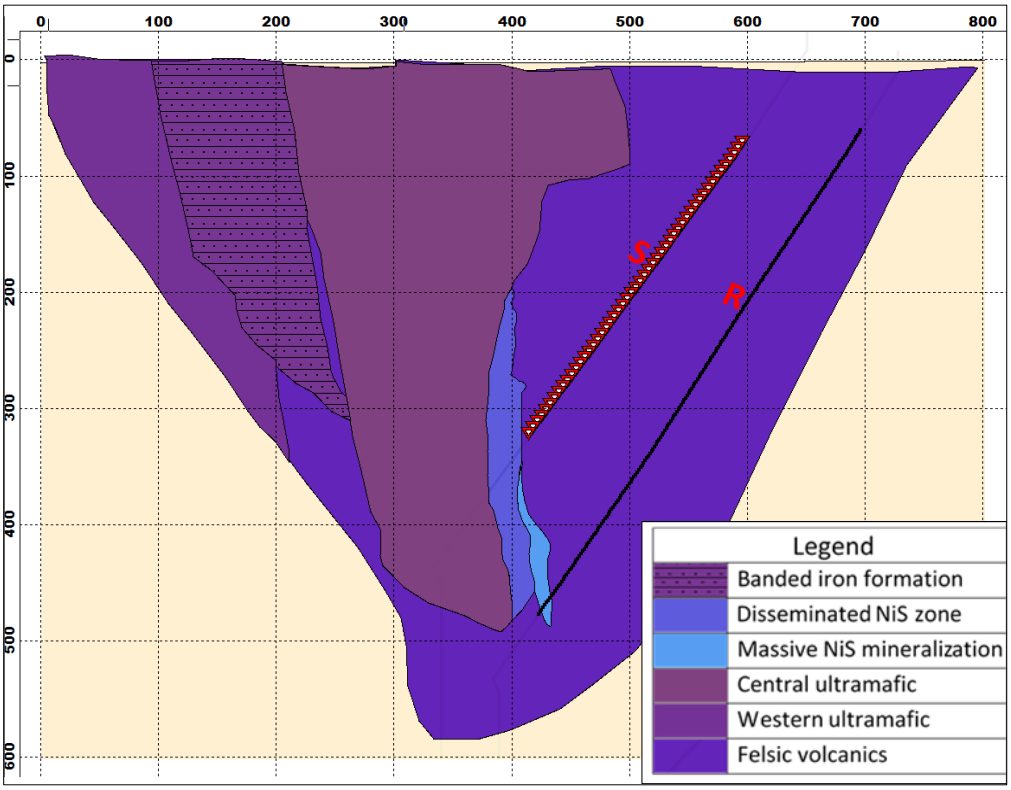

Figure 5-4: The modelled cross section of the Maggie Hays Main (MHM) nickel sulphide deposit. Two drill holes as source and receiver boreholes are labelled. The position of the source and receiver boreholes depicts the "normal" shooting approach, source borehole being selected up dip.

From below a surface depth of about 200 m where it commences, the disseminated nickel sulphide has a thickness of about 3.4 m to about 30 m at a depth near to 350 m around where the massive nickel sulphide zone begins. The thickness of the massive nickel sulphide mineralized zone, itself, varies with about less than 1 m at the depth of commencement to about 17.5 m in thickness at its central portion. A high peak frequency of 100 Hz and dense acquisition parameters are used with the view to have high frequency content, shot wavelet data for possible high-resolution imaging of targets including the thinner to medium sized portions of the massive sulphide mineralized zone.

Numerical modelling is performed with values as in Tables 5-1 and 5-2 on Model 1. The synthetic seismogram and wavefield propagation snap for shot point 29 at 90 ms are shown in Figure 5-5. Despite relatively simple geological model the recorded snap shot and the resulted time sections are quite complex. Multiple reflections

create a very complex wave picture. In Figure 5-5, down-going reflected wavefields are shown as lighter gold and darker gold broken lines coming from two main sectional contacts. All other identified wavefield types are as indicated.

Table 5-2: Modelling parameters for Maggie Hays Main synthetic data generation.

Maggie Hays Main deposit	**Parameters and values**				
	Sources	**Receivers**	**Wavelet**	**Sample rate**	**Record length**
Model 1 (massive and disseminated nickel sulphides)	51 at 5 m spacing	206 at 2 m spacing	Ricker 100 Hz	0.4 ms	250 ms
Model 2 (massive nickel sulphide replaced disseminated nickel sulphide)	✓	✓	✓	✓	✓

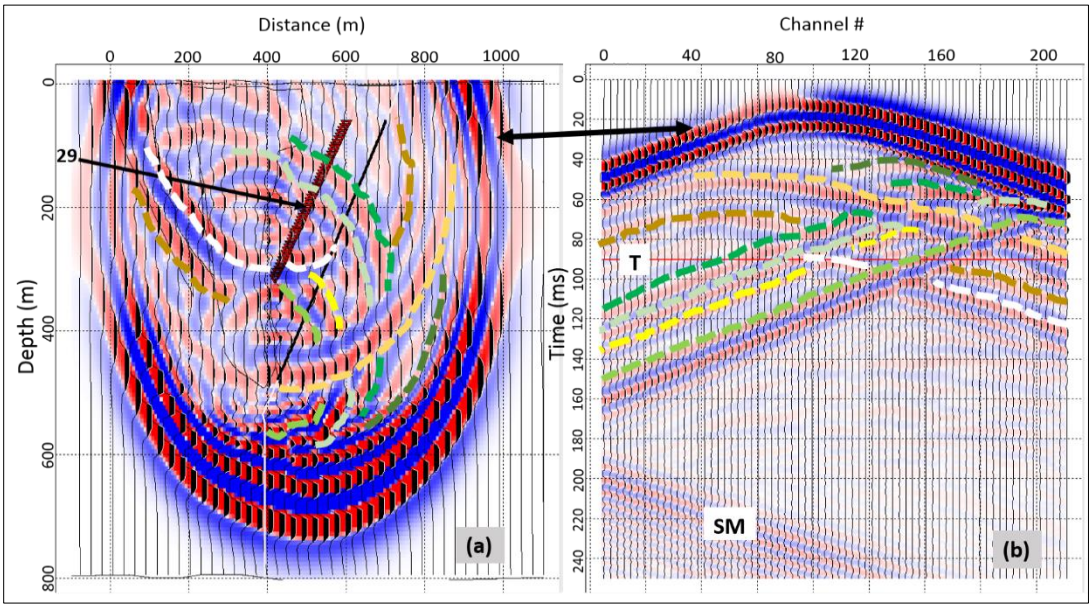

Figure 5-5: Synthetic wavefield propagation time snap (a) and synthetic seismic record (b) of Model 1 for shot point 29 at 90 ms of propagation. Black double-arrow line – outward propagating direct wave (D_S). For the broken lines: lighter gold – down-going reflection of D_S from the jutted CUU-FV contact (around 100 m depth), darker gold – down-going surface reflection from CUU-FV contact (near the surface) caused by D_S, darker green – reflection from most upper part of the disseminated NiS (DNiS), bright green and lighter green – reflections from near upper parts of DNiS, yellow – reflection likely coming from near central part of the DNiS, light green– overlapped reflections from thin upper part of the massive NiS mineralization (MNiSM) and lower part of DNiS, white – surface reflected down-going wave. SM – some down-going multiples and T – time-step line.

5.3.1 Synthetic data processing and imaging for Model 1

The synthetic raw data are displayed in Figure 5-6. Down-going part of the direct wave, D_S, has a detrimental effect on the near bottom traces. To avoid degradation of this reflected wave, the direct wave is muted instead of removing it by 2D-spatial filtering. The CUU-FV contact down-going reflections, D_{CF1} and D_{CF2}, and other coherent and unwanted wavefields are removed by the application of the F-K reject polygon and the 2D-median filters. A 10-45-170-280 Hz Ormsby band-pass filter was applied thereafter. Figure 5-7 shows the wavefield separated seismograms.

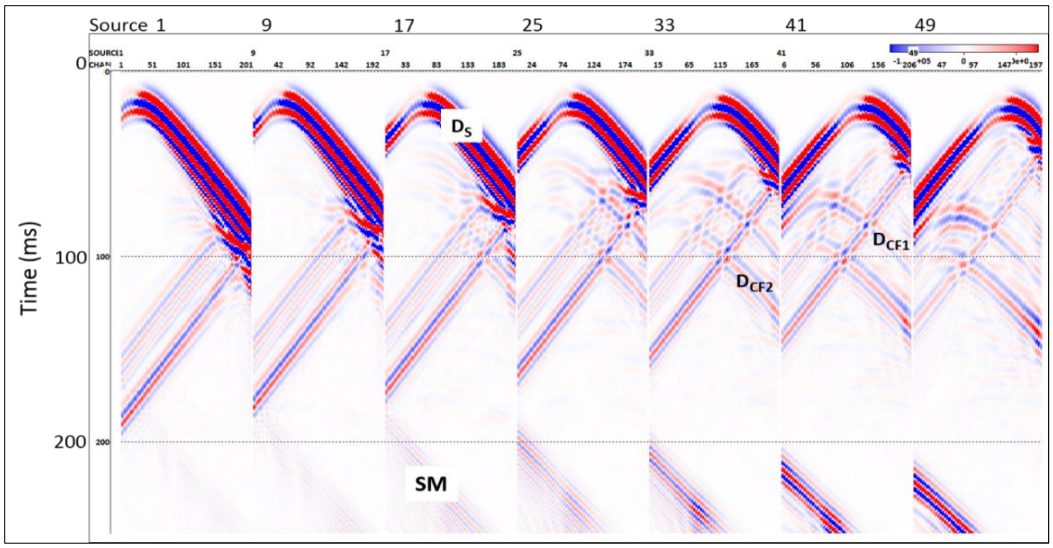

Figure 5-6: The raw synthetic seismograms for MHM Model 1 shown for every 8th shot. D_S – spherically propagating direct wave, SM – some down-going multiples, and D_{CF1} and D_{CF2} – down-going surface reflections emanating from two main different contact sections of CUU-FV caused by the up-going part of D_S.

After extensive tests with 90° preferential slope, migration aperture of 8° resulted in the closest match to the model. The migration used a constant velocity of 5520 ms^{-1}, a representative velocity of the felsic volcanics. The migration space was 500 m wide and 600 m in depth. All the shot points and receivers located above (at the right side of) the target were used in the migration image creation. The resulting migrated image with the geologic section overlain is presented in Figure 5-8. The part of the nickel sulphide ore deposit imaged is largely displaced to the left of the target. However, the uneconomic reflectors interfaces such as the BIF-western ultramafic correspond favourably with the associated geologic section. From the figure, the depth of the ore-body recovered is about 400 m from the surface.

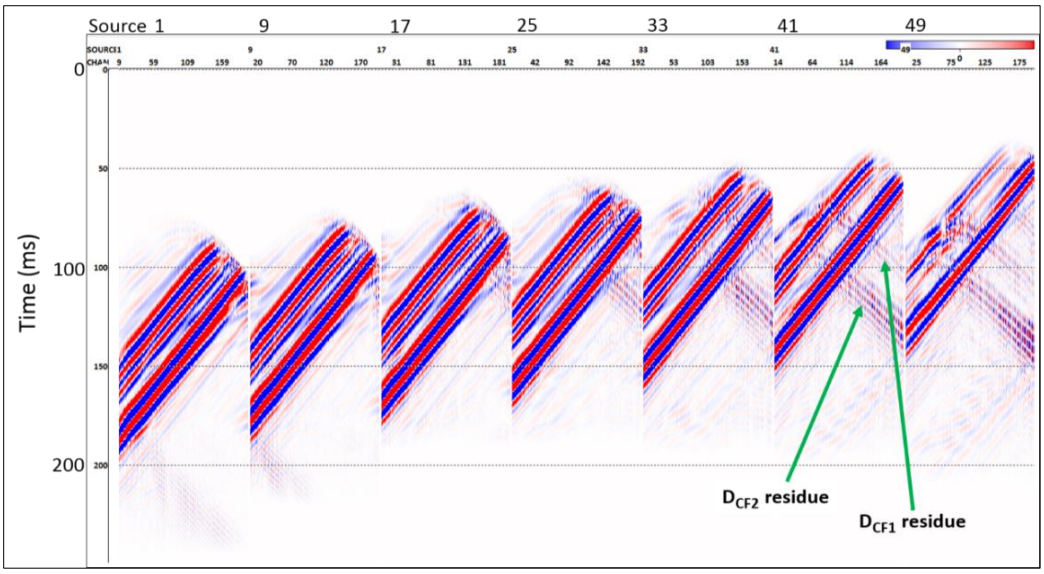

Figure 5-7: Resulting seismograms after wavefield separation processing. Diffracted and remnants of surface reflected up- and down-going wavefields including D_{CF1} and D_{CF2} residues are present.

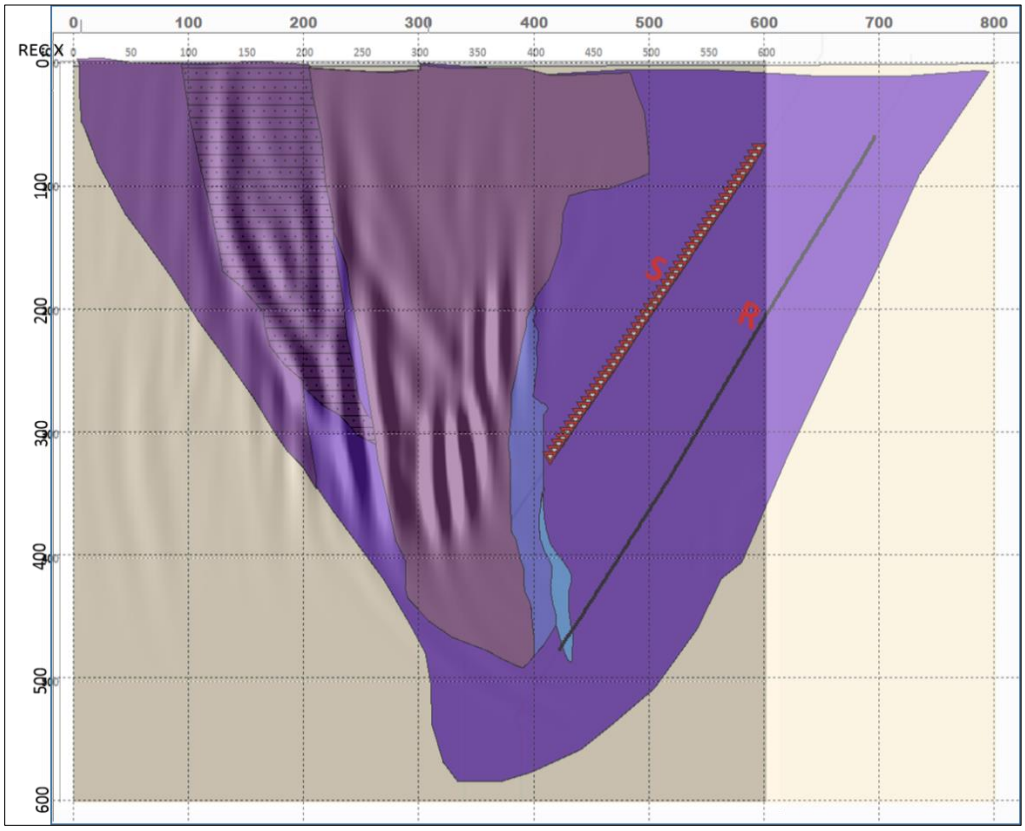

Figure 5-8: Migrated image obtained for Model 1(disseminated and massive nickel sulphide zones in place, as shown in Figure 5-4). A migration aperture of 8° and 90° preferential slope were used for the migration image generation. The migrated image space is 0 to 600 m and to a depth of 600 m. The migrated image of the nickel sulphide (NiS) mineralized zone is largely displaced left-ward to the target but other rock contacts matched quite well the geologic section.

5.3.1.2. Synthetic data processing and imaging for Model 2

This model is built with the purpose to examine if any amplitude differences can be detected related to different ore concentrations. Thus, Model 2 has everything like Model 1 of Figure 5-4, except that the disseminated nickel sulphide zone in Model 1 is replaced entirely by the massive nickel sulphide mineralization. Model 2 data was generated and processed same way as for Model 1. Still the ore zone is poorly imaged. Resultant PSDM images of the two models are shown in Figure 5-9. Generated with same wavelet and central frequency, both images are of same resolution. Both migrated images relatively poorly resemble geology. In each case the dip of the ore-body imaged is preserved but the migrated images are erroneously displaced far to the left of the corresponding geology. Interestingly, there is a good correlation of the uneconomic rock interfaces with the migrated section. Relatively, high reflection coefficient exists between these various rock contacts, as shown on Table 5-3, giving rise to strong reflections at these interfaces. There is a subtle amplitude difference for different ore concentrations, but the miss-positioning of the image is too great to assign real value to the amplitude differences. As conducted in this study, clearly this geological model presents a challenge for crosshole imaging.

An alternative approach to this type of crosshole which may be envisaged coming to the exploration practice sometimes in the near future is to utilize Full Waveform Inversion (FWI) of crosshole data followed by depth imaging. Recent FWI tests involving soft-rock borehole seismic data (VSP) have shown some promise (Urosevic et al., 2018). Interferometric crosshole imaging might be another approach.

Table 5-3: Reflection coefficients for Maggie Hays Main various rock interfaces

Rock contact	**Reflection coefficient (R)**
Felsic/central ultramafic	0.08
Felsic/disseminated nickel sulphide	0.09
Felsic/massive nickel sulphide	0.18
Massive/disseminated nickel sulphides	-0,05
Central ultramafic/banded iron formation	0.03
Felsic volcanics/banded iron formation	0.11
Banded iron formation/western ultramafic	-0.08

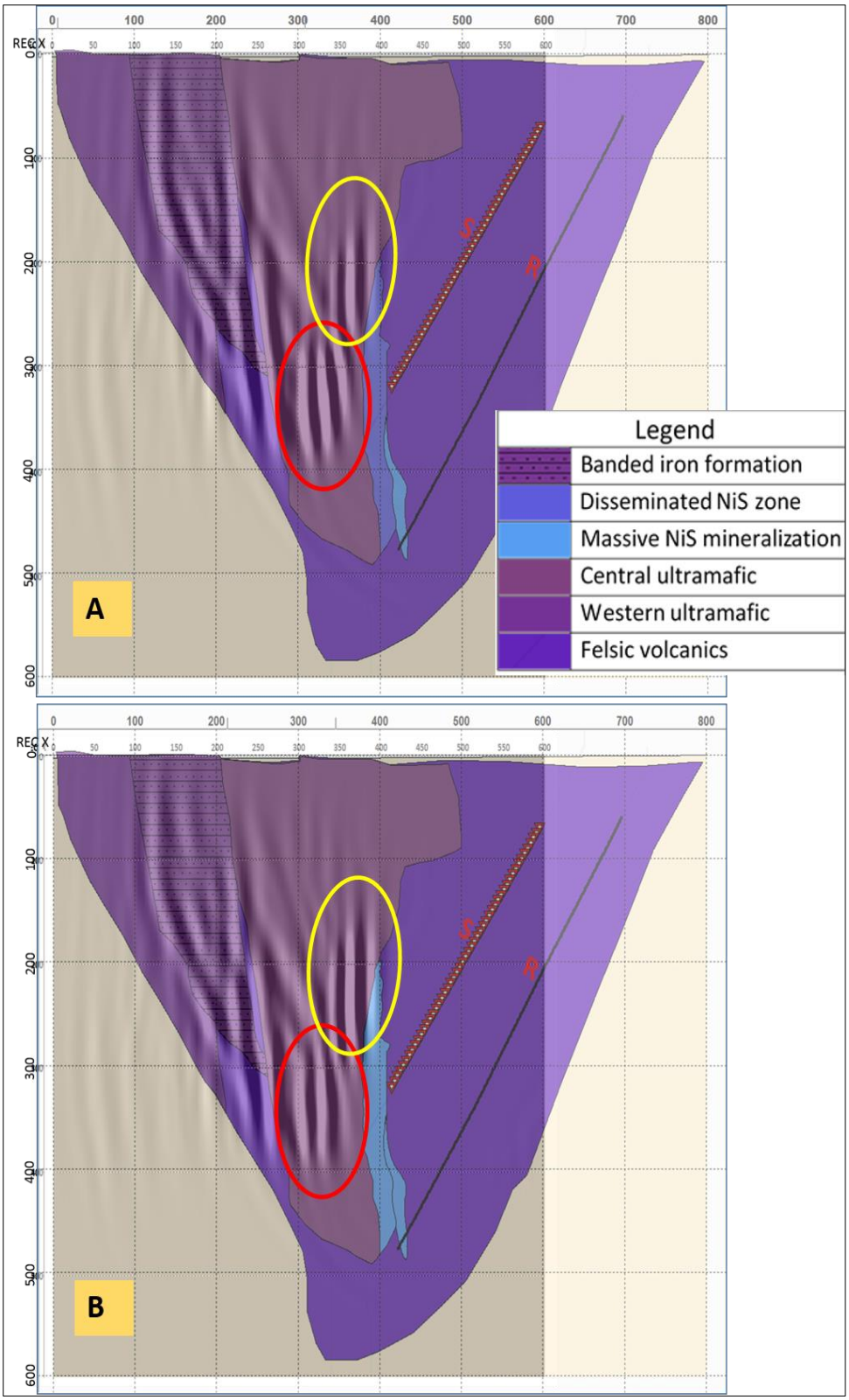

Figure 5-9: Migrated sections with the overlain geologic sections of Maggie Hays Main. Panel A: Model 1 (ore zone is disseminated and massive NiS). Panel B: Model 2 (ore zone is all massive NiS). Some differences in reflection amplitudes exist but these differences are very subtle; example, as observed within the yellow ellipses.

5.4. Maggie Hays North nickel ore-body mineralization style

This zone is hosted entirely within Felsic Volcanic Unit (FVU) with the mineralization controlled by an early thrust fault. Mainly massive, stringer, and breccia sulphides, the deposit with a near vertical geometry dips at about 50° to the east, has a strike length of 800 m, and it is blind with the top commencing at about 100 m beneath the surface. An average regolith depth of about 50 m is associated with the deposit. A highly conductive barren sulphide hosted BIF unit lies in close proximity to the west of the deposit (Peters and Buck, 2000; Williams, 2001). Figure 5-10 is a cross section of the Maggie Hays North nickel sulphide deposit observed at 83200N (refer to Figure 5-2).

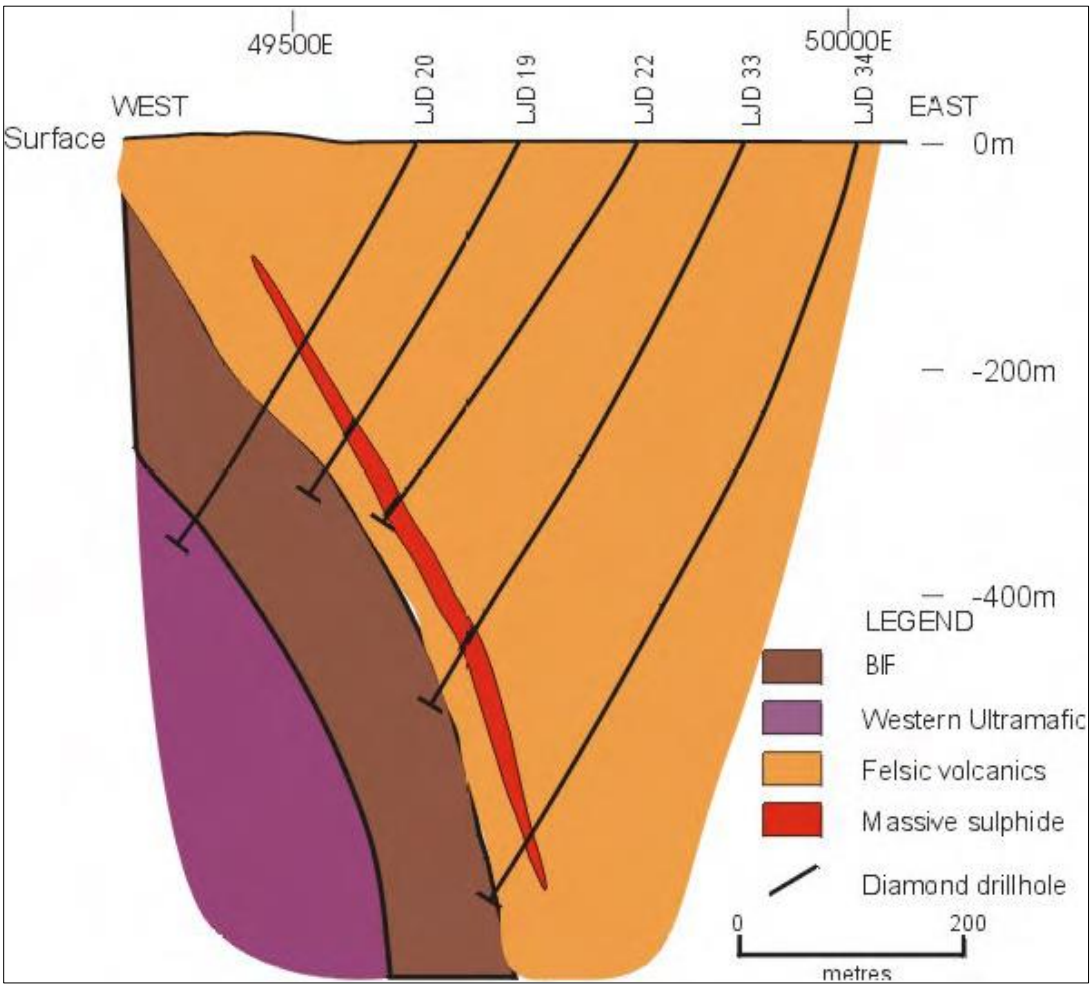

Figure 5-10: A cross section of the Maggie Hays North nickel sulphide deposit observed at 83200N (after Williams, 2001). Refer to Figure 5-2 for location.

5.4.1. Maggie Hays North ore-body delineation using different CSR source-receiver borehole geometries

The massive sulphide deposit is characterised by a series of angular boreholes (Figure 5-10). This provides possibility for testing different combination of boreholes and to observe their effect on image quality produced. Four different boreholes scenarios are considered. The first case and second case involve so-called forward shooting geometry and borehole separation typical of surface grid drilling patterns of 100 m and 200 m, respectively. In these two cases, the receiver borehole remains same but the source borehole is moved from 100 m to 200 m in the up-dip direction. In the third case the reverse CSR shooting borehole geometry is examined for borehole separation of 100 m. Finally, the fourth case considers 100 m separated boreholes, but located far down-slope of the target.

5.4.1.1. Cases 1 and 2: Forward shooting crosshole borehole geometry with 100 m (Case 1) and 200 m (Case 2) inter-borehole separation

The geologic model covering Cases 1 and 2 is depicted in Figure 5-11. No petro-physical measurements were available from the study. Consequently, the density and velocity values of Table 5-1 have been used to parametrise the model. Recording geometry is provided in Table 5-4.

Table 5-4: Maggie Hays North (MHN) modelling parameters for the synthetic data generation.

Type of Geometry	Parameters and values				
	Sources	**Receivers**	**Wavelet**	**Sample rate**	**Record length**
Normal, 100 m inter-borehole interval	52 at 10 m spacing	138 at 5 m spacing	Ricker 80 Hz	0.4 ms	260 ms
Normal, about 200 m inter-borehole interval	41 at 10 m spacing	✓	✓	✓	✓
Reverse, 100 m inter-borehole interval	138 at 5 m spacing	52 at 10 m spacing	✓	✓	✓
Normal, 100 m inter-borehole (for far down-slope located boreholes)	68 at 10 m spacing	173 at 5 m spacing	✓	✓	270 ms

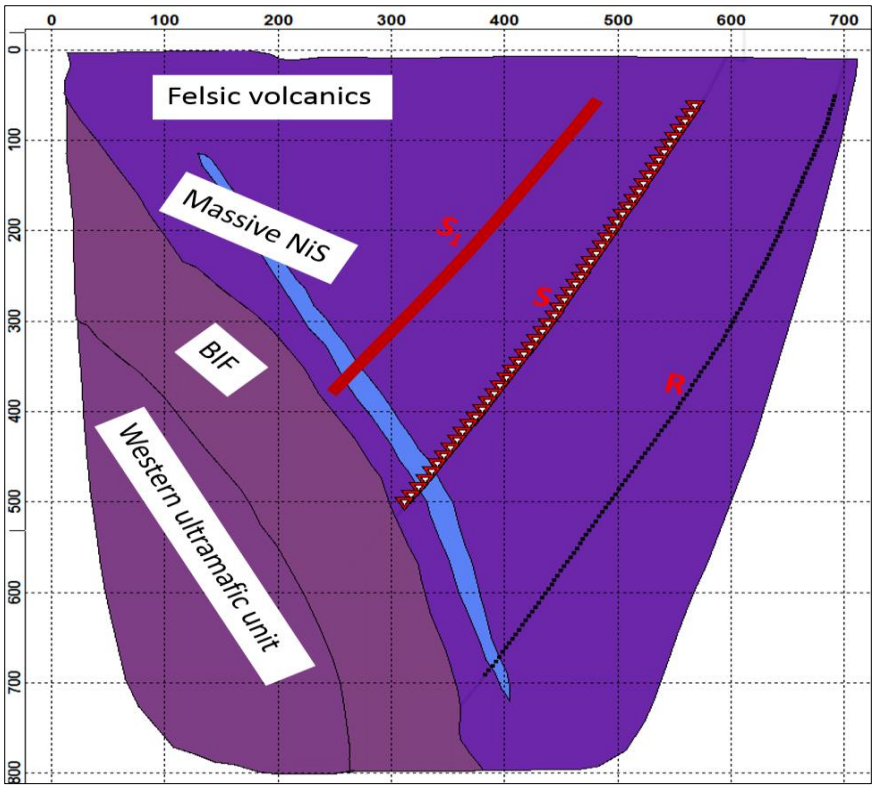

Figure 5-11: The modelled cross section of the Maggie Hays North (MHN) nickel sulphide deposit as shown in Figure 5-10 showing the source-receiver geometries of Case 1 and Case 2. The position of the source and receiver boreholes assumes normal approach shooting crosshole geometry.

Data processing and wavefield separation assumed the same flow as in previous studies. The preserved amplitude wavefield is then used for CSR Kirchhoff migration to depth images. The migration used a constant velocity of 5520 ms^{-1} representative of the felsic volcanic host rock. The migration space was 500 m wide and 800 m in depth. Migration imaging was tested with the migration dip of 45° and varying migration apertures. Figure 5-12 shows two examples of migrated images overlain onto the geologic model, obtained with 1° and 5° migration apertures and preferential dip of 45°. Images are distributed over very short distance. Further testing revealed that the migration aperture of 7° and a focussing slope of 58° produced the image that closely matched geology (Figure 5-13). Significant segment of the reflector is imaged as denoted by red arrows in Figure 5-13. The distance from the source borehole to the point where the red line bisects the nickel sulphide deposit (the target) indicates how much of the inter-borehole interval is recovered. In the figure, apart from the nickel sulphide ore-body imaged, the boundaries of other rock layers have as well been mapped.

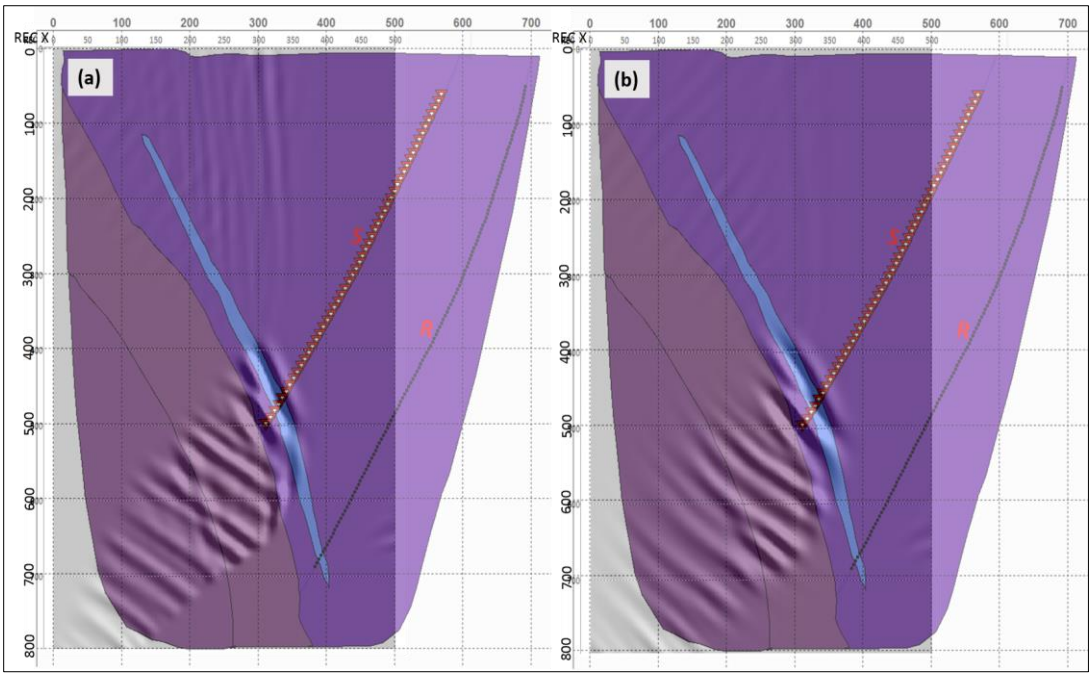

Figure 5-12: Migrated images with the overlain geologic sections obtained using image focusing dip of 45° and migration aperture of (a) 1° and (b) 5°.

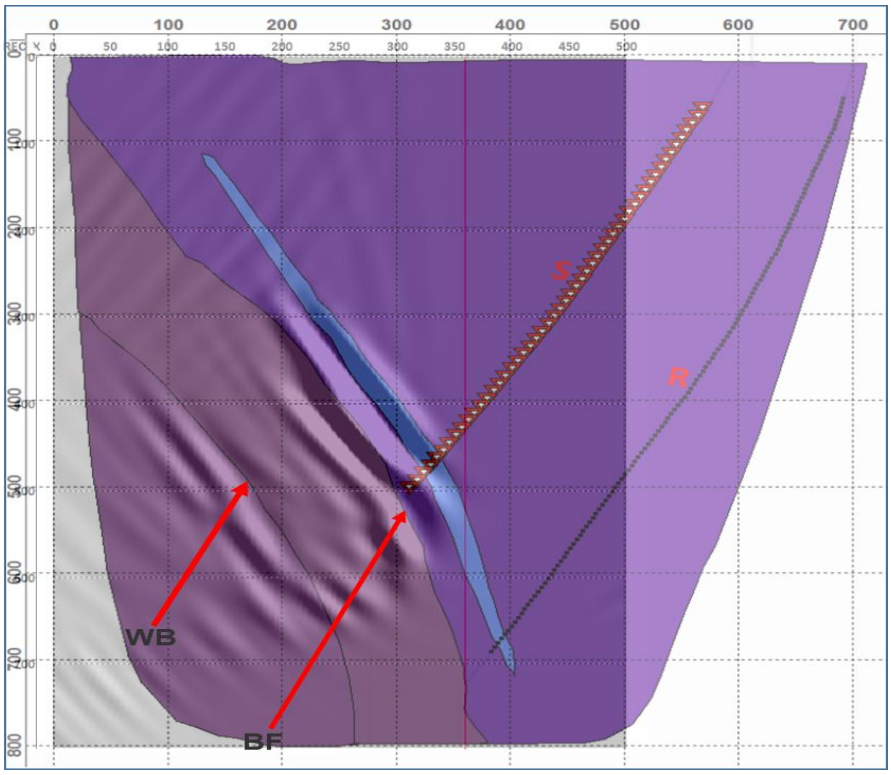

Figure 5-13: Migrated image using migration aperture of 7° and 58° preferential slope. The image is 500 m wide and to a depth of 800 m. The distance between source borehole intersection of target and the red line indicates the approximate target's surface area recovered between the boreholes in this geometry. BF indicates the BIF-Felsic volcanics (BIF-FV) rock units contact and WB indicates the contact of the Western ultramafic-BIF (WU-BIF) rock units.

Once imaging parameters were set, I compare images computed for Case 1 and Case 2. This is shown in Figure 5-14. Both cases imaged the target up-dip from the borehole locations. The first initial black (positive peak) of the recovered image correlates well to the felsic volcanics and the ore-body upper boundary while the second positive peak correlates to their lower boundary. This can all be related back to the acoustic impedance contrasts at each boundary (Table 5-1).

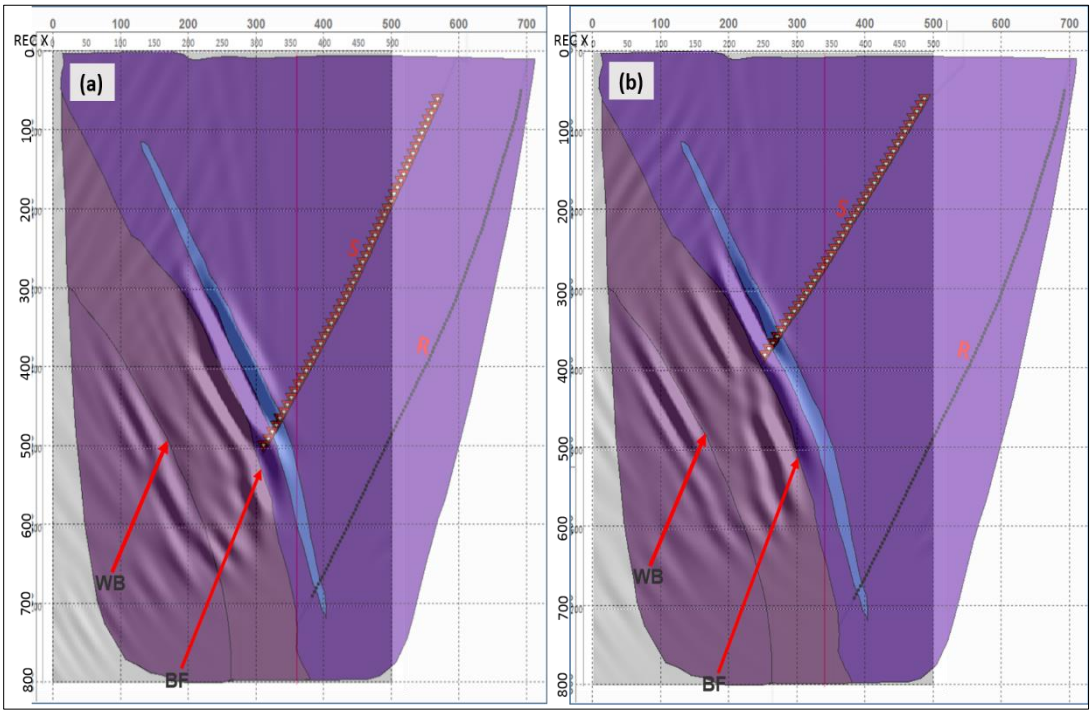

Figure 5-14: Comparison of the migrated sections with the overlain geologic sections. (a) Case 1 using 100 m, and (b) Case 2, 200 m inter-borehole spacing. The distance of the red line from the source borehole indicates the amount of partial recovery inter-borehole imaged for each case.

In Case 1, the up-dip part of the ore-body is imaged from about 190 m to 365 m covering a lateral extent of 175 m and depth of about 542 m. In comparison, the PSDM image of Case 2 has mapped the ore-body from about 170 m to 340 m covering a lateral extent of 170 m and to a depth of about 521 m. Partial imaging occurred between the boreholes in the two borehole geometries but larger for Case 2 than Case 1. The explanation to this is that, an increase in borehole separation allowed greater inter-borehole reflection angles (along the slanting part of the ore-body) and results in greater inter-borehole imaging. A weakening amplitude reflection exists in Case 2 than in Case 1. Case 2 geometry also tends to record more

reflections in the up-dip direction but Case 1 more reflections down-dip hence more down-dip recovery of the ore-body (542 m of Case against 521 m of Case 2).

The proximity of the ore-body and BIF rock layers produce reverberations with constructive and destructive interference distorting and misplacing the individual reflectors. A higher frequency is required to resolve the layers and place the reflections in the correct position. Also, on both migrated sections the reflection from the BIF and Western Ultramafic unit contact is presented but poorly imaged.

5.4.1.2. Case 3: Reciprocity geometry of Case 1

Using the model values in Table 5-1 and modelling parameters in Table 5-4, acoustic full-waveform modelling is performed for the Case 3 model. Note that for Case 1, the forward shooting geometry results in a longer receiver array for recording. Also, the location of the receiver borehole in Case 1 relative to the dipping ore-body enables reflections to be recorded by the bottom receivers. The reciprocal geometry (Case 3) makes up-dip slope target reflected waves travel relatively shorter distance to get recorded. Imaging results for Cases 1 and 3 are compared in Figure 5-15.

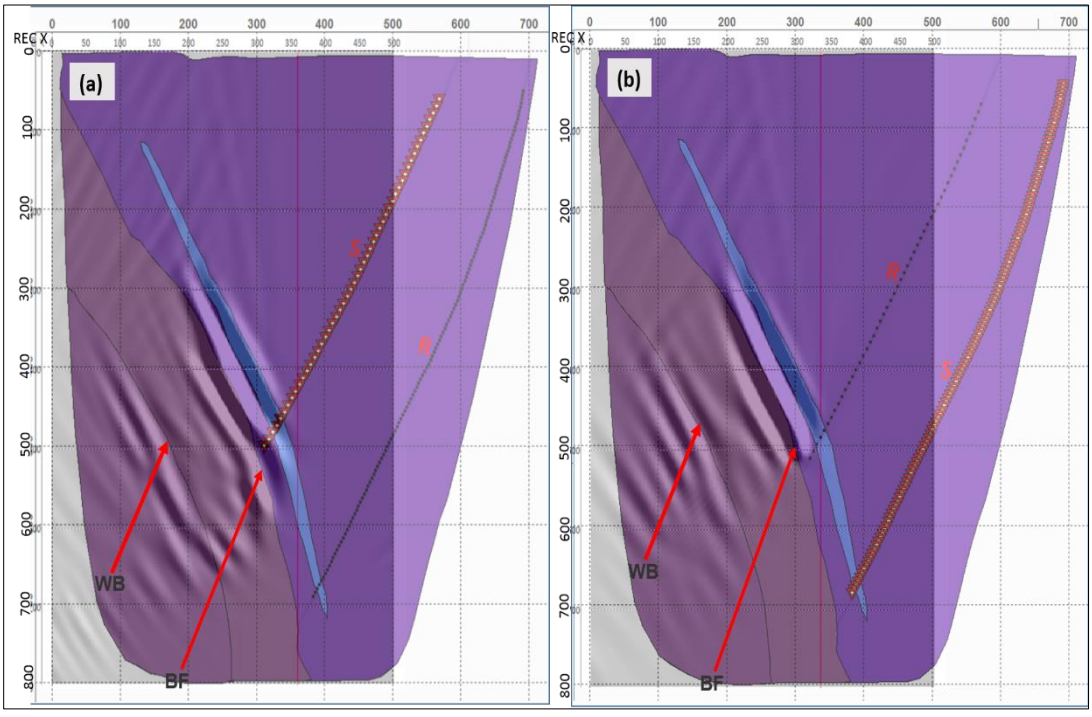

Figure 5-15: Comparison of the migrated sections with the overlain geologic sections. (a) Case 1 (100 m inter-borehole for a forward shooting crosshole geometry) and (b) Case 3 (reverse shooting crosshole geometry; a reciprocal geometry of Case 1).

The lateral target surface area and depth recovery is larger in Case 1 than in Case 3 (the reciprocity geometry), being 175 m and 542 m for target surface area and depth recovery respectively for Case 1 while for Case 3 they are only 130 m and 511 m respectively. Case 3 also produces equally good image in the up-dip direction as Case 1 but worse in the down-dip direction. There is weakening amplitude reflection in the up-dip direction in Case 3. Both geometries provide good quality depth images but over a shorter length. While long shot aperture facilitates larger target surface area recovery, longer receiver array length is perhaps even more required for CSR data quality and target surface area recovery, as observed also in Chapter 4.

5.4.1.3. Imaging the Maggie Hays North ore-body utilizing arbitrary far down-slope located receiver borehole

The final test involved a pair of boreholes shifted in the down-dip direction of the ore-body as presented in Figure 5-16. The source-receiver boreholes are separated 100 m in a forward crosshole shooting arrangement. The same processing parameters

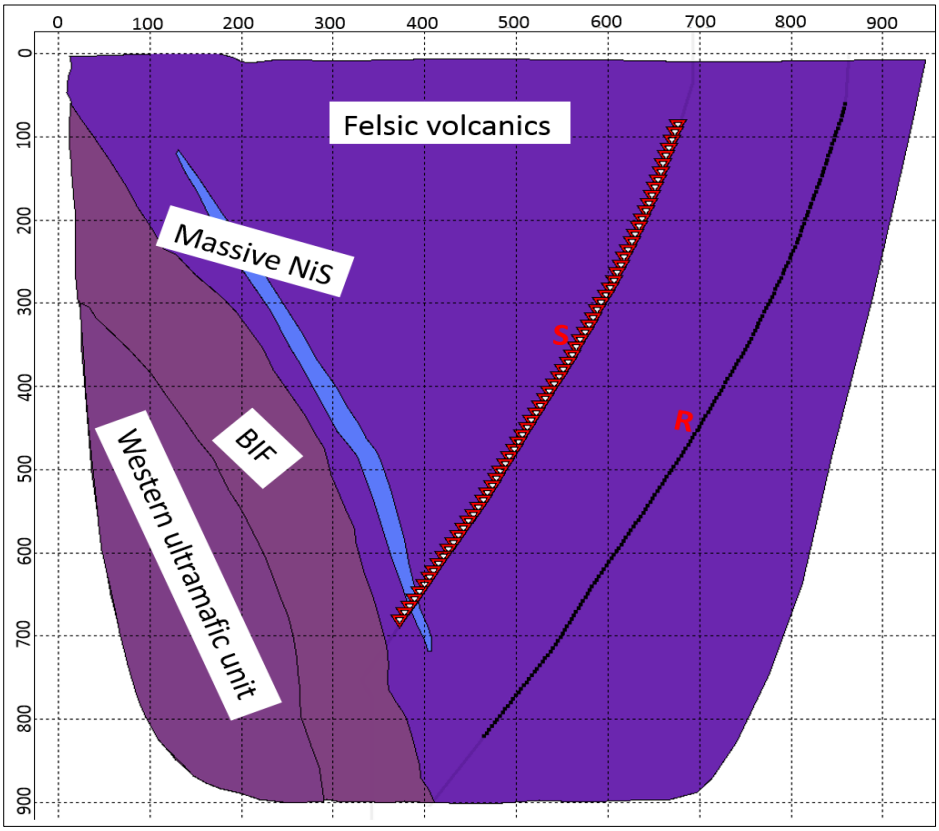

Figure 5-16: MHN geologic model (Case 4). The receiver borehole is arbitrary located far down-slope the ore-body, about 100 m down-slope from the source borehole.

and migration velocity were used as for Cases 1-3. However, to optimize the image quality, the migration aperture is increased to 10° and a focussing dip of 61°. The PSDM image obtained is provided in Figure 5-17. The resultant image has lateral extent increased to 600 m instead of 500 m and imaged down to 900 m instead of 800 m in the previous cases. The image resulted in the closest match to the geology. A substantial surface area including the entire down-dip part of the ore-body has been delineated. The boundaries of other rock layers have also been clearly mapped.

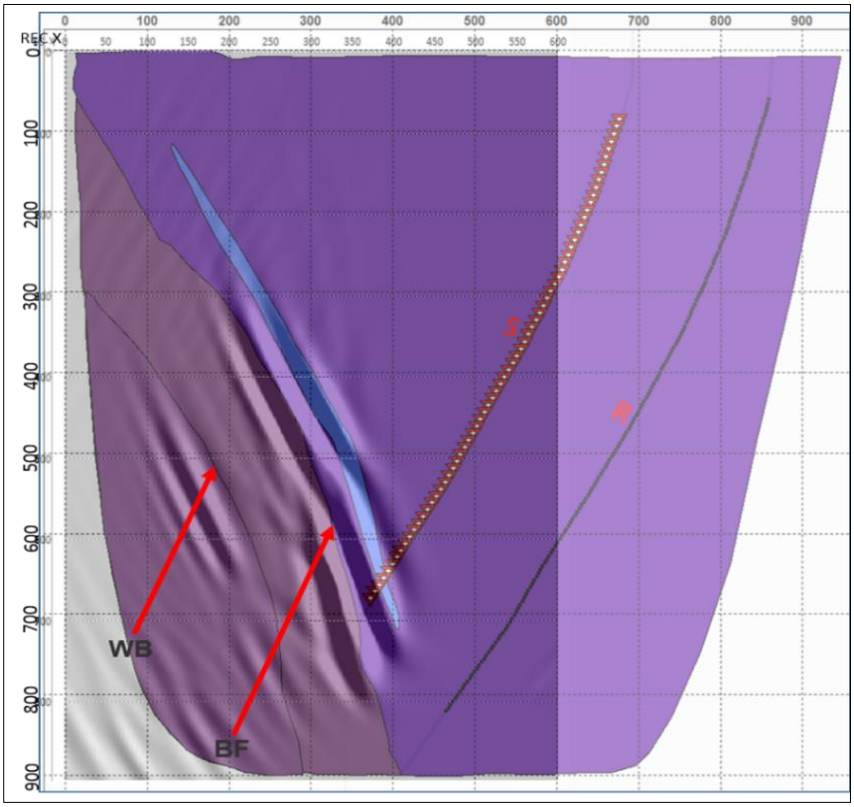

Figure 5-17: Migrated image using aperture of 10° and 61° preferential slope. The image is 600 m wide and to a depth of 900 m. A substantial surface area including the entire down-slope part of the ore-body is imaged.

5.5. Summary

Synthetic tests were performed to examine CSR applicability in imaging Maggie Hays style nickel sulphide ore deposits. With the Maggie Hays Main (MHM) deposit, two scenarios of nickel sulphide mineralized zones were considered. Model 1 considered the presence of both the disseminated and massive nickel sulphides as is the real deposition model. Model 2 considered the situation where the

disseminated nickel sulphide zone is entirely replaced by the massive nickel sulphides but made use of same data generating parameters in Model 1. Model 2 was built with the purpose to examine if any amplitude differences can be detected related to different ore concentrations. Results were presented in Figure 5-9. It was observed that amplitude reflections differences are very subtle. As such, it will be difficult to target massive sulphides in MHM hard rock type environment with CSR approach base only on amplitude reflections attributes. Practically, additional geophysical and geological information are needed for better interpretation of such results. Also, in the real field case we would require good knowledge of the rock properties and precise velocity field for imaging. In both models, the migrated section superimposed with the geologic section indicated that the dip of the nickel sulphide ore-body imaged is preserved but the image is displaced largely to the left of the corresponding geologic section. This positioning error of the image may possibly result from the smoothing the velocity field of migration. Interestingly, however, other uneconomic rock contacts imaged mapped quite well the geologic section.

One other way to likely improve crosshole imaging of such a geology is to utilize Full Waveform Inversion (FWI) of crosshole data followed by depth imaging. Utilization of FWI is envisaged to come into the hard rock exploration practice sometimes in the near future. FWI will provide much higher resolution velocity model that can be used for improved depth imaging and stratigraphic interpretation. The reason for testing FWI is that one anticipates a crosshole environment to have much more accurate starting model and much higher SNR, both of which are prerequisite for successful FWI (particularly high frequency inversion).

Delineating the MHN ore deposits with the CSR geometry, forward and reverse shooting crosshole borehole geometries and different borehole separations for the forward crosshole shooting geometry show slightly different results in the various cases (Cases 1-3) considered. Results of different inter-borehole spacing (Cases 1 and 2) were presented in Figure 5-14, and those of reciprocity geometries (Cases 1 and 3) were presented in Figure 5-15. Migrated images produced with each of the three geometries provided appreciably well the up-dip part of the target nickel sulphide surface area. Also, the images obtained in all the cases correlated quite well

with the geologic section. However, only the forward shooting borehole geometries provided inter-borehole partial imaging of this type of ore deposit. For these borehole geometries and geology, each geometry imaged different part of the structure. Case 2 imaged much more up-dip part than the down-dip part (from 170 m to 340 m covering a lateral extent of 170 m) whereas Case 1 imaged much more down-dip part than the up-dip part (from 190 m to 365 m covering a lateral extent of 175 m). Thus, though target lateral extent recovery is quite the same in both geometries Case 1 provided greater depth recovery of 542 m than the 521 m depth recovery provided in Case 2. Also from the results, Case 1 provided a nicer imaging than Case 2. For the reciprocity geometries, even-though Case 3 mapped very well the geologic section, it produced less target depth recovery of 511 m against 542 m of Case 1. It can be concluded that reciprocity geometries of angular boreholes for steeply dipping targets will not produce the same target depth image recovery. For real survey, all these factors need to be considered but where target depth recovery is paramount, then Case 1 geometry may be more advantageous. Case 4 for MHN ore-body delineation utilized similar pair of boreholes and same separation and shooting geometry as in Case 1 but the boreholes shifted in the down-dip direction of the ore-body. PSDM migrated image of Case 4 is presented in Figure 5-17. A substantial surface area including the entire down-dip part of the ore-body has been delineated.

Other migrated features that do not correspond to real structures may arise when these individual reflectors are not well resolved. The proximity of the ore-body and BIF rock layers creates reverberation with constructive and destructive interference distorting and misplacing the individual reflectors. A higher frequency is required to resolve the layers and place the reflections in their correct positions. The presence of artefacts may be due to multiple factors such as insufficient wavefield separation, late time events, and migration related issues.

In all then, CSR modelling results of MHM (in particular) and MHN type nickel sulphide ore deposits show that while the dips of vertical ore-bodies are preserved, their locations are misplaced. Also, modelling results, in particular for MHN type nickel sulphide ore deposit, demonstrate that depth recovery of steeply dipping structures will require boreholes location at far down-slope part of the target.

6. Crosshole synthetic study of Rosebery-type volcanogenic massive sulphide ore lenses

6.1. Introduction

Rosebery volcanogenic massive sulphide (VMS) ore deposit is a major sheet-style polymetallic Zn-Pb-Cu-Au-Ag massive sulphide distributed in composite lenses (Green et al., 1981; Green, 1983; Large et al., 2001). Because of its nature, the future of the Rosebery mining operation depends on the continual discovery of new lenses to maintain the required feed to the mill (Large et al., 2001). This in turn, depends on the continual development and upgrading of in-mine exploration techniques, including geophysics, to enable the required discovery rate to be maintained. But largely, Rosebery VMS deposit has peculiar geological deposition and environmental characteristics. A large section of the deposit is buried under marine origin electrically conductive black slates with varying thickness and the ore lenses are hosted within tuffaceous shale (this is elaborated more under the summary section of Rosebery geology). In addition, sub-vertical and steeply dipping structures commonly associate with the target (Green et al., 1981; Green, 1983; Solomon et al., 1987; Large et al., 2001). These factors pose a challenge to the more familiar methods of geophysical exploration. Furthermore, the area, in general, has varying topographical mountainous terrain and a thick cover of vegetation (Evans, 2009), (see Figure 6-1), which restricts access to the area. Restricted access to the area coupled with the steeply dipping nature of the VMS ore bearing structures restrict the application of the conventional surface seismic reflection technique. To image deep seated vertical or sub-vertical structures by walk-away VSP, whether by the conventional or the reversed VSP approach, the source or the receiver positions on the surface need to cover considerable offsets in proportion to the depth of the target. This will be a difficult feat for VSP application in such environment. Also, in VSP application, there will be some amount of energy scattering once either the source or receiver is placed on the surface.

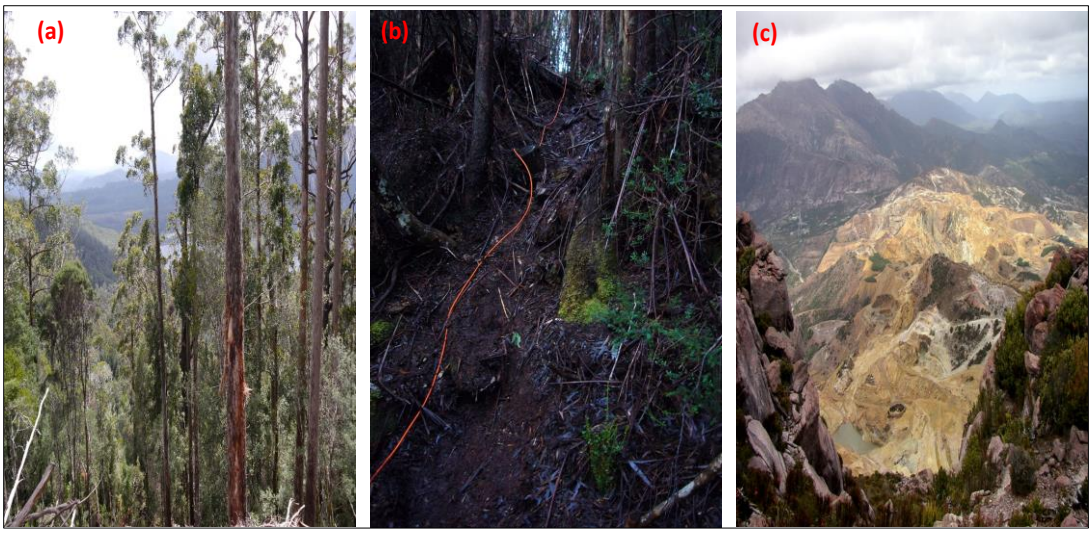

Figure 6-1: Environmental challenges at Rosebery. (a) and (b) dense vegetation (courtesy of HiSeis Pty Ltd, (pers. commun.)), (c) difficult terrain (with reference to Seymour et al., 2007, Mineral Resources Tasmania).

Kinkela et al. (2014) performed a trial surface seismic reflection at Rosebery in attempt to image, at depth, the controlling structures of mineralization and the known ore-bodies so as to validate the surface seismic technique in the area. And then to prospect down-dip for further mineralization. A lot of challenges were encountered from the survey design stage to the actual survey and beyond. The design process was extremely difficult due to dipping structures and large topographical variation on mountainous terrain (about 400 m variation). Because of the extreme topography and vegetation, the area was only accessible by foot. Restriction to vehicle access led to the choice of explosive energy source. Even then, variability of the near-surface cover resulted in a change of buried source coupling from excellent, when coupled to fresh rock, to very poor when the fresh rock was deeper. All these factors, and the consequent data processing challenges, made the Rosebery surface seismic survey extremely difficult and expensive in terms of time and cost.

The application of the CSR technique as an additional geophysical method to detect and delineate (new) ore lenses within the mine environment is a driving factor for this research. The method could as well be employed to re-evaluate exhausted areas within the mine environment for low-volume high-grade VMS ore lenses missed by drilling and potential field methods. Thus, this synthetic work seeks to test the capability of the CSR method to detect and delineate relatively medium sized,

dipping VMS ore lens in environment where other geophysical methods and techniques may lack the ability to provide adequate information. The method will then be extended to image a theoretically unknown VMS ore deposit and then test the capability of the method to image cluster of VMS ore lenses.

6.2. Geologic setting of Rosebery VMS deposit

A detailed description of the geology of Rosebery deposit has been well documented and only a summary of some of the research is presented here.

Rosebery ore deposit is one of five major VMS deposits within the Central Volcanic Complex, of the 250-km long Mount Read Volcanic belt, on the west coast of Tasmania, Australia. The Mount Read Volcanic belt is late Cambrian in age (Bradley, 1956; Corbett et al., 1974; Corbett, 1981; Green et al., 1981; Large et al., 2001) and occurring within it are a number of major economic and numerous sub-economic volcanic-hosted deposits (Loftus-Hills, 1915; Hall and Solomon, 1962; Green, 1976; 1983; Solomon et al., 1987). Figure 6-2 shows the location of the Rosebery deposit relative to the other four deposits and the main structural feature of the area, the Henty Fault. To the north-west of the Henty Fault, the Complex is composed of rhyolitic to dacitic acid lavas and pyroclastics and has a higher andesite content than those to the south-east (Corbett et al., 1974). Observed at parts of the Complex are massive banded pyrite-chalcopyrite and pyrite-sphalerite-galena ores which probably epitomize exhalative mineralization accumulation in topographic depressions of the seafloor (Solomon and Walshe, 1979; Large, 1990; Hannington et al., 2005; Petersen and Hein, 2013). The Central Volcanic Complex is unconformably overlain by the keratophyric tuffs (of ash fall and ash flow origin), massive agglomerates, conglomerates, sandstones, shales and limestones of the Tyndall Group (Solomon, 1964; Brathwaite, 1974; Corbett et al., 1974). During the Devonian epoch, shallow level post-tectonic granitoids intruded the mine area resulting in metamorphism and recrystallization of the ores (Hall and Solomon, 1962; Loftus-Hills et al., 1967; Green, 1983). In the immediate Rosebery mine area, the rock sequence consists of the following from bottom to top: (1) Foot-wall Pyroclastics of feldspar-phyric ash flow tuffs, (2) Tuffaceous Shale (the ore host rock), (3) Black Slates, (4) Hanging-wall Pyroclastics (epiclastics), and (5) Mount

Black Volcanics (dacitic to andesitic lavas) (Brathwaite, 1972; 1974; Corbett et al., 1974; Green et al., 1981; Green, 1983; Solomon et al., 1987; Large et al., 2001; Solomon et al., 2004; Seymour et al., 2007). The high angle reverse Rosebery Fault, though not shown here, truncates this sequence immediately to the west of the ore zone (Brathwaite, 1972; 1974). The Rosebery Fault is captured in more detailed geological maps of the study area such as in Solomon et al., (2004). The black slates and host rock form a lens at least 2,335 m in strike length. This lens pinches out to the north, but its southern limit has not been established (Brathwaite, 1974; Green, 1983). The rock sequence together with the VMS ore lenses formed the geologic model presented in Figure 6-3.

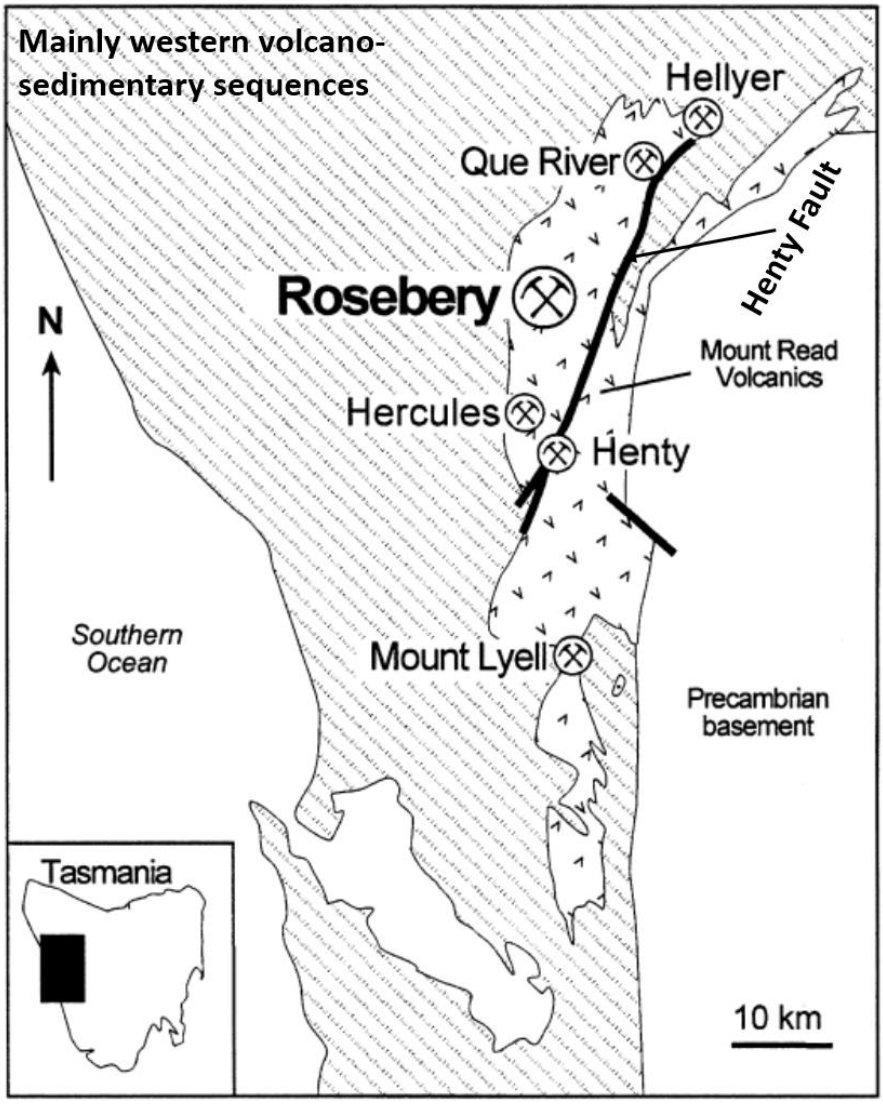

Figure 6-2: Map showing the locations of Rosebery and the other major VMS deposits within the Mount Read Volcanic belt, west coast of Tasmania (modified after Large et al., 2001).

The Rosebery VMS deposit is a strata-bound massive sulphide deposit of pyritic Zn-Pb-Cu-Au-Ag mineralization and barite associated with silicic pyroclastic rocks and considered to be a surface exhalative deposit with a large part formed below water level (Brathwaite, 1974; Solomon and Walshe, 1979; Green et al., 1981; Large, 1990). It is recorded that the VMS deposit was discovered in 1893 and full-scale production commenced in 1936 (Brathwaite, 1974). Large et al. (2001) recorded that the global mining resource of Rosebery deposit is about 28.3 million metric tons (mt), that is about 28.3 Mt, at 14.3 percent Zn, 4.5 percent Pb, 0.6 percent Cu, 145 g/t Ag, and 2.4 g/t Au. Since its commencement, significant amounts of base and precious metals of Pb, Zn, Cu, Au and Ag have been mined over the period (Brathwaite, 1974; Green et al., 1981; Huston and Large, 1988; Large et al., 2001).

Rosebery is made up of at least 16 individual ore lenses, which vary in size from 0.1 to 5 Mt, residing within an east-dipping sequence of volcanic and sedimentary rocks. The ore lenses occur along a strike length of over 2,000 m, which is also the approximate strike extent of the black slates, suggesting the area might define a basin (Brathwaite, 1974; Green, 1976; Green et al., 1981; 1983; Berry and Keele, 1997; Large et al., 2001; Solomon et al., 2004). The ore-bodies are concordant lenses, mostly tabular sheets up to about 12 m in thickness. Some of the ore lenses have a strike length of 100 to 400 m and a down-dip extent of 100 to 500 m. This resulted from deformation of the ore-body, enclosed by the host rock, into one main system of folds which have an associated axial plane and cleavage. The average strike and dip of the ore-body is 345^{o} at 45^{o} east, with the cleavage having a fairly uniform strike and dip of 350^{o} at 60^{o} east (Brathwaite, 1972; 1974; Green et al., 1981; Large, 1992; Large et al., 2001). The stacked stratiform ore lenses have undergone not less than two phases of Devonian deformation, including tight folding (Brathwaite, 1972) and thrust faulting (Green and Iliff, 1989; Berry and Keele, 1997). The combination of folding and thrusting has resulted in a complex pattern of ore lenses and alteration in the southern end of the mine (Berry, 1990; Large, 1990) according to the zonation. In comparison to the southern zone, the ore lenses in the northern end of the mine show less effects from the deformation (Green et al., 1981; Green, 1983; Huston and Large, 1988; Large et al., 2001). The southern zone is separated from the north end by weakly mineralized sericitic schist – a more or less zone of barren host rocks (Green, 1983; Green and Iliff, 1989). The VMS ore at Roseberry has overall down

plunged to a depth of more than 1,500 m (Brathwaite, 1972; 1974; Green et al., 1981; Green, 1983).

Dykes of basaltic composition are found in the mine area and to the west of Rosebery. In the mine, there is one main dyke about 1 m thick. Where it cuts through the ore-body, the dyke contains galena-chalcopyrite veinlets which are regarded as post-ore (Brathwaite, 1974).

6.3. Rosebery ground conditions test response to CSR

To test the CSR method at Rosebery, I have considered a simple geological model resembling the western portion of the generalized East-West southern section of the mine presented in Figure 6-3. A portion of the geologic model in Figure 6-3 considered for this test is from its up-slope to the point marked by the right bracket (in light blue). This simplified model consists of the black slates, the host rock, the mine foot-wall volcanoclastics, and a single elongated VMS ore lens. The elongated VMS ore lens is set to 8 m average thickness, it has a geologic dip of about 57 degrees (57°) and extends 100s of meters down-plunge. The simplified geologic model is provided in Figure 6-4. The model parametrisation assumes values provided in Table 6-1.

Across the mine area, arrays of diamond drill-holes are made from suitable underground drill chambers and from the surface, some having the same drill pad but drilled azimuthally at different angles (Huston and Large, 1988; Large et al., 1998). The orientation of the (surface) diamond drill-holes is from slightly slanting to almost curvilinear, but all the drill-holes are guided to intersect the dipping lithology at near normal incidence. Some of the surface drill-holes crisscross each other before finally intersecting the dipping lithology. In this test, the CSR source and receivers utilized two arbitrary boreholes using again typical separation of 100 m and 200 m. With these inter-borehole intervals, different scenarios involving different borehole geometries and source-receiver arrays are considered and are discussed.

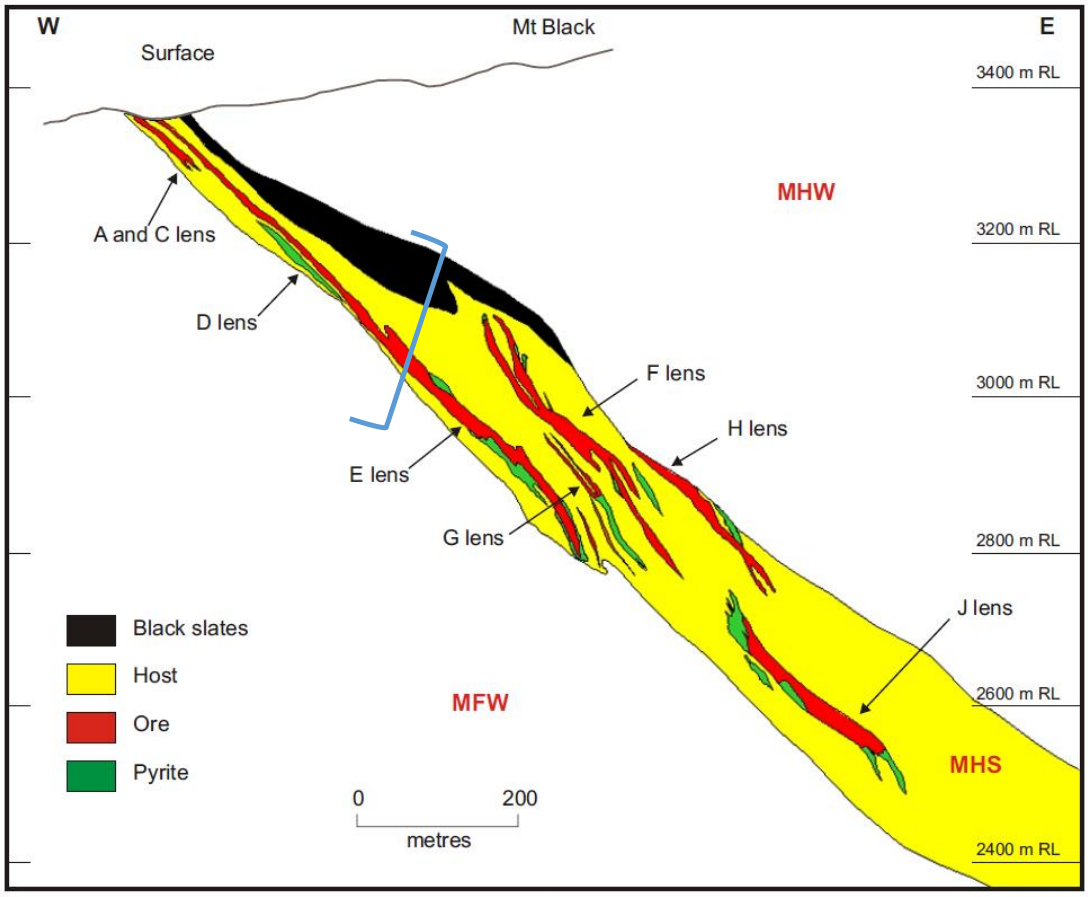

Figure 6-3: Generalized E-W cross section through the southern section of Rosebery mine at 500 N derived from underground and surface drilled holes. MFW – mine foot-wall sequence; MHS – mine host sequence; and MHW – mine hanging-wall sequence. (Cross section: Seymour et al., 2007, Mineral Resources Tasmania); Part of the geologic model for consideration is from the up-slope to the right bracket (in light blue) location.

6.3.1. CSR technique imaging of an elongated VMS ore lens

The synthetic study consists of two different scenarios with the same geologic model. In the first part, synthetic migrated images of VMS ore lens with different shot point densities but same shot aperture are analyzed. The second part compares migration imaging of VMS ore lens using different borehole configurations. This is meant to determine primarily the effect of shot density and borehole geometry on the CSR imaging capability in terms of image recovery and its extent.

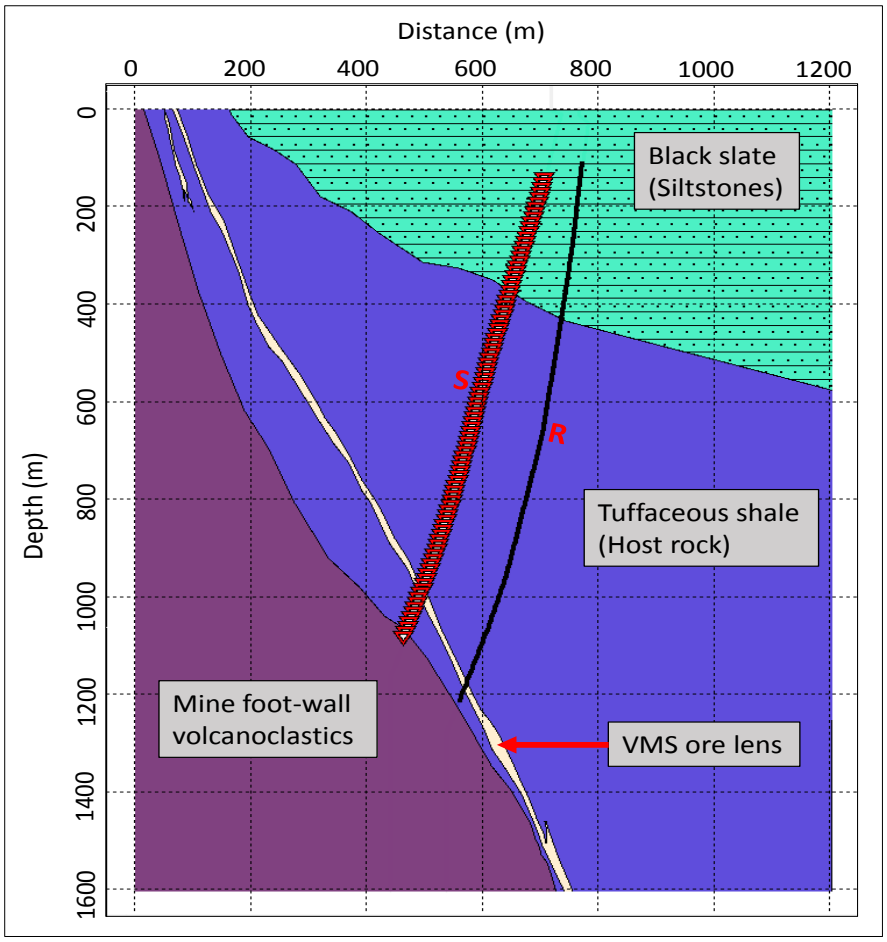

Figure 6-4: The synthetic geologic cross section resembling the western part of the generalized East-West southern section of the Rosebery mine simplified from Figure 6-3. (Note: The cross section is not drawn to scale). The red triangles are shot points; black dots are borehole receivers.

Table 6-1: Acoustic impedance of various rock layers (courtesy HiSeis Pty Ltd).

Rock type	P-wave velocity ,v, (ms^{-1})	Density ,ρ, (kgm^{-3})	Acoustic impedance , ρ * v x10^6, ($kgm^{-2}s^{-1}$)
Black slate (Siltstones)	5100	2760	14.08
Tuffaceous shale (Host rock)	5300	3083	16.34
VMS ore lens	4400	4690	20.64
Mine foot-wall volcanoclastics	5500	2700	14.85

6.3.1.1. CSR imaging comparison for different shot densities

The CSR synthetic data for the model shown in Figure 6-4 were generated with a 100-m source-receiver borehole separation and used forward approach crosshole shooting geometry. Modelling parameters are provided in Table 6-2.

Table 6-2: Modelling parameters for the CSR synthetic data generation.

Type of Geometry	Parameters and values				
	Sources	**Receivers**	**Wavelet**	**Sample rate**	**Record length**
CSR, forward, 100 m inter-borehole interval (at the basement)	95 at 10 m, and then 50 m and 100 m spacing	221 at 5 m spacing	Ricker 120 Hz	0.4 ms	400 ms
CSR, forward, 200 m inter-borehole interval (at the basement)	95 at 10 m spacing	247 at 5 m spacing	✓	✓	✓

Figure 6-5 displays the time snap shot for T=106 ms and the corresponding synthetic seismic record for shot point 57. Two distinct up-going reflected waves are identified emanating from: 1) the host rock-VMS ore lens contact (green broken line) and 2) the host rock-mine foot-wall (MFW) contact (yellow broken line). The down-going reflection from the black slate-host rock contact is shown with black arrow line. The shot point is not indicated but lies below the black slate layer.

The raw shot records are presented in Figure 6-6. Up- and down-going reflections from the slate-host rock contact are indicated respectively as Um and Ud. The green circled denotes shot point located very close to the black slate-host rock interface. The host rock-VMS ore lens interface and the host rock-MFW contact reflections are indicated respectively as R_1 and R_2. These events are overwhelmed by the transmitted waves.

Similar processing was assumed as before except Ormsby band-pass filter was set to a range 10-45-170-290 Hz to cut off unwarranted frequencies. The resulting seismograms after wavefield separation are shown in Figure 6-7 and consist primarily of the reflected waves of interest, their multiples, and remnants of up-going reflection multiples and down-going surface reflected waves.

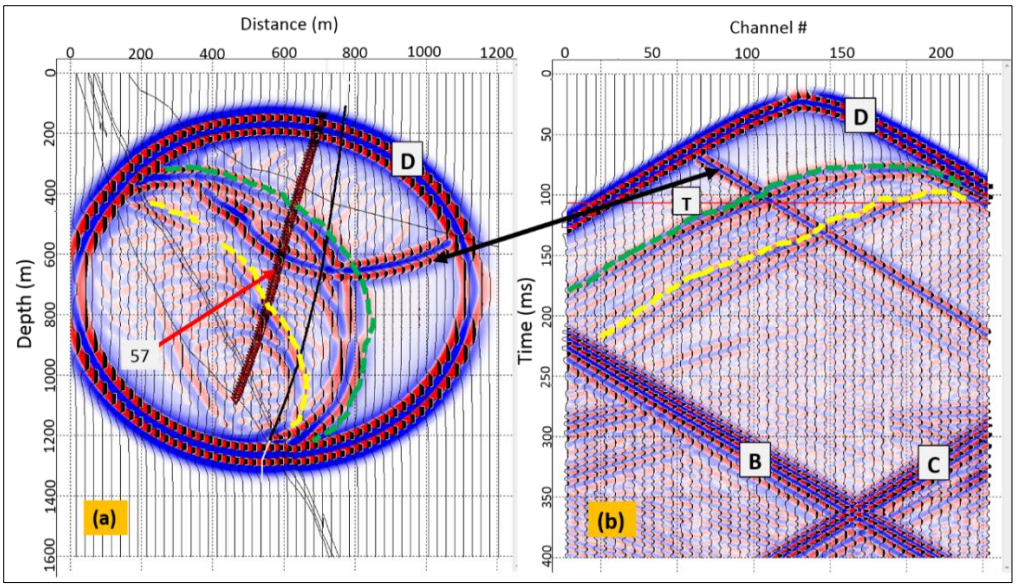

Figure 6-5: (a) Snap shot at 106 ms and (b) Synthetic seismogram for shot point 57. Green broken line – reflected up-going wave from host rock-VMS ore lens, yellow broken line – up-going reflection from the host rock-mine foot-wall (MFW), black solid double-arrow line – reflected down-going wave from black slates-host rock contact, D – the spherically propagating direct wave, B – surface reflected down-going wave, and C – some up-going multiples.

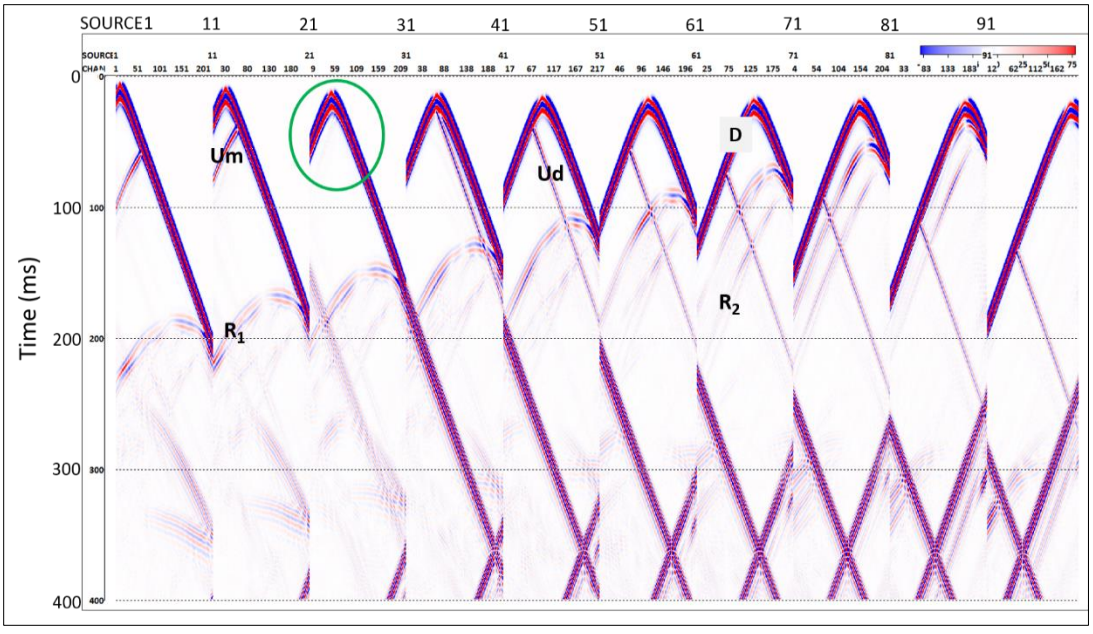

Figure 6-6: Synthetic CSR shot records for the model in Figure 6-4. It is displayed for every 10th shot. D – direct wave, Um – up-going reflected wave from the black slate-host rock contact, and Ud – down-going reflected wave from the same rocks contact. Green circle portion – shot point location almost at the black slate-host rock contact (neither Um nor Ud present). R_1 is the host rock and VMS ore lens interface reflected wave and R_2 is the host rock and mine foot-wall (MFW) interface reflected wave. Other identified wavefields are indicated in Figure 6-5.

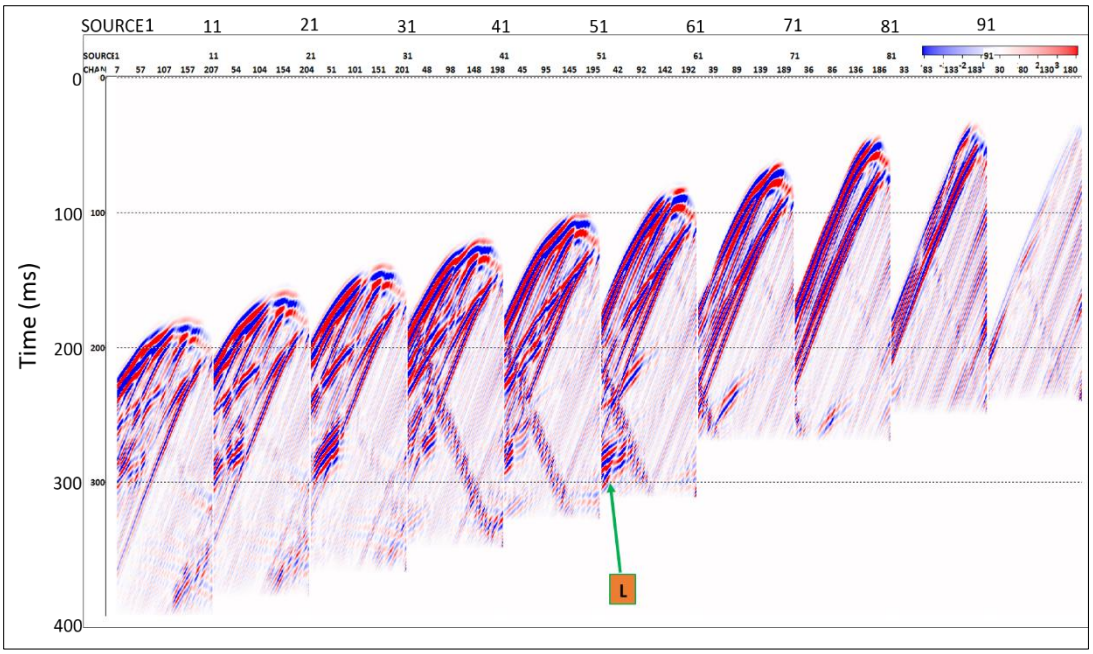

Figure 6-7: Up-going wavefield preserved after wavefield separation processing. It is shown for every 10th shot. There is a gain in energy of reflected waves of interest when the direct wave is removed. L - remnants of up-going reflection multiples.

In the migration process, only shot points and receiver stations above the VMS ore lens are used. A host rock velocity of 5300 ms^{-1} was used. In the migration process, various migration apertures and dips have been trialled. Results show that constricting the aperture clearly defines the extent of plausible imaging and reduces the effect of migration smiles but brings a consequential reduction in sharpness of the image. Results of two sets of migration aperture and dip have been selected for comparison: migrated images obtained with 1° and 5.5° migration apertures and a structural dip of 56°. These are presented in Figure 6-8. The migration image obtained with 1° aperture terminated the up-dip reflector and defined the extent of plausible imaging but slightly deforms the image towards the centre of the reflector. An improved fidelity image is obtained with 5.5° migration aperture image but with some migration smiles created at the termination. It is interesting to note that the smearing of the reflector does not occur in down-dip direction, where the imaging is naturally restricted by the geometry of the sources and receivers. Subsequently higher migration aperture values were tested which provided a higher fidelity image towards the centre of the reflector but with increasing diffraction smiles created at its edge, hence improving the sharpness of the image towards the centre but producing migration smiles towards the edge of the display.

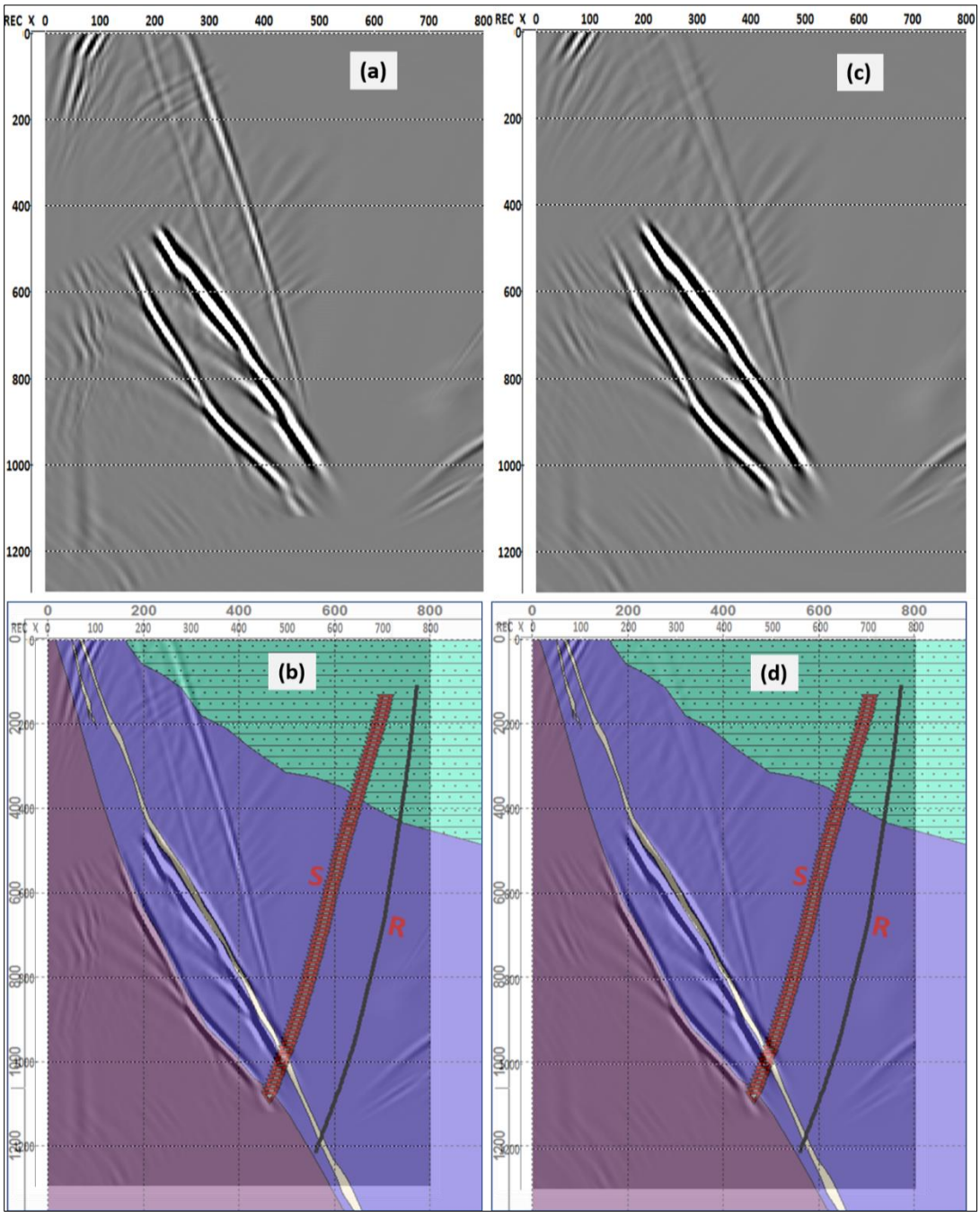

Figure 6-8: PSDM images obtained at two different migration apertures (a) 1° and (c) 5.5° with their overlain geologic models shown respectively in (b) and (d). All the migrated images were focused at 56° preferential slope.

Finally, a 10° aperture value is selected that provides migrated image that strikes the balance between sharpness of image towards the centre and creation of migration smiles at the edge of the display. This is shown in Figure 6-9. The MFW-host rock contact is well imaged as indicated with a red arrow. These parameters were used for subsequent tests.

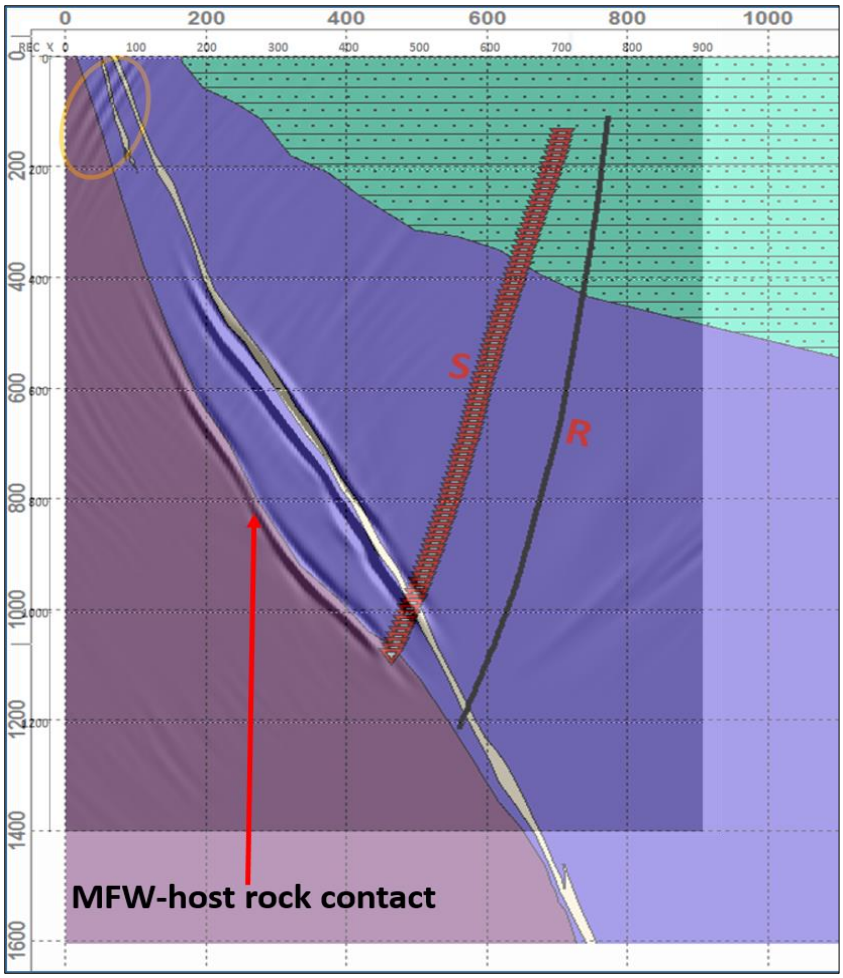

Figure 6-9: CSR pre-stack depth migration (PSDM) image obtained with the 10 m source spacing. The migrated space is 0 to 900 m for a depth range 0-1400 m. Migration dip is 56°, migration aperture dip of 10°. The orange circle indicates migration artefacts from unseparated wavefields.

Figure 6-10 displays migrated images obtained with equal shot aperture but variable shot spacing of 10, 50 and 100 m. The receiver array, data processing and migration approach were unaltered. All of the images are of good quality which is to some extent expected for the numerical data.

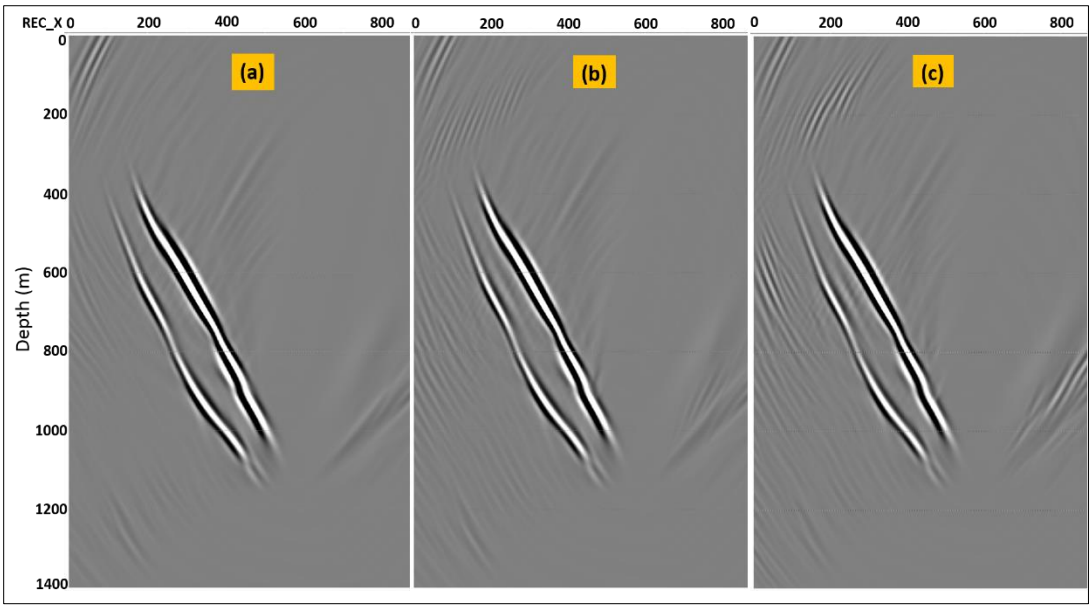

Figure 6-10: Comparison of CSR PSDM images for different shot densities: (a) 10 m, (b) 50 m, and (c) 100 m. The same migration parameters for Figure 6-9 were used for all. All the images have been set to the same visualization gain. Relatively coarse shot points provide images comparable in quality to much denser shooting geometry.

6.3.1.2. CSR VMS ore lens imaging at different boreholes separation

In this second test the source borehole remains the same as in scenario 1. Number of source points remains the same as well as the source separation of 10 m. The receiver borehole is moved down-slope 100 m making the inter-borehole separation of 200 m. The number of receiver stations is more than used in scenario 1 but the receiver spacing remains at 5 m. Figure 6-11 compares the CSR images, for scenarios 1 and 2 that is borehole separation of 100 and 200 m, respectively. Both images are of a high quality. Some smearing is present and is marked with the red ellipse in Figure 6-11. Partial imaging occurred between the boreholes in the two borehole geometries. This has been red circled in (a) and (b) of Figure 6-11 for the respective borehole geometry. Increase in the inter-borehole distance enabled more inter-borehole surface area of the target to be illuminated resulting in more partial imaging in (b) than in (a). Increase in borehole separation, however, brings a corresponding artefact into the migration section as indicated by the larger orange circle in (b). In the two migrated sections, the depths to the reflector and the dip have been accurately represented.

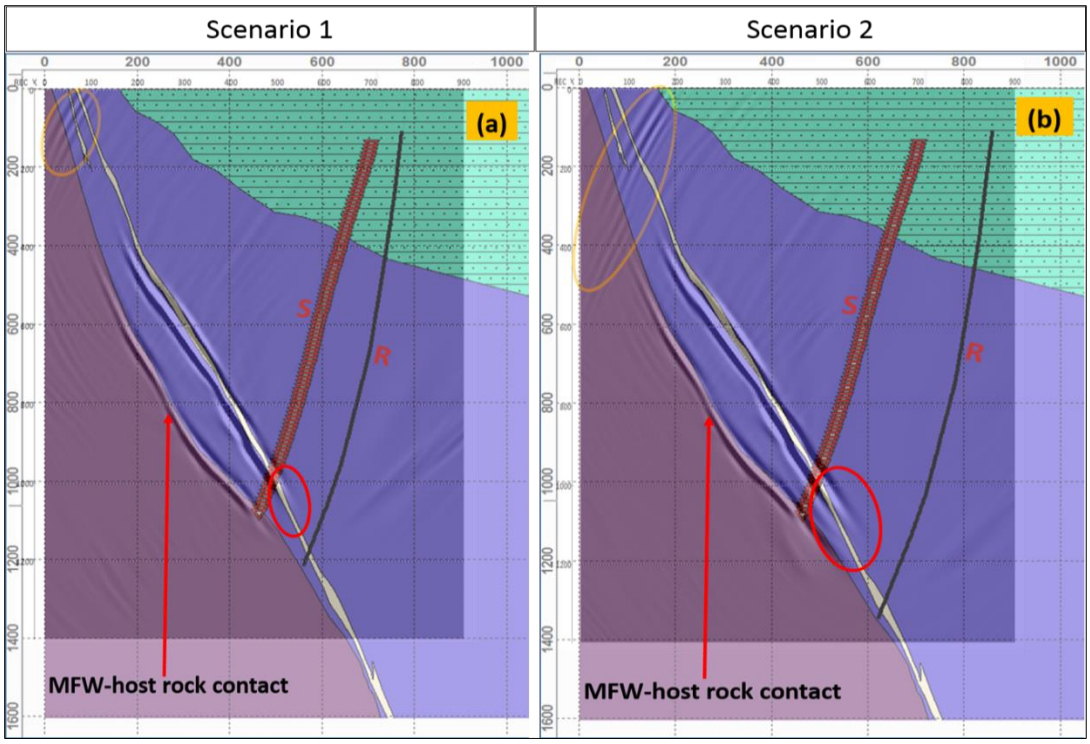

Figure 6-11: The CSR images for: (a) 100 m and (b) 200 m borehole spacing. All the images have migrated image space of 0 to 900 m and to a depth of 1400 m. The migration aperture is 10° and the migration has been made to focus the images at 56°.

6.4. CSR to delineate cluster of Rosebery VMS ore lenses

The deposit consists of at least 16 lenticular massive sulphide ore lenses with varying size and strike lengths (Green et al., 1981; Green, 1983; Large et al., 2001). To investigate the potential of the CSR method to delineate a Rosebery-like VMS cluster of ore lenses, the full cross section of Figure 6-3 is used to create the model presented in Figure 6-12. Velocity-density values are as in Table 6-1 but added are those of the mine hanging-wall felsic volcanics. Modelling parameters are provided in Table 6-3. A forward shooting source-receiver borehole geometry was used.

A stepwise approach has been adopted in generating the synthetic CSR data. The first synthetic data and PSDM image have been obtained for the deeper theoretically unknown ore lens J. The PSDM image of this ore lens then compared with the known geology and also with a pre-stack time migration (PSTM) 3D image of the study area obtained by HiSeis Pty Ltd. The second set of synthetics run involved both J and H lenses, then with J, H, and F, and then finally for all the ore lenses.

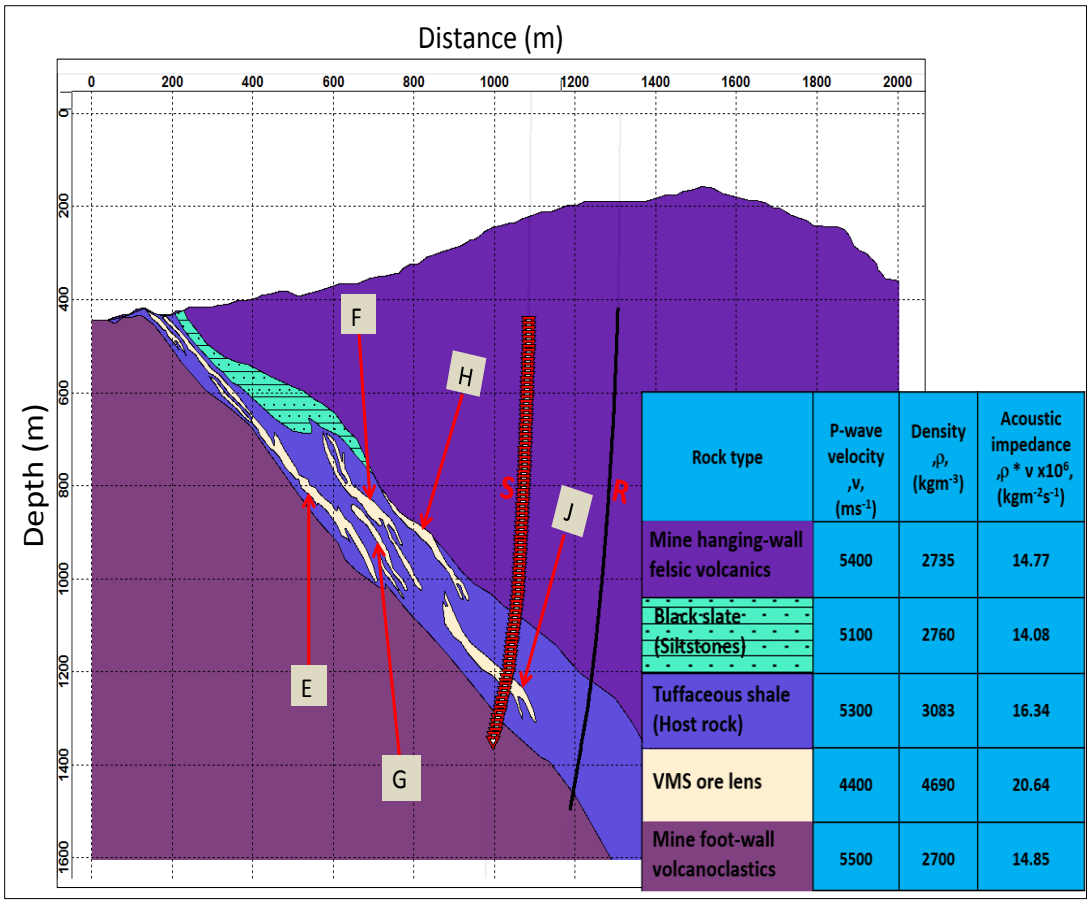

Figure 6-12: The numerical model of the generalized E-W cross section through the southern section of Rosebery mine at 500 N. Labelled with letters (indicated by the red arrows) are the ore lenses to image. Also shown is the crosshole geometry; S - source borehole and R - receiver borehole. Note: In the modelling, for uniform reflection pattern, VMS petro-physical values are assigned to pyrites.

Table 6-3: Modelling parameters for CSR synthetic data generation on cluster of VMS ore lenses.

Type of Geometry	Parameters and values				
	Sources	**Receivers**	**Wavelet**	**Sample rate**	**Record length**
Normal, 200 m inter-borehole interval (for first run; for ore lens J)	92 at 10 m spacing	217 at 5 m spacing	Ricker 120 Hz	0.4 ms	270 ms
Normal, 200 m interval for all other runs	✓	✓	✓	✓	400 ms
Normal, about 160 m interval (for a later run on up-slope ore lenses)	67 at 10 m spacing	169 at 5 m spacing	✓	✓	280 ms

6.4.1. CSR imaging of the deeper theoretically unknown ore lens J

The wavefield propagation snap and the corresponding synthetic seismogram for shot point 43 at 111 ms for ore lens J are presented in Figure 6-13. The major wavefields identified have been indicated.

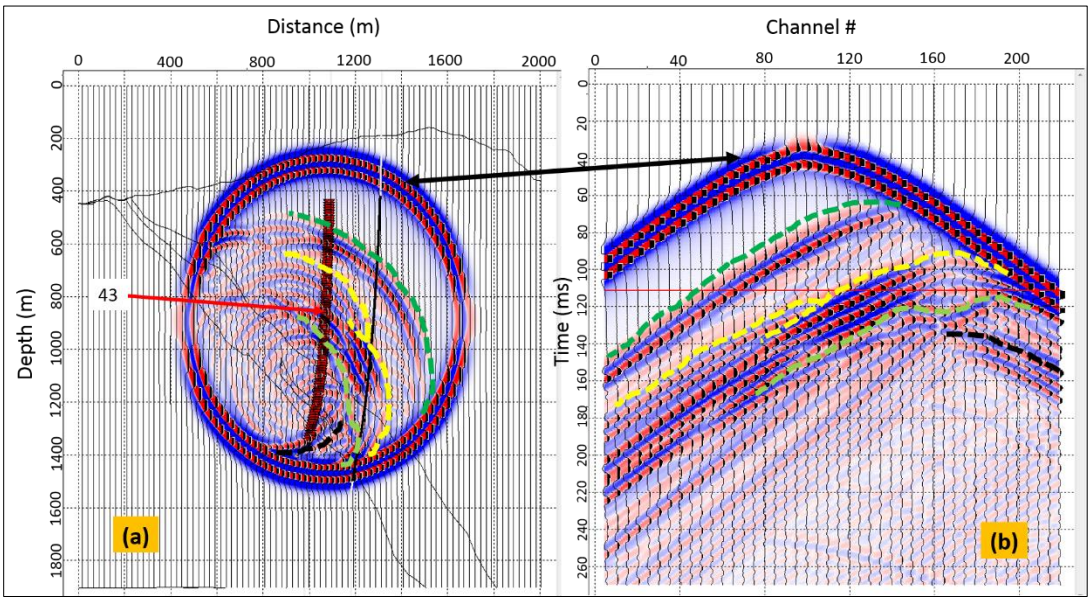

Figure 6-13: (a) CSR wavefields propagation snap for shot point 43 at 111 ms, (b) the corresponding synthetic seismogram. In both (a) and (b): green broken line – reflected up-going wave from the upper part of the host rock, light green broken line – reflected up-going wave from the host rock-mine foot-wall contact, yellow broken lines – reflections from the J ore lens, black solid double-arrow line – spherically propagating direct wave, and black broken line – some down-going multiples.

Figure 6-14 displays the 43rd shot point wavefield propagation generated for ore lens J only and for all ore lenses. While the reflections from the various rock boundaries are relatively identifiable in the case for the J ore lens, only the up-going reflection from the upper boundary of the host rock is clearly identifiable in the case for all ore lenses. Figure 6-15 shows wavefield separation result. The wavefield separation was successful with the minimum artefacts left in the data. A clear difference in complexity exists between the displayed wavefield separated seismograms of J ore lens and of all ore lenses. The preserved reflected wavefield of interest for all ore lenses is far more complex than that of the J ore lens which is a direct reflection of the reflected waves pattern presented in Figure 6-14.

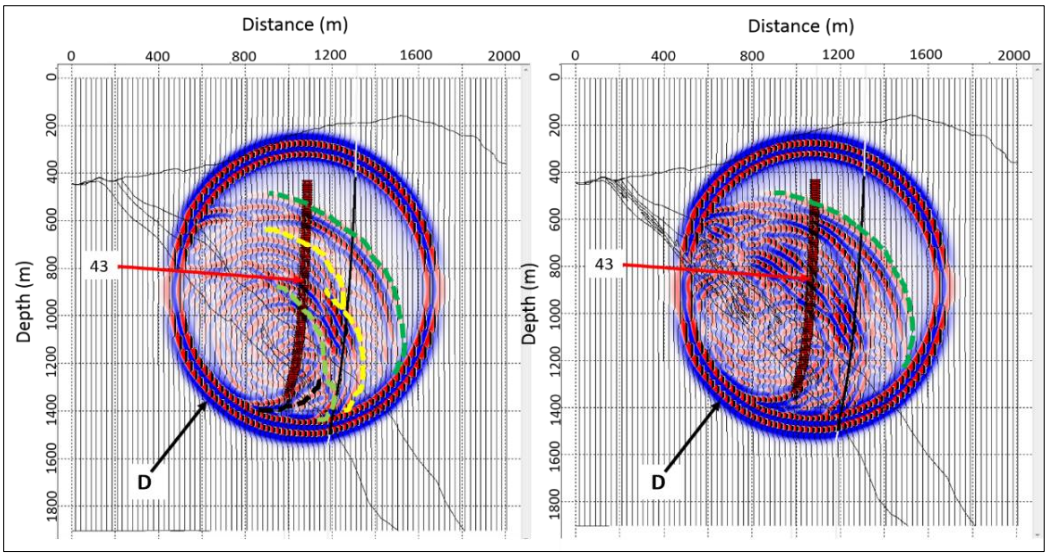

Figure 6-14: Wavefield propagation for shot point 43 at 111 ms for J ore lens (left panel) and for all the ore lenses (right panel). Complexity of wavefields increases with increasing ore lenses. D - spherically propagating direct wave.

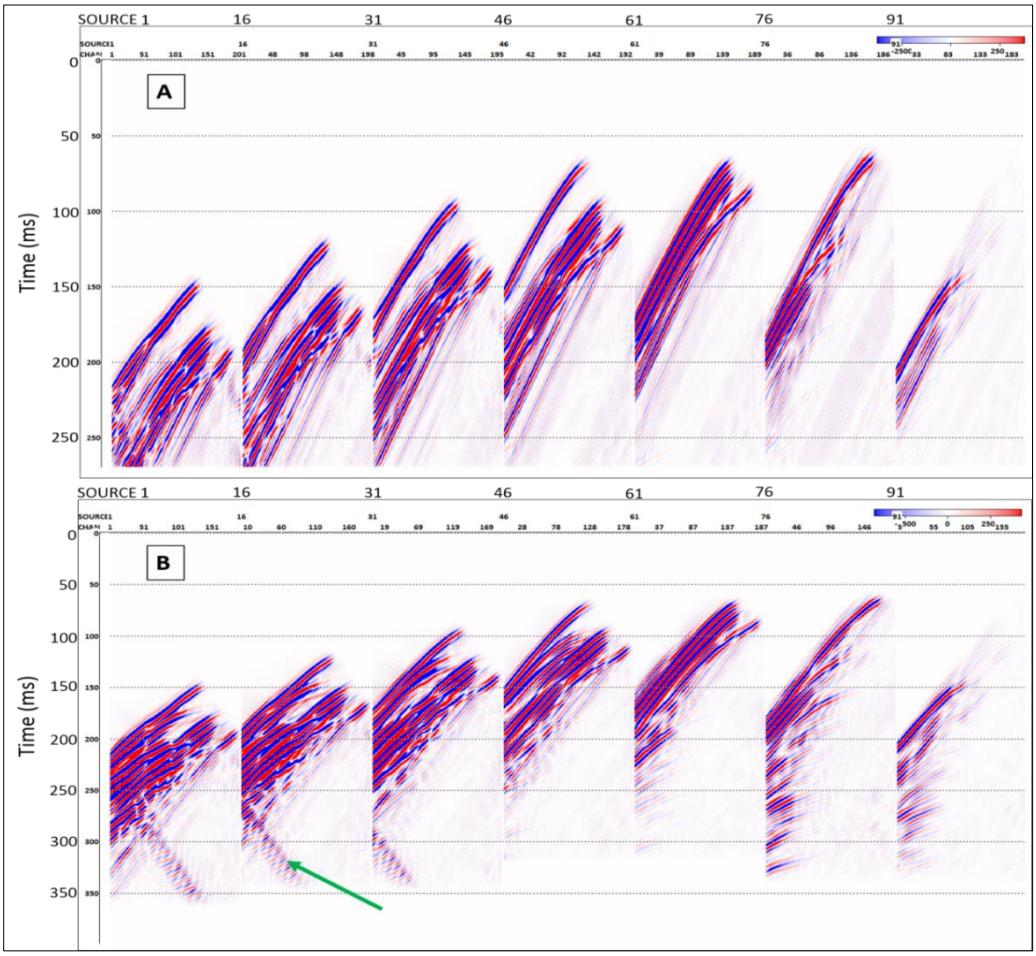

Figure 6-15: Preserved wavefields after wavefield separation processing. Panel A: for only the J ore lens. Panel B: for all the ore lenses. Seismograms are shown for every 15th shot. Green arrow indicates remnant energy of a down-going wavefield.

The migration was guided to focus the image at 48° with the best aperture migration of 12°. The PSDM image obtained and the migrated section/image overlain with the geologic section are shown in Figure 6-16. An arrow marked J indicates the J ore lens and the arrows HR indicate the boundaries of the host rock. With the overlain geologic section, the migrated image of the ore lens mapped the dip, location, and the depth of the J ore lens accurately.

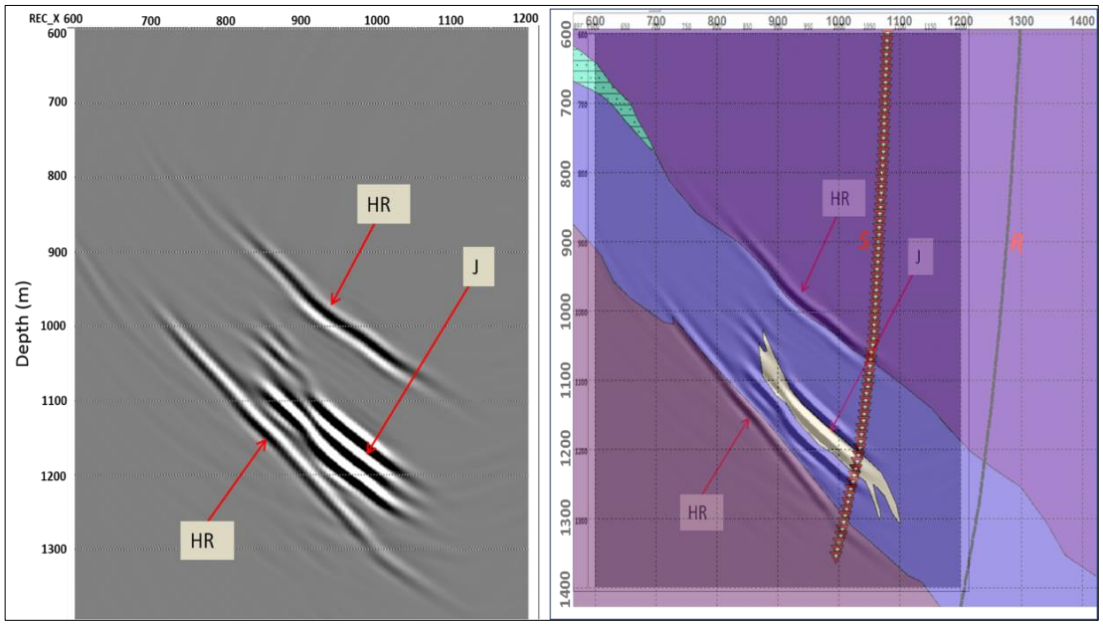

Figure 6-16: Left: PSDM image of the J ore lens. The migrated image space is from 600 to 1200 m and a depth of 1400 m with a migration aperture of 12°. The migration focused the image at 48° dip. Right: Migrated image with the geologic section overlain. In both panels, J – the J ore lens and HR – the host rock boundary.

6.4.2. Comparison of numerically modelled PSDM image of the J ore lens with a PSTM 3D image of the study area (field data)

The synthetic CSR PSDM image of the J ore lens compared with a real data pre-stack time migration (PSTM) image extracted from a 3D cube over the study area is shown in Figure 6-17. The synthetic PSDM image section and the real data PSTM image section are obtained with different methods, their processing approaches totally different, and are of different scale. However, the synthetic CSR PSDM image compares favourably with the real data PSTM image in terms of resolution, shape, fidelity, and dip of the image.

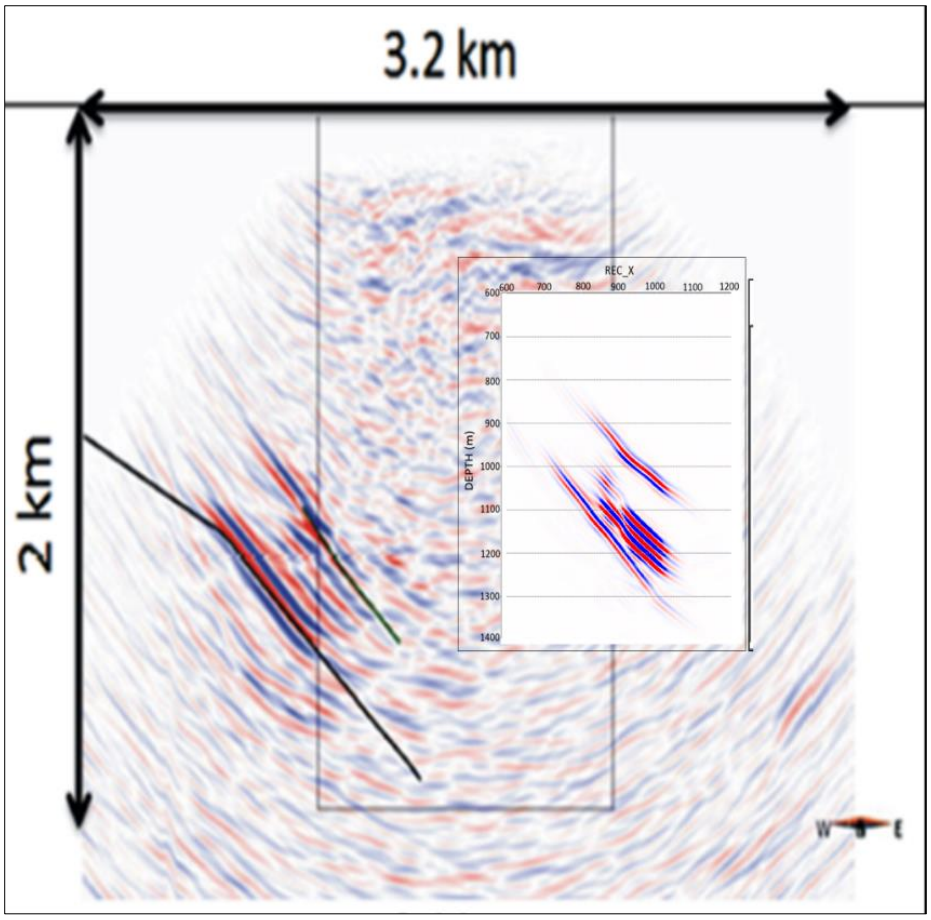

Figure 6-17: A PSDM synthetic image of the J ore lens obtained with the CSR method overlain onto a conventional AGC PSTM expanded geometry from arbitrary crossline of the cube of the study area. In both techniques, the J ore lens' image compares very well. (AGC PSTM image courtesy HiSeis Pty Ltd (pers. commun.)).

6.4.3. CSR migration imaging of multiple ore lenses

Successive CSR imaging is performed after including additional lenses. Same migration parameters are used for all cases (dip 48° and migration aperture 12°) for data migration. Migration image depth also remains same for all cases but migrated image space varies. Image space of 600 - 1200 m is used in imaging ore lens J and ore lenses J and H, and 500 - 1200 m in imaging ore lenses J, H and F and in the case for all ore lenses. Figure 6-18 and 6-19 demonstrate that CSR imaging can recover multiple lenses with a striking precision albeit some small migration tails and smearing are unavoidably present. Finally, all ore lenses are included to further challenge CSR imaging capabilities. Fairly complex and variable snap shots are produced (refer to Figure 6-14). The resulting wavefield separated seismograms

obtained for all ore lenses has been presented in Figure 6-15. The CSR migrated result of all ore lenses is shown in Figure 6-20. A good portion of ore lens G, labelled G′, was imaged. The host rock boundaries are equally well mapped. However, no clear part of ore lens E has been imaged. In other words, with the current source-receiver geometry, ore lenses J and H were well imaged, ore lenses F and G were partially imaged, but the ore lens E was not imaged at all.

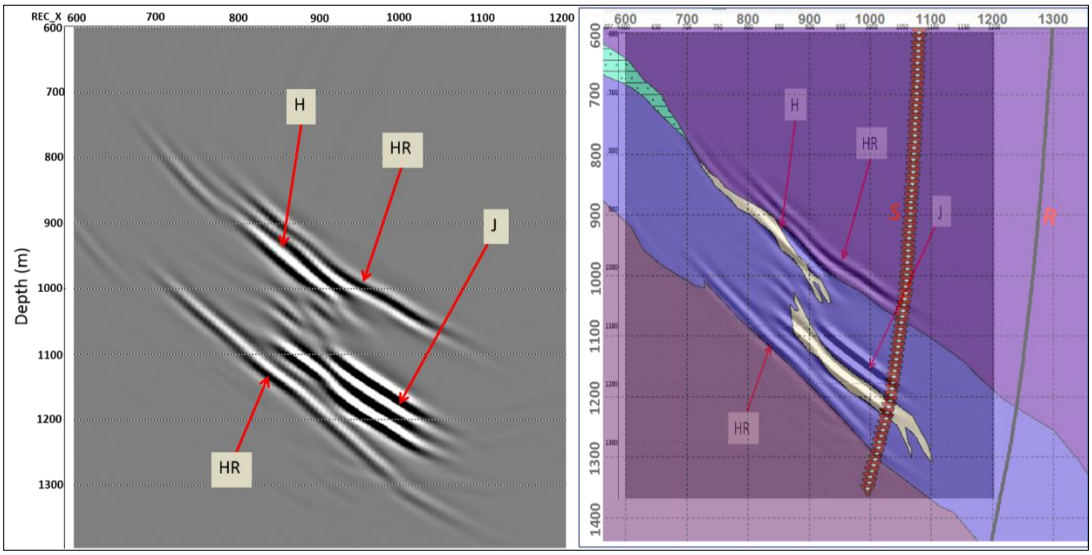

Figure 6-18: The migrated image of the J and H ore lenses (left) overlain onto geologic section (right). The migrated image space is 600 to 1200 m and to a depth of 1400 m. HR is the host rock boundary.

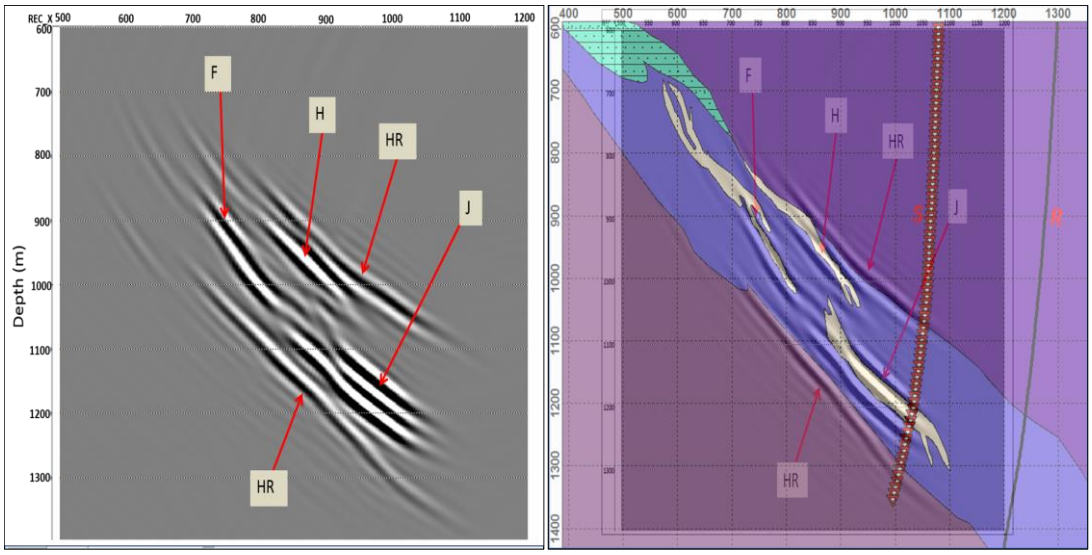

Figure 6-19: Left panel: Migrated section of the J, H, and F ore lenses. The migrated image space is 500 to 1200 m and to a depth of 1400 m. Right panel is migrated image overlain onto the geologic section.

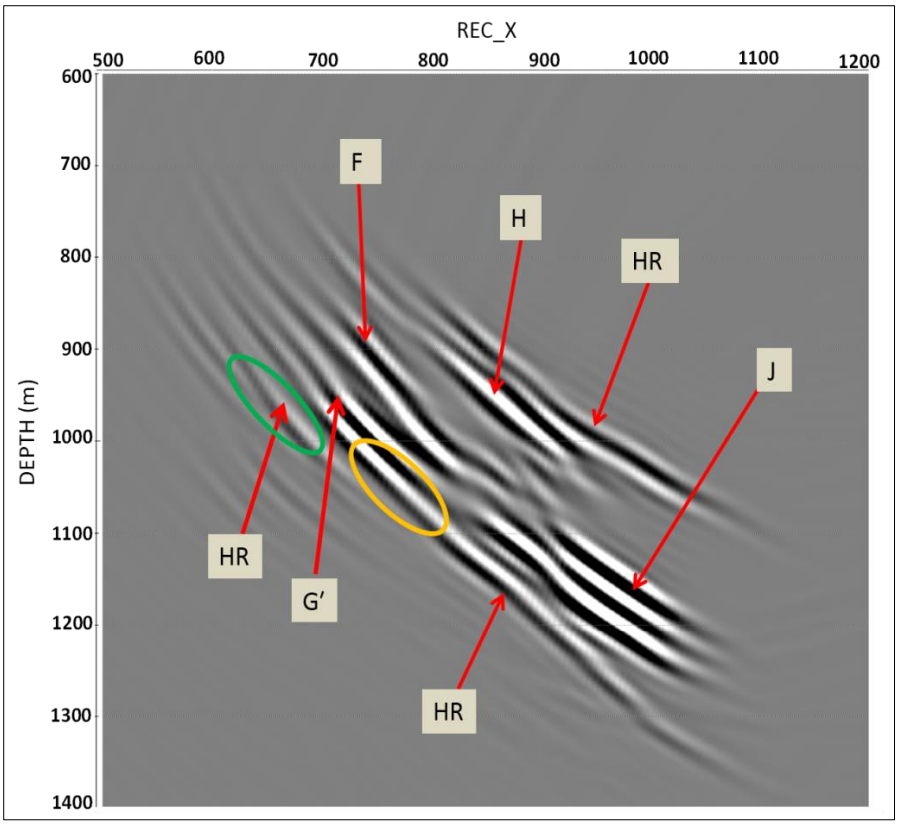

Figure 6-20: The migrated section obtained for the case when all ore lenses are built into the model. The migrated section has image space of 500 to 1200 m and a depth of 1400 m. G′ indicates part of ore lens G imaged. Other features are as indicated previously. The green circled portion is most likely part of the host rock boundary. Within the orange circle, neither the ore lens G nor ore lens E nor the host rock boundary could clearly be differentiated.

In addition to other features, part of the host rock boundary seemed to have been imaged and indicated by the green circle. Within the area circled in orange, it is not definite if it is the ore lens G or E or even the host rock boundary that has been imaged or if it is overlap of features from them. Still the amount of geological details recovered is impressive.

In a quest to recover all geological features I assumed additional pair of boreholes, S′ as the source borehole and R′ as the receiver borehole, located up-dip the slope (Figure 6-21). In this, the source borehole intersected ore lenses H, F and G while the receiver borehole intersected the H and J ore lenses. The resulting PSDM image obtained is presented in Figure 6-22. Interpretation of this image is not easy despite the geology is exactly known. After some analysis ore lenses H′, F′, and G′ have

been identified and labelled as partially recovered images of the respective ore lenses H, F, and G. Ore lens E is also now recovered. Some artefacts are present on the migration section. Generally, the lenses caused seismic energy to be scattered and diffracted resulting in imaging artefacts. As the result, some parts of the image are as indicated as artefacts by a blue circle in Figure 6-22. One noticeable feature on the migration section is labelled FWHR. It is the migrated image of the mine foot-wall discontinuity.

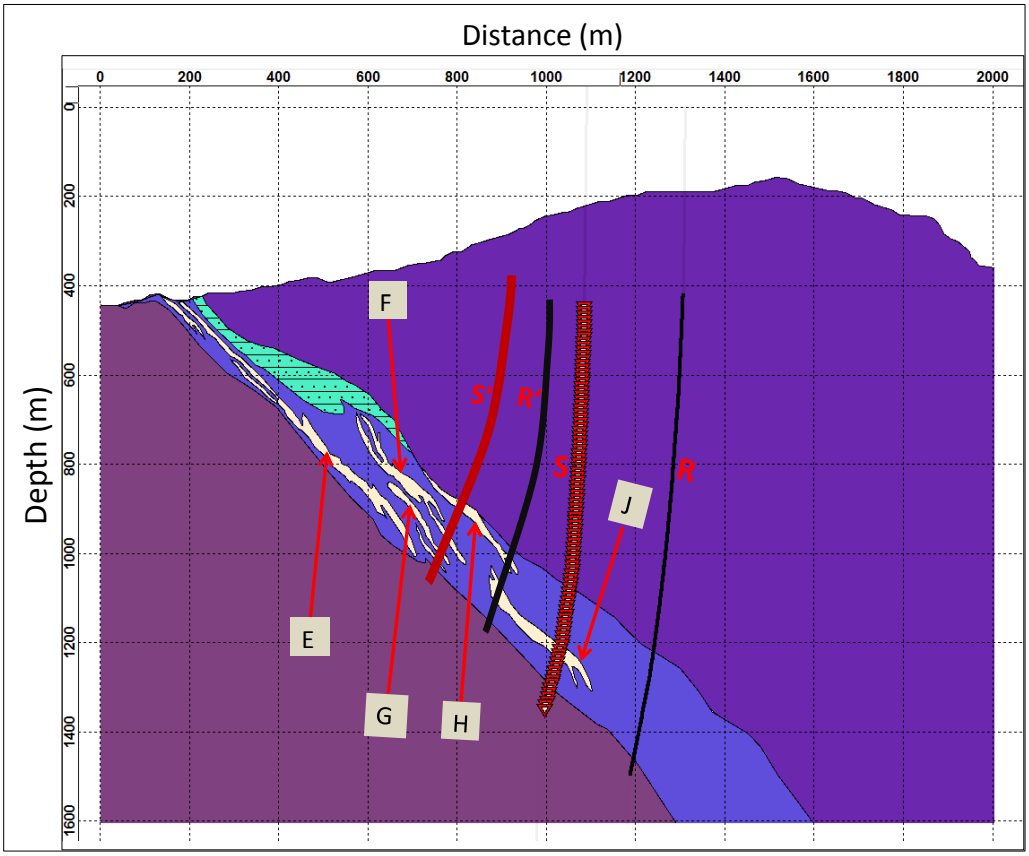

Figure 6-21: The same numerical model in Figure 6-12 but there is another pair of source (S')-receiver (R') boreholes.

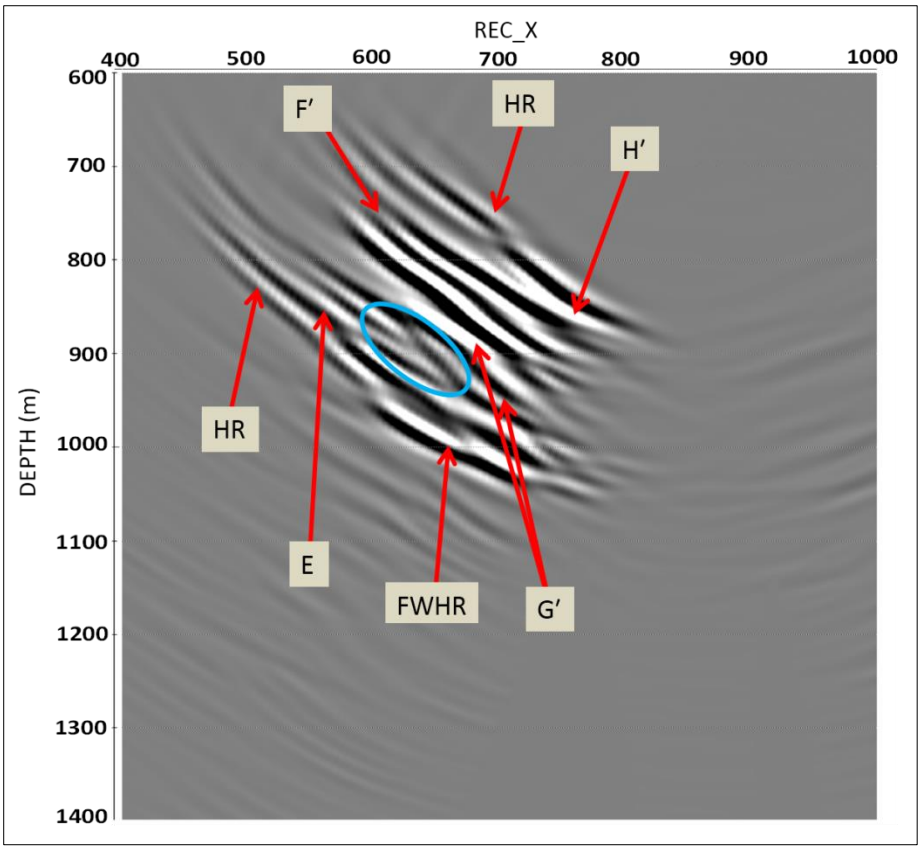

Figure 6-22: Migrated section obtained by using a pair of up-dip source (S')-receiver (R') boreholes. Partially recovered lenses are labelled with primes. Portion circled in blue – scattered and diffracted seismic energy caused by ore lenses resulting in imaging artefacts. FWHR is the image of the mine foot-wall discontinuity. All other events labelled have same meaning as previously defined.

Finally, an ultimate image is presented in Figure 6-23. The CSR image is obtained here by adding together the PSDM sections of Figures 6-20 and 6-22. The migrated images of lenses J, H, F, and G are well presented. The E ore lens is imaged although it is not entirely delineated. The result provides a clear image of the host rock boundaries (the upper and the lower boundaries are clearly indicated). The blue and orange circled portions have the same interpretation as previously given. The weak reflection amplitudes seen in Figure 6-20 have now been reinforced. The geologic model, with the source-receiver boreholes locations, superimposed on the migrated section (Figure 6-23), is presented in Figure 6-24 to show the performance of CSR imaging. The depth and dip of practically all geological features have been successfully recovered by the process of two by two borehole combined CSR imaging.

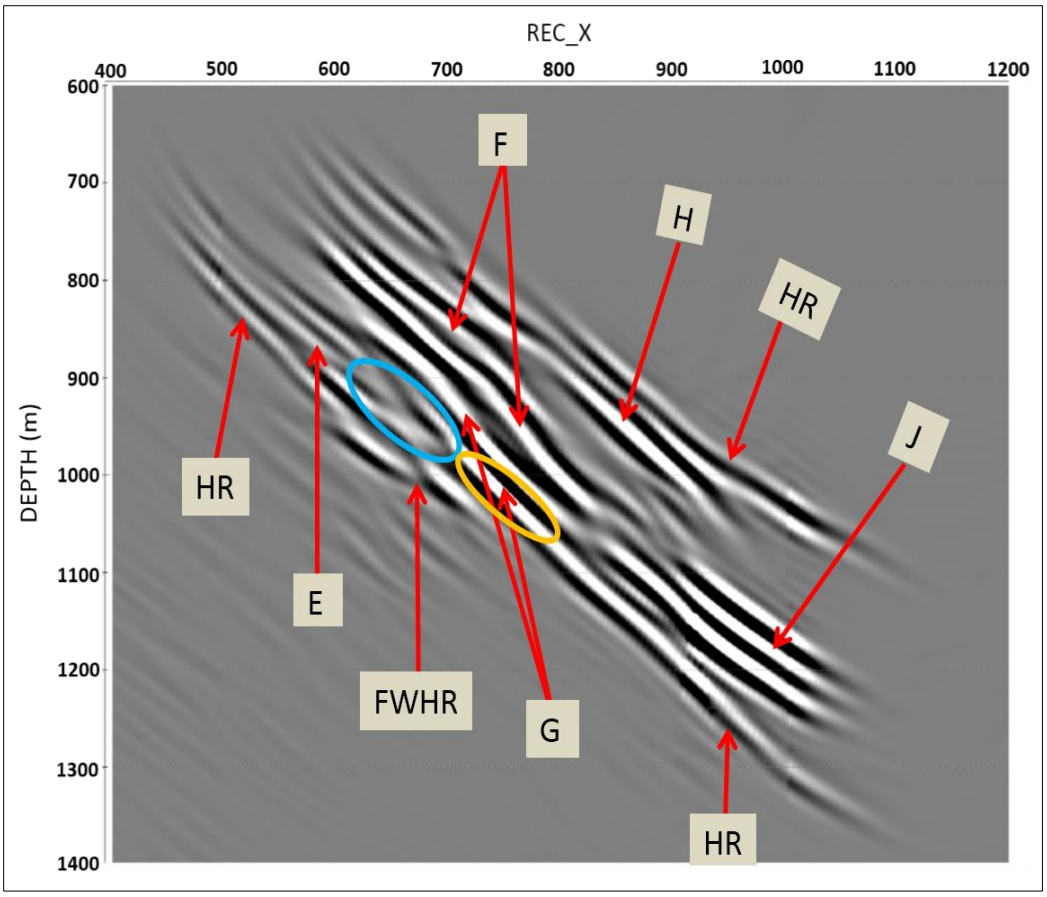

Figure 6-23: The overall PSDM image obtained by stacking sections in Figures 6-20 and 6-22. It has a migrated image space of 400 m to 1200 m and a depth of 1400 m. The aperture of migration is 12° and the migration focused the image at 48° dip. HR – host rock boundary imaged, FWHR – image of the mine foot-wall discontinuity. The orange and blue circled portions meant same as explained in Figure 6-20 and Figure 6-22 respectively. Other labels denote the respective ore lenses imaged.

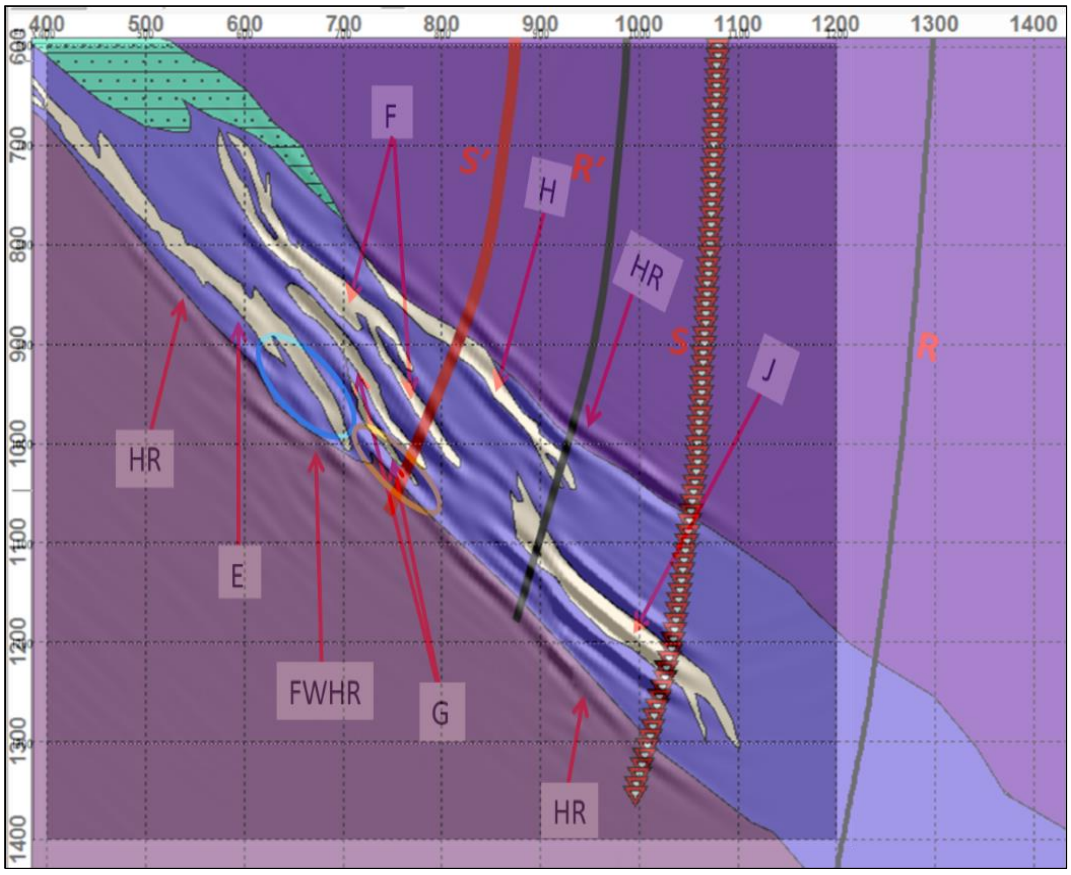

Figure 6-24: The migrated section in Figure 6-23 superimposed by the geologic section. The various VMS ore lenses imaged are as indicated against their location on the geologic section. Also, the imaged mine foot-wall discontinuity, FWHR, and the host rock upper and lower boundaries, HRs, are as indicated.

6.5. Summary

The seismic response of Rosebery underground geology was tested in several stages, by gradually increasing the model complexity and investigating the best ways of recovering it by CSR imaging process. It was shown that for relatively low geological complexity shot density is of the second importance for the image quality. This opens the possibility for more flexible field acquisition parameters.

The model was further adapted to image a cluster of VMS ore lenses. This very complex geological model was eventually recovered through a series of imaging steps and follow up analysis. Optimum parametrisation of the imaging was the first and the necessary step in recovering underground geology. This has been

accomplished by careful analysis of the resultant image in terms of both geology and produced artefacts.

The results of Figure 6-23 show that by adding additional boreholes or stacking images of individual pairs of boreholes, CSR imaging is capable of recovering extremely fine and complex geological features.

7. Thesis summary, discussions and conclusions

7.1. Ore-body delineation potential of the CSR method

This research was initially inspired by the decreasing rate of mineral discoveries and the necessity of introduction of seismic methods into mineral exploration practice. This idea of the study is to inspire and encourage utilization of borehole seismic surveys to delineate steeply dipping mineralization that are posing serious challenge to surface reflection methods. High resolving power and imaging precision of CSR method can be used to resolve many other mining issues. It can be, for example, deployed to de-risk mine development and planning by detecting structures hazardous to mining operations.

Downhole EM may be powerful in detecting some types of mineralized bodies, but it is not good in delineating geometry of a body. This is where CSR may be a method of choice to complement exploration drilling and reserve estimate. Since CSR does not suffer from access restrictions and has superior resolution to any other geophysical method it could become a method of choice for delineation of deep and complex mineralized bodies.

For the analysis, I have selected different geological scenarios in order to test and evaluate the imaging potential of the CSR method. Currently, most of the mineral companies are unaware of the potential of crosshole surveys and are exhausting exploration budget on deep drilling of sub-vertical mineralization where surface seismic is of a little help. This fact was the prime motivation for the selection of the sites analyzed in this work. Numerical tests with CSR method were performed on magmatic nickel sulphides within Komatiite environments (Kambalda types) of the Yilgarn Craton province, Western Australia, and Volcanic-hosted massive sulphide deposits, Rosebery complex ore lenses, Tasmania, Australia. Under the Kambalda type nickel sulphide mineralization, categories of deposits with different deposition styles were considered namely: McLeay nickel sulphide ore deposit, Maggie Hays North (MHN) and Maggie Hays Main (MHM) nickel sulphide ore deposits, and the generally low-volume high-grade nickel sulphide deposit associated with the Yilgarn

Craton province. In common with these deposits is their small size, complexity, and inability to be characterized properly from the surface due to low resolution. With the selected deposits, a number of depositional scenarios and CSR geometries were considered to optimize imaging of underground structures. This is accompanied by appropriate parametrisation of Kirchhoff pre-stack depth migration (PSDM).

With the McLeay nickel sulphide ore deposit, the plausibility of the CSR method has been established by comparing its numerical investigation results for a known ultramafic-basalt (UM-basalt) interface and a steeply dipping fault structure, associated with McLeay magmatic nickel sulphide ore deposit, with the counterpart numerical test results obtained by means of the well-established multiple offset VSP (MVSP) method. As presented in Figure 4-12, the initial numerical simulation MVSP data of the UM-basalt interface itself has been compared with the field result of same rock interface. Comparative MVSP and CSR PSDM results were shown in Figure 4-20, Figure 4-21, and Figure 4-22. Results compared favourably. The extent of CSR image is found to be marginally shorter in comparison to MVSP but the CSR image is in much better agreement with the geology for the fully populated receiver borehole (in Figure 4-21). As shown in Figure 4-22, the fault zone is much better reconstructed with CSR method. Imaging artefacts are much smaller for CSR results. The above study offers the first appreciable insight to the imaging capability of the CSR method in a complex, steeply dipping environment.

For CSR numerical test of MHM deposit style imaging, two scenarios of nickel sulphide mineralized zones were considered. Model 1 considered the real deposition model where both the disseminated and massive nickel sulphides were present and Model 2 considered the situation where the disseminated nickel sulphide zone was entirely replaced by the massive nickel sulphides. Model 2 was built with the purpose to examine if any amplitude differences could be detected related to different ore concentrations. The PSDM results were presented in Figure 5-9. The numerical test results show that while the dips of vertical ore-bodies are preserved, their locations are misplaced. The ore-body imaged is largely displaced to the left of the corresponding geology. Clearly, this geological model presents a challenge for crosshole imaging as conducted in this study. It was also observed that amplitude reflections differences are very subtle. As such, it will be difficult to target massive

sulphides in MHM hard rock type environment with CSR approach base only on amplitude reflections attributes. Practically, additional geophysical and geological information are needed for better interpretation of such results. For such deposit, in the real field case, we would require good knowledge of the rock properties and precise velocity field for imaging. Using a precise velocity field for migration may mitigate the misplaced imaging error.

To test CSR imaging capability on MHN ore deposit style, four different cases were considered involving forward and reverse shooting crosshole geometries (as defined in this thesis), different borehole separations for the forward crosshole shooting geometry, and different borehole locations relative to the ore-body (location). The PSDM results of the first three cases were displayed and compared in Figure 5-14 and Figure 4-15. All the geometries provided image recovery more up-dip than down-dip of the ore-body. It was observed that image recovery is not the same for crosshole reciprocity geometries though both geometries provided satisfactory results. It is also realized from the test results that the limit of target surface area and, in particular, depth recovery of MHN nickel ore deposit style is to a large extent influenced by receiver borehole location. A greater depth image recovery is realized when the receiver borehole is located down-slope the target. Figure 5-17 presented the result of the MHN ore deposit with the fourth case CSR boreholes geometry when the borehole pairs were located far down-slope the target with the receiver borehole arbitrary located. A substantial surface area including the entire down-dip part of the ore-body has been imaged. From the results, significance amplitude reflections differences exist between the ore-body and the surrounding rocks. As such, it will be possible to target massive sulphide ore deposits in MHN hard rock type environment with CSR approach base highly on amplitude reflection attributes. The numerical test results also demonstrate that to obtain substantial depth recovery of such steeply dipping structures requires boreholes location at far down-slope part of the target. Also, from these results, forward shooting borehole geometry should be the preferred choice for target depth recovery in brown fields.

To investigate the potential of the CSR method to delineate Rosebery complex ore lenses, the seismic response of Rosebery ground conditions was first tested by using a part of VMS elongated ore lens. This test was also meant to examine the effect of

different shot point densities and borehole geometry on the CSR imaging capability in terms of image recovery and its extent. The PSDM image superimposed with the geology section was presented in Figure 6-9. The long lateral and vertical extensions of the elongated VMS ore deposit and the mine foot-wall contact have well been delineated and the image correlated well with the corresponding geology. Results in Figure 6-10 show that under normal circumstances, a relatively coarse shot density points could provide high-resolution images comparable to relatively dense shot point separations. Thus, with CSR, large shot spacing can strike a balance between data quality and, therefore, provision of high-resolution image and cost of survey. Figure 6-11 compared the CSR images, for two scenarios, scenarios 1 and 2, for borehole separations of 100 and 200 m respectively. In scenario 2, the receiver borehole was moved from its original position in scenario 1 to 100 m down-slope the VMS ore lens. Despite the increase in borehole separation both images are of a high quality. By using a far-offset down-slope receiver borehole a more down plunge part of target between the boreholes was imaged. Increase in borehole separation, however, brings a corresponding artefact into the migration section.

Subsequently, synthetic data and PSDM image were obtained for the deeper theoretically unknown ore lens and result compared with that of a real data. The synthetic PSDM image compared favourably with a real data pre-stack time migration (PSTM) image extracted from a 3D cube over the study area as shown Figure 6-17. The CSR method was then used to image and delineate cluster of the VMS ore lenses as well as the host rock boundaries. The ore lenses imaged have their depths and dips accurately represented and correlated well with the superimposed geologic section. This result was shown in Figure 6-24. The host rock boundaries imaged also have the depth and dip preserved and mapped and contoured the geologic section to a high degree of accuracy. Strong reflected amplitude, as expected from the high reflectivity ore lenses, was the seismic attribute used to identify the delineated ore lenses. Result presented in Figure 6-23 shows that by stacking images of individual pairs of boreholes, CSR imaging is capable of recovering extremely fine and complex geological features of Rosebery-like VMS ore lenses at depth and over extensive lateral coverage.

Except the Maggie Hays Main nickel sulphide deposit, where the mineralization was imaged with some imprecision, all the PSDM images obtained mapped and contoured the known geological structures to a high degree of accuracy and preserved their depths and dips. Thus, in favourable conditions, the CSR technique is capable of delineating complex images beyond the reach of any other geophysical method. The image quality improves with optimum borehole geometry and carefully designed acquisition parameters, both of which can be assessed through modelling. Clearly, extensive modelling studies need to precede any field data acquisition if CSR is to be optimally utilized for resolving underground geology.

7.2. Discussions

Slim-line borehole seismic receiver tools are now available coupled with the advent of the hydrophone string for hard rock conventional VSP application. The use of Distributed Acoustic Sensing (DAS) is becoming more frequent. However, one major problem with adoption of borehole-to-borehole seismology relates to seismic source, its deployment, particularly for hard rock exploration considering also the diameter of the borehole and the potential damage of the borehole walls coming from the seismic sources. Though the solution to the problem is far from over, through advancing technology a variety of impulsive and controlled frequency downhole sources are now available for use.

The synthetic data generated in this work, assumed particle displacement amplitudes similar to that recorded by a geophone. For practical purposes, the choice between sensitive broadband pressure sensors and particle motion sensors may need to be decided upon by considering the borehole diameter, weight, cost, deployable rapidity, repeatability, and, more so, the wave components to be collected. Implementation of CSR and imaging results are controlled by many different factors. Some of these factors have been tested in this work and others can only be properly evaluated through the future field studies.

In VSP geometry, reflections can originate from either side of the borehole. This is not the case in surface seismic. The paradox of the origins of reflections within a VSP profile as illustrated by Greenwood (2013) is that, given the same VSP shot and

receiver geometry, a geologic dip of say 45° gives a very similar reflection response (shape and angle) as that of an opposite -75° geologic dip. However, in VSP survey, one can help resolve directionality with walk-away's or radial surveys. Crosshole surveys are essentially multiple offset or walk-away VSP surveys. It is further possible to add another borehole which will help determine directionality and exclude offline reflectors. Crosshole geometry, when rotated, can be liken to surface seismic. The simple illustrations of reflection points origination I performed in crosshole geometry does not give credence to the ambiguity observed with VSP geometry. Further studies, however, is needed to investigate this.

Geometry of boreholes with respect to the geometry of the target is of a crucial importance for image formation and spatial delineation of ore-body. An attractive proposition includes multiple boreholes where a multi plane image formation may be accomplished. Similarly, virtual crossholes surveys are of additional interest particularly with the future development of the DAS equipment.

Tomographic inversion of a crosshole survey suffers from limited ray coverage. Therefore, in CSR data acquisition, it is recommended to place surface geophones, wherever possible, to improve the reliability of tomographic velocity recovery which in turn will facilitate CSR imaging.

In real data collection where slim-line hydrophone string will be used, tube-waves could be affecting the data quality. One way to resolve this issue is to have borehole receivers closely spaced so that tube waves can be removed by digital filtering. Greenwood (2013) suggested a preferable (1-2 m) spacing of hydrophones for VSP data collection to prevent aliasing of tube-waves. This is worth considering in hydrophone CSR survey. In dealing with tube-waves, the non-standard wavefield separation method (Greenwood, 2013) employed to remove strong coherent tube-wave noise or the digital filtering techniques (Li, 1994) for suppressing strong tube-waves can be considered.

Field interpretation of CSR results would benefit from integration with other geophysical methods and available geological information. Of particular importance for parametrisation and evaluation of CSR image is the availability of surface

seismic 3D images. It is unlikely that CSR method will be implemented prior to 3D surface seismic.

In this research, I have limited current analysis at a qualitative level where the result is overlain onto the true geological model while the errors are visually estimated and commented. In future studies it may be beneficial to quantify these errors.

Optimal imaging parameters are quite vital for the imaging quality but also quite sensitive to the geological structures. In case of real field acquisition where the geological structures are unknown these parameters can be determined by:

1. Preferential slope: A good starting point is priori knowledge from geological data and can be tested with different migration slope panels either side of this looking at when primary reflectors become continuous, linear, and less smiley. In other words, it can be tested with different migration slope panels with restricted apertures to search for aligning reflectors.
2. Aperture: Should be restricted to a Fresnel zone for best results.
3. Geometry: Clearly, holes don't need to be deeper than the target. Rather, relatively large source aperture and long receiver array length are required as imaging is primarily up-dip. Simple ray diagram illustration demonstrates that for dipping reflectors, near bottom shot points may contribute more to reflector area recovery nearer to the borehole whereas more reflector surface area recovery, especially the up-dip part of the structure, may be obtained with up-located shot points. Also from simple ray diagram illustration and from CSR numerical results, depth recovery requires (receiver) borehole located far down-slope the target.

7.3. Conclusions

Extensive CSR numerical tests conducted with complex synthetic models and, where possible, compared with field results suggest that this technique could be of exceptional value in specific geological and mining situations. CSR data processing and migration can make use of the already existing software developed for surface and VSP data processing. The importance of the proper parametrisation for imaging cannot be overestimated. This is particularly true for CSR since even small

imprecision in image formation when using ultra high frequencies signals are likely to produce smeared images and numerous artefacts. The model parametrisation and imaging optimization are intrinsic components of CSR method. Hence petro-physical information must be available prior to application of either modelling or field studies. The CSR method also requires significant a priori knowledge of the underground geology in order to optimize acquisition geometry for the given set of boreholes. Thus, CSR method is best applied in well advanced brown fields when further mine extensions and discoveries of the satellite ore-bodies are a must.

Synthetic modelling with CSR demonstrated that even a single pair of boreholes can be, in some cases, used to produce depth images of exceptional quality and thus high value to mining. Utilization of multiple boreholes is modelled to show that such approach can be effective in recovery of underground geology of exceptional complexity. Hence CSR method has very high exploration power and high potential for producing new discoveries. These observations were made possible only after extensive numerical tests conducted on carefully designed models that were parametrised using a priori knowledge of the selected well-known mineral deposits. Only then it was possible to prove that CSR imaging can precisely delineate complex geological structures and recover correctly their depths and dips away from the inter-borehole space.

Extensive numerical tests further show that the image quality, resolution and spatial accuracy are dependent on several factors. These are summarized below:

- Borehole separation relative to the dip of the mineralized structure
- Number of boreholes available
- Position of boreholes with respect to the target
- Choice of source and receiver borehole
- Source and receiver density
- Borehole length and deviation
- Accuracy of the model geometry and parametrisation
- Pre-processing and imaging approach

The above factors determine the image extent and the image quality for the given choice of source. Consequently, it is necessary that any crosshole survey is preceded

by the extensive modelling study which will aim to optimize not only the acquisition stage but also the outcome.

The CSR method could be a cost-effective approach applicable especially in situations where: drilling is costly; the drill-hole may not have intersected a target of interest located at depth; dense vegetation and difficult terrain restrict mobility for conventional seismic methods application; delineation of steeply dipping ore-bearing structures buried deeply under highly attenuating heterogeneous regolith is required; and in situations where other geophysical methods are non-deterministic. Unfortunately, CSR case studies are very rare. The existing results or the available literature were clearly not sufficiently intriguing to inspire mining industry to utilize this method more frequently for helping resolve complex mining objectives. This is why I have embarked on this research with the main quest of proving that CSR method has potential to be routinely used in brown-field exploration. The CSR method can only mature if used and evaluated properly. This is why my research investigated all aspects of CSR method and documented its strengths and potential weaknesses through extensive numerical studies based on real field situations.

To the best of my knowledge, this is the first comprehensive attempt of such kind and I hope that the application of the CSR method presented in this study will form the basis for future work in adopting and perfecting this method for mineral exploration purposes. My objective for conducting this work was to produce a step forward in understanding and adopting crosshole approach as a valuable tool for exploration. It is my expectation that the thoughts developed herein will be developed further and integrated into the hard rock exploration tool box for exploring specific types of ore deposit. And may it be so.

7.4. Future work

My study encompassed certain aspects of CRS method. However, more research is required for the technique to establish itself on the exploration stage. Further work and directions for crosshole surveys are proposed below:

- Conduct more elastic modelling experiments to evaluate the potential of shear waves including the combination of P and S images and velocities for rock characterization
- Utilize crosshole and VSP derived velocity fields to improve accuracy of PSDM crosshole data image. That is, utilize both transmitted and reflected wavefields
- Conduct Full Waveform Inversion tests on numerical then on field data. This novel methodology should be effective with crosshole data due to intrinsically high SNR of crosshole surveys as well as high quality starting velocity model
- Further developments of crosshole sources is of a critical importance for the implementation of this method in the cases where we have deep and complex ore-bodies and we cannot possibly hope to delineate them by any other method
- Inclusion of DAS into crosshole surveys is likely to be a key for the future of this highly promising methodology
- Interferometric studies including surface sources are also highly potent for future imaging improvements

References

Anderson, N., and S. Cardimona, 2002, Forward seismic modeling: The key to understanding reflection seismic and ground penetrating radar (GPR) techniques: Presented at the 2nd Annual Conference on the Application of Geophysical and NDT Methodologies to Transportation Facilities and Infrastructure held in Los Angeles, CA, USA.

Azcue, J. M., 1999, Environmental Impacts of Mining Activities: Emphasis on Mitigation and Remedial Measures: Springer-Verlag Berlin Heidelberg,.

Bakulin, A., and R. Calvert, 2004, Virtual source: new method for imaging and 4D below complex overburden: Presented at the SEG Annual Meeting, Society of Exploration Geophysicists.

Bakulin, A., and R. Calvert, 2006, The virtual source method: Theory and case study: Geophysics, **71**, SI139-SI150.

Balch, A. H., and M. W. E. Lee, 1984, Vertical Seismic Profiling: Technique, Applications, and Case Histories: D. Reidel Publishing Company.

Bancroft, J. C., 2007, A Practical Understanding of Pre-and Poststack Migrations: Prestack: Soc of Exploration Geophysicists.

Barnes, S. J., and C. S. Perring, 2007, Komatiite-hosted nickel sulfide deposits: geology, geochemistry, and genesis: SPECIAL PUBLICATION-SOCIETY OF ECONOMIC GEOLOGISTS, **13**, 51.

Bell, F. G., and L. J. Donnelly, 2006, Mining and its impact on the Environment: Taylor & Francis Group.

Berry, R. F., 1990, Structure of the Rosebery deposit: Structure and Mineralisation of Western Tasmania, 17-26.

Berry, R. F., and R. A. Keele, 1997, Cambrian tectonics and mineralization in western Tasmania: International Mining Geology Conference, 3rd, Launceston, November 1997, Australasian Institute of Mining and Metallurgy, Proceedings: Presented at the International Mining Geology Conference.

Birch, F., 1961, The velocity of compressional waves in rocks to 10 kilobars, part 2: Journal of Geophysical Research, **66**, 2199-2224.

Blackburn, J., J. Daniels, S. Dingwall, G. Hampden-Smith, S. Leaney, J. Le Calvez, L. Nutt, H. Menkiti, A. Sanchez, and M. Schinelli, 2007, Borehole Seismic Surveys: Beyond the Vertical Profile: Journal Oil Field Review, Schlumberger, **15**, 20-35.

Bois, P., M. La Porte, M. Lavergne, and G. Thomas, 1972, Well-to-well seismic measurements: Geophysics, **37**, 471-480.

Bording, R. P., and L. R. Lines, 1997, Seismic modeling and imaging with the complete wave equation: Soc of Exploration Geophysicists.

Bradley, J., 1956, The geology of the west coast range of Tasmania: Pt. II: Presented at the Papers and Proceedings of the Royal Society of Tasmania.

Brathwaite, R. L., 1972, The structure of the Rosebery ore deposits, Tasmania: Presented at the Australasian Institute of Mining and Metallurgy.

Brathwaite, R. L., 1974, The geology and origin of the Rosebery ore deposit, Tasmania: Economic Geology, **69**, 1086-1101.

Buck, P. S., S. A. Vallance, C. S. Perring, R. E. T. Hill, and S. J. Barnes, 1996, Geology of the Maggie Hays komatiitic nickel sulphide deposit, Western

Australia: in Grimsey, E.J. and Neuss, I., Eds., Nickel'96 Mineral to Market: Austral. Inst. Min. Metall., **96**, 111-120.

Buck, P. S., S. A. Vallance, C. S. Perring, R. E. T. Hill, and S. J. Barnes, 1998, Maggie Hays nickel deposit: Geology of Australian and Papua New Guinean mineral deposits: Melbourne, Australian Institute of Mining and Metallurgy, 357-364.

Cai, W., and G. Schuster, 1993, Processing Friendswood cross-well seismic data for reflection imaging: Presented at the 63th SEG Ann. Intern. Mtg: Expanded Abstracts, Washington, DC.

Campbell, G., 1990, The seismic revolution in gold and platinum prospecting: South African Geophysical Association Yearbook, 37-45.

Campbell, G., and J. H. Crotty, 1990, 3-D seismic mapping for mine planning purposes at the South Deep Prospect: in D. A. J. Ross-Watt, and P. D. K. Robinson, eds., Proceedings International Deep Mining Conference: SAIMM Symposium Series S1O,, **2**, 569-597.

Cao, S., and S. Greenhalgh, 1995, High-resolution seismic tomographic delineation of ore deposits: Exploration Geophysics, **26**, 315-318.

Carcione, J. M., G. C. Herman, and A. Ten Kroode, 2002, Seismic modeling: Geophysics, **67**, 1304-1325.

Cassidy, K. F., D. C. Champion, B. Krapez, M. E. Barley, S. J. A. Brown, R. S. Blewett, P. B. Groenewald, and I. M. Tyler, 2006, A revised geological framework for the Yilgarn Craton, Western Australia: Geological Survey of Western Australia, Record, **8**.

Chabot, L., D. C. Henley, R. J. Brown, and J. C. Bancroft, 2002, Single-well seismic imaging using full waveform sonic data: An update: SEG Int'l Exposition and 72nd Annual Meeting.

Cheraghi, S., A. Malehmir, and G. Bellefleur, 2011, 2D seismic reflection imaging in the Brunswick no. 6 massive sulphide and iron deposits, Bathurst Mining Camp, Canada: Implications for crustal architecture and mineral potential: Tectonophysics, **506**, 55-72.

Christie, P., D. Ireson, J. Rutherford, A. Hess, N. Smith, K. Dodds, L. Johnston, and J. Schaffner, 1995, Borehole seismic data sharpen the reservoir image: Oilfield Review, **4**, 18-31.

Claerbout, J. F., 1971, Toward a unified theory of reflector mapping: Geophysics, **36**, 467-481.

Claerbout, J. F., 1985, Imaging the earth's interior: Blackwell Scientific Publications: London.

Corbett, K. D., 1981, Stratigraphy and mineralization in the Mt. Read Volcanics, western Tasmania: Economic Geology, **76**, 209-230.

Corbett, K. D., K. O. Reid, E. B. Corbett, G. R. Green, K. Wells, and N. W. Sheppard, 1974, The Mount Read Volcanics and Cambrian-Ordovician relationships at Queenstown, Tasmania: Presented at the Journal of the Geological Society of Australia, Taylor & Francis.

Cosma, C., L. Balu, and N. Enescu, 2010, 3D VSP migration by image point transform: Geophysics, **75**, S121-S130.

Cosma, C., and N. Enescu, 2003, Ore delineation by crosshole seismics, transmission and reflection imaging at Voisey's Bay, Canada: The 7th International Symposium on Recent Advances in Exploration Geophysics (RAEG 2003).

Cosma, C., N. Enescu, E. Adam, and L. Balu, 2002, Vertical and horizontal seismic profiling investigations at Olkiluoto, 2001: Posiva Report.

Cosma, C., A. Wolmarans, D. Eichenberg, and N. Enescu, 2007, Kimberlite Delineation by Seismic Side-scans from Boreholes: Exploration in the New Millennium: Proceedings of the Fifth Decennial International Conference on Mineral exploration.

Deans, S. R., 1983, The Radon transform and some of its applications: John Wiley and Sons, Inc.

Dillon, P. B., and R. C. Thomson, 1984, Offset Source Vsp Surveys and Their Image RECONSTRUCTION*: Geophysical Prospecting, **32**, 790-811.

Dillon, P. B., 1988, Vertical seismic profile migration using the Kirchhoff integral: Geophysics, **53**, 786-799.

Dragoset, B., 2005, A historical reflection on reflections: The leading edge, **24**, 46-70.

Drummond, B. J., B. R. Goleby, A. Owen, A. Yeates, C. Swager, Y. Zhang, and J. Jackson, 2000, Seismic reflection imaging of mineral systems: Three case histories: Geophysics, **65**, 1852-1861.

Eaton, D. W., B. Milkereit, and M. Salisbury, 2003, Hardrock Seismic Exploration: Society of Exploration Geophysicists.

Emerson, D., 1995, Petrophysical results on Maggie Hays core samples: Notes to Maggie Hays Nickel NL.

Enescu, N., C. Cosma, and L. Balu, 2003, Seismic VSP and crosshole investigations in Olkiluoto, 2002: Working Report, **13**.

Evans, L. R., 2009, Groundwaters in wet, temperate, mountainous, sulphide-mining districts: delineation of modern fluid flow and predictive modelling for mine closure (Rosebery, Tasmania), University of Tasmania.

French, W. S., 1975, Computer migration of oblique seismic reflection profiles: Geophysics, **40**, 961-980.

Fullagar, P. K., G. N. Fallon, P. J. Hatherly, and D. W. Emerson, 1996, AMIRA Project P436 Final Report—Implementation of Geophysics at Metalliferous Mines, Centre for Mining Technology and Equipment Report: MM1-96/11.

Fullagar, P. K., G. N. Fallon, P. J. Hatherly, and D. W. Emerson, 1996a, Implementation of Geophysics at Metalliferous Mines: Application of Geophysics to Mine Planning and Operations, Stage II - Testing of Existing Technology, AMIRA Project P436 Final Report, CMTE Report No. MM1-96/11.

Gower, C. F., and J. A. Bunting, 1976, Lake Johnston, Western Australia, 1: 250 000 geological series explanatory notes: Sheet SI/51-01, Bureau of Mineral Resources and Geological Survey of Western Australia, Perth.

Green, A. G., and J. A. Mair, 1983, Subhorizontal fractures in a granitic pluton: Their detection and implications for radioactive waste disposal: Geophysics, **48**, 1428-1449.

Green, G. R., 1976, The environment of massive sulphide ore deposition at Rosebery, Tasmania [abs.]: Internat. Geol. Cong., 25th, Sydney, **1**, 163.

Green, G. R., 1983, The geological setting and formation of the Rosebery volcanic hosted massive sulphide orebody, Tasmania: Unpublised PhD. thesis University of Tasmania, Hobart, Australia.

Green, G. R., and G. D. Iliff, 1989, Rosebery: Geological Society of Australia Special Publication 15.

Green, G. R., M. Solomon, and J. L. Walshe, 1981, The formation of the volcanic-hosted massive sulfide ore deposit at Rosebery, Tasmania: Economic Geology, **76**, 304-338.

Greenhalgh, S., B. Zhou, and S. Cao, 2003, A crosswell seismic experiment for nickel sulphide exploration: Journal of applied geophysics, **53**, 77-89.

Greenhalgh, S. A., I. M. Mason, and C. Sinadinovski, 2000, In-mine seismic delineation of mineralization and rock structure: Geophysics, **65**, 1908-1919.

Greenwood, A., 2013, Application of Vertical Seismic Profiling for the characterisation of hard rock: PhD, Curtin University.

Greenwood, A., C. Dupuis, A. Hashemi, and M. Urosevic, 2010, Hydrophone VSP Imaging in the Agnew Wiluna Belt, Western Australia: Presented at the ASEG Extended Abstracts.

Greenwood, A., C. J. Dupuis, M. Urosevic, and A. Kepic, 2012, Hydrophone VSP surveys in hard rock Geophysics 77(5), **5**, WC223-WC234.

Greenwood, A., F. Menu, and M. S. Hossain, 2014, Full Waveform Sonic (FWS) Logging Lightning Nickel Surface Drill Hole LNSD-063 for Independence Group, IGO NL, (Report). .

Gyorfi, I., Z. Hajnal, D. White, E. Takacs, B. Reilkoff, I. Annesley, B. Powell, and R. Koch, 2007, High-resolution seismic survey from the McArthur River region: Contributions to mapping of the complex P2 uranium ore zone, Athabasca Basin, Saskatchewan: BULLETIN-GEOLOGICAL SURVEY OF CANADA, **588**, 397.

Hall, G., and M. Solomon, 1962, Metallic mineral deposits: Journal of the Geological Society of Australia, **9**, 285-309.

Hannington, M. D., C. D. J. de Ronde, and S. Petersen, 2005, Sea-floor tectonics and submarine hydrothermal systems. In: (Eds. Hedenquist, J. W., Thompson, J. F. H., Goldfarb, R. J., and Richards, J. P.) Economic Geology 100th Anniversary Volume, 111-141.

Hardage, B. A., 1983, Vertical Seismic Profiling. Part A: Principles: Geophysical Press Limited.

Hardage, B. A., 1992, Crosswell Seismology & Reverse VSP: Geophysical Press Ltd.

Harrison, C., and M. Urosevic, 2008, Towards Direct Detection of Gold Bearing Rock Formations From Seismic Data: St. Ives Gold Camp, Western Australia: Presented at the 2008 SEG Annual Meeting.

Harrison, C. B., 2009, Feasibility of Rock Characterization for Mineral Exploration Using Seismic Data: PhD, Curtin Unversity of Tecnology.

Haslett, M. J., 1994, The South Deep Project: geology and planning for the future: Presented at the Proceedings XVth CMMI Congress.

Hatherly, P. J., M. Urosevic, A. Lambert, and B. J. Evans, 1994, A simple approach to calculating refraction statics corrections: Geophysics, **59**, 156-160.

Heggie, G. J., 2010, The application of platinum group elements in komatiite-hosted nickel sulfide exploration: Ph.D, Western Australia.

Heggie, G. J., M. L. Fiorentini, S. J. Barnes, and M. E. Barley, 2012, Maggie Hays Ni Deposit: Part 1. Stratigraphic Controls on the Style of Komatiite Emplacement in the 2.9 Ga Lake Johnston Greenstone Belt, Yilgarn Craton, Western Australia: Economic Geology, **107**, 797-816.

Herman, G. T., 1980, Image Reeconstruction From Projections: The Fundamentals of Computerized Tomography: Academic Press.

Hinds, R. C., N. L. Anderson, and R. D. Kuzmiski, 1996, VSP Interpretive Processing: Theory and Practice: Society of Exploration Geophysicists.

HiSeis Pty Ltd, 2010, Seismic Reflection for Nickel Sulphides in Greenstone Terranes.

Hornby, B. E., 1989, Imaging of near-borehole structure using full-waveform sonic data: Geophysics, **54**, 747-757.

Huston, D. L., and R. R. Large, 1988, Distribution, mineralogy, and geochemistry of gold and silver in the north end orebody, Rosebery, Tasmania: Economic Geology, **83**, 1181-1192.

Independent Group NL, 2013, Annual Report. http://www.igo.com.au/irm/content/annual-report1.aspx?RID=509.

Independent Group NL, 2014, Annual Report. http://www.igo.com.au/irm/content/annual-report1.aspx?RID=509.

Joly, A., J. Miller, C. Stott, T. McCuaig, and M. Duguet, 2008, Unravelling the Maggie Hays and Emily Ann nickel sulphide deposits via a multidisciplinary study of the Archaean Lake Johnston Greenstone Belt, Yilgarn Craton, Western Australia: Presented at the AGU Fall Meeting Abstracts.

Juhlin, C., 1995, Imaging of fracture zones in the Finnsjön area, central Sweden, using the seismic reflection method: Geophysics, **60**, 66-75.

Juhlin, C., S. Kashubin, J. Knapp, V. Makovsky, and T. Ryberg, 1995, EUROPROBE seismic reflectionprofiling in the Urals: The ESRU project.

Juhlin, C., J. Lindgren, and B. Collini, 1991, Interpretation of seismic reflection and borehole data from Precambrian rocks in the Dala Sandstone area, central Sweden: First Break, **9**.

Juhlin, C., and H. Palm, 1999, 3-D structure below Ävrö Island from high-resolution reflection seismic studies, southeastern Sweden: Geophysics, **64**, 662-667.

Keary, P., and M. Brooks, 1991, An Introduction to Geophysical Exploration: Blackwell Scientific Publications.

Kinkela, J., A. Dzunic, M. Urosevic, R. MacRae, and L. Webb, 2014, Seismic Exploration for Volcanogenic Massive Sulphides-The Rosebery Zinc, Lead, Copper Mine, Tasmania: Presented at the 76th EAGE Conference and Exhibition-Workshops.

Kukkonen, I. T., 2011a, Outokumpu deep drilling project 2003-2010: Geological Survey of Finland, Special paper.

Kukkonen, I. T., P. Heikkinen, S. Heinonen, and J. Laitinen, 2011b, Reflection seismics in exploration for mineral deposits: Initial results from the HIRE project: Geoscience for society: 125th anniversary volume: Geological Survey of Finland, 49-58.

Kukkonen, I. T., and R. Lahtinen, 2006, Finnish reflection experiment FIRE 2001-2005: Geological survey of Finland.

Large, R., R. Allen, M. Blake, and W. Herrmann, 1998, Alteration halo model for the Rosebery VHMS deposit, Western Tasmania: Studies of VHMS-related alteration: geochemical and mineralogical vectors to ore, 1.

Large, R. R., 1990, The gold-rich sea-floor massive sulfide deposits of Tasmania: Geologische Rundshau, **79**, p. 256–278.

Large, R. R., 1992, Australian volcanic-hosted massive sulfide deposits; features, styles, and genetic models: Economic Geology, **87**, 471-510.

Large, R. R., R. L. Allen, M. D. Blake, and W. Herrmann, 2001, Hydrothermal alteration and volatile element halos for the Rosebery K lens volcanic-hosted

massive sulfide deposit, western Tasmania: Economic Geology, **96**, 1055-1072.

Larroque, M., J. Postel, M. Slabbert, and W. Duweke, 2002, How 3D seismic can help enhance mining: First Break, **20**.

Li, G., 1994, Crosswell Seismic Processing: Automatic Velocity Analysis, Filtering, and Reflection Imaging: MSc, Calgary, Alberta, Canada.

Lines, L., 1991, Applications of tomography to borehole and reflection seismology: The Leading Edge, **10**, 11-17.

Loftus-Hills, C. L., 1915, The Zinc-lead Sulphide Deposits of the Read-Rosebery District: Part II: Rosebery Group:: Tasmania Geological Survey Bull., no. 23, Department of Mines.

Loftus-Hills, G., M. Solomon, and R. J. Hall, 1967, The structure of the bedded rocks west of Rosebery, Tasmania: Journal of the Geological Society of Australia, **14**, 333-337.

Malehmir, A., and G. Bellefleur, 2010, Reflection seismic imaging and physical properties of base-metal and associated iron deposits in the Bathurst Mining Camp, New Brunswick, Canada: Ore Geology Reviews, **38**, 319-333.

Malehmir, A., R. Durrheim, G. Bellefleur, M. Urosevic, C. Juhlin, D. J. White, B. Milkereit, and G. Campbell, 2012, Seismic methods in mineral exploration and mine planning: A general overview of past and present case histories and a look into the future: Geophysics, **77**, WC173-WC190.

Mari, J., F. Huguet, J. Meunier, and M. Becquey, 2011, Natural Gas Storage Seismic Monitoring: Oil & Gas Science and Technology–Revue d'IFP Energies nouvelles, **66**, 9-20.

Mari, J. L., and F. Coppens, 2003, WELL SEISMIC SURVEYING: Editions Technip.

Matthews, L., 2002, Base metal exploration: Looking deeper and adding value with seismic data: CSEG recorder, **27**, 37-43.

McDonal, F., F. Angona, R. Mills, R. Sengbush, R. Van Nostrand, and J. White, 1958, Attenuation of shear and compressional waves in Pierre shale: Geophysics, **23**, 421-439.

Meng, F., and J. McGaughey, 1996, Ore body hunting with crosswell imaging methods: Presented at the 1996 SEG Annual Meeting, Society of Exploration Geophysicists.

Meyers, J., and M. Uroservic, 2007, Experimental 2D high-resolution seismic data acquisition and processing at the Prospero-Tapinos Nickel Project, Western Australia: For Jubilee Mines NL.

Milkereit, B., E. K. Berrer, A. R. King, A. H. Watts, B. Roberts, E. Adam, D. W. Eaton, J. Wu, and M. H. Salisbury, 2000, Development of 3-D seismic exploration technology for deep nickel-copper deposits-A case history from the Sudbury basin, Canada: Geophysics, **65**, 1890-1899.

Milkereit, B., D. Eaton, J. Wu, G. Perron, M. H. Salisbury, E. K. Berrer, and G. Morrison, 1996, Seismic imaging of massive sulfide deposits; Part II, Reflection seismic profiling: Economic Geology, **91**, 829-834.

Mussett, A. E., and M. Aftab-Khan, 2009, LOOKING INTO THE EARTH: An Introduction to geological Geophysics: Cambridge University Press, USA.

Nafe, J. E., and C. L. Drake, 1963, Physical properties of marine sediments, The sea:, Interscience publishers.

Park, C. B., R. D. Miller, D. W. Steeples, and R. A. Black, 1996, Swept Impact Seismic Technique (SIST): Geophysics, **61**, 1789-1803.

Peters, B., and P. Buck, 2000, The Maggie Hays and Emily Ann nickel deposits, Western Australia: a geophysical case history: Exploration Geophysics, **31**, 210-221.

Petersen, S., and J. R. Hein, 2013, The geology of sea-floor massive sulphides.

Petrie, L., and M. Salisbury, 2003, Seismic exploration of the Manitouwadge greenstone belt, Ontario: A case history: Hardrock seismic exploration, 110.

Pretorius, C. C., G. K. Chunnett, T. W. J. Chalke, and M. Gibson, 1997, 3D data integration for Exploration and Mine Planning: Proceeding of Exploration '97, 399-408.

Pretorius, C. C., M. A. Gibson, and Q. Snyman, 2011, Development of high resolution 3D vertical seismic profiles: Journal of the South African Institute of Mining and Metallurgy, **111**, 117.

Pretorius, C. C., A. A. Jamison, and C. Irons, 1989, Seismic exploration in the Witwatersrand basin, Republic of South Africa: Presented at the Proceedings of Exploration.

Pretorius, C. C., M. R. Muller, M. Larroque, and C. Wilkins, 2003, A review of 16 years of hard rock seismics on the Kaapvaal Craton, in Eaton, D.W., B. Milkereit, and M. H. Salisbury, eds., Hard rock seismic exploration: SEG, 247–268., SEG.

Qin, F., and G. T. Schuster, 1993, Constrained Kirchhoff migration of crosswell seismic data: 63th Ann. Internat. Mtg. Soc. Expl. Geophys., 99-102.

Ricker, N., 1953, The form and laws of propagation of seismic wavelets: Geophysics, **18**, 10-40.

Robein, E., 2010, Seismic imaging: A Review of the Techniques. their Principles. Merits and Limitations. EAGE.

Roberts, B., E. Zaleski, G. Perron, F. Adam, L. Petrie, and M. Salisbury, 2003, Seismic exploration of the Manitouwadge Greenstone Belt, Ontario: A Case History.

Rowbotham, P. S., and N. R. Goulty, 1993, Imaging capability of cross-hole seismic reflection surveys: Geophysical Prospecting, **41**.

Rutledge, J. T., 1989, Interwell seismic surveying workshop: An overview: The Leading Edge, **8**, 38-38.

Salisbury, M., and D. Snyder, 2007, Application of seismic methods to mineral exploration: Mineral deposits of Canada: A synthesis of major deposit types, district metallogeny, the evolution of geological provinces, and exploration methods: Geological Association of Canada, Mineral Deposits Division, Special Publication, **5**, 971-982.

Salisbury, M. H., C. W. Harvey, and L. Matthews, 2003, The acoustic properties of ores and host rocks in hardrock terranes: Hardrock seismic exploration, 9-19.

Salisbury, M. H., B. Milkereit, G. Ascough, R. Adair, L. Matthews, D. R. Schmitt, J. Mwenifumbo, D. W. Eaton, and J. Wu, 2000, Physical properties and seismic imaging of massive sulfides: Geophysics, **65**, 1882-1889.

Salisbury, M. H., B. Milkereit, and W. Bleeker, 1996, Seismic imaging of massive sulfide deposits; Part I, Rock properties: Economic Geology, **91**, 821-828.

Schodde, R., 2011, Recent trends in Australian exploration: Presented at the presentation to the AMEC Convention.

Seymour, D. B., G. R. Green, and C. R. Calver, 2007, The Geology and Mineral Deposits of Tasmania: a summary, Tasmanian Geological Survey, Bulletin 72.

Sheriff, R. E., 1978, A First Course in Geophysical Exploration and Interpretation: International Human Resources Development Corporation.

Sheriff, R. E., and L. P. Geldart, 1995, Exploration Seismology: Cambridge University Press.

Solomon, M., 1964, The spilite-keratophyre association of West Tasmania and the ore deposits at Mt. Lyell: Risebery and Hercules: Unpubl. PhD. thesis, University of Tasmania.

Solomon, M., F. Tornos, R. R. Large, J. N. P. Badham, R. A. Both, and K. Zaw, 2004, Zn–Pb–Cu volcanic-hosted massive sulphide deposits: criteria for distinguishing brine pool-type from black smoker-type sulphide deposition: Ore Geology Reviews, **25**, 259-283.

Solomon, M., F. Vokes, and J. Walshe, 1987, Chemical remobilization of volcanic-hosted sulphide deposits at Rosebery and Mt. Lyell, Tasmania: Ore Geology Reviews, **2**, 173-190.

Solomon, M., and J. L. Walshe, 1979, The formation of massive sulfide deposits on the sea floor: Economic Geology, **74**, 797-813.

Stewart, R. R., 1991, Exploration Seismic Tomography: Fundamentals: Society of Exploration Geophysicists.

Stolz, E., M. Urosevic, and K. Connors, 2004, Reflection seismic surveys at St Ives gold mine, WA: ASEG Extended Abstracts, 1-4.

Stuart, G. W., S. J. Jolley, L. G. B. T. Polome, and R. F. Tucker, 2000, Application of 3-D seismic attributes analysis to mine planning: Target gold deposit, South Africa: The Leading Edge, **19**, 736-742.

Swager, C., 1997, Tectono-stratigraphy of late Archaean greenstone terranes in the southern Eastern Goldfields, Western Australia: Precambrian Research, **83**, 11-42.

Telford, W. M., L. P. Geldart, and R. E. Sheriff, 1990, Applied Geophysics: Cambridge University Press.

Turner, G., T. Craske, A. Kepic, E. Stolz, and M. Urosevic, 2007, Seismic reflection surveys to assist nickel and gold exploration in the WA goldfields: ASEG Extended Abstracts, **2007**, 1-5.

Urosevic, M., S. Ziramov, R. Pevzner, A. Kepic, A. Egorov, J. Kinkela, D. Pridmore, and J. Dwyer, 2017, Seismic for mineral resources - a mainstream method of the future: Presented at the Decennial Mineral Exploration Conferences, Exploration 17, Toronto Canada.

Urosevic, M., 2000, A study of seismic wave propagation as applied to seismic imaging in the Southern Sydney Basin: PhD, Curtin University of Technology.

Urosevic, M., G. Bhat, and M. H. Grochau, 2012, Targeting nickel sulfide deposits from 3D seismicreflection data at Kambalda, Australia: Geophysics, **77**, WC123-WC132.

Urosevic, M., A. Bona, S. Ziramov, R. Martin, J. Dwyer, and A. Foley, 2018, Reflection seismic with DAS, why and where?: Presented at the Conference and Exhibition, Near Surface Geoscience 2018.

Urosevic, M., and B. J. Evans, 2007, Feasibility of seismic methods for imaging gold deposits in Western Australia: Minerals and Energy Research Institute of Western Australia.

Urosevic, M., B. J. Evans, and P. J. Hatherly, 1992, The improvement in seismic resolution by map and trace attribute analysis: Exploration Geophysics, **23**, 387-392.

Urosevic, M., A. Kepic, E. Stolz, and C. Juhlin, 2007, Seismic exploration of ore deposits in Western Australia: Presented at the Exploration in the new millennium: Proceedings of the Fifth Decennial International Conference on Mineral Exploration.

Urosevic, M., N. Stoltz, and S. Massey, 2005, Seismic Exploration for Gold in a Hard Rock Environment–Yilgarn Craton, Western Australia: 67th EAGE Conference & Exhibition.

Urosevic, M., S. Ziramov, J. Kinkela, J. Dwyer, and D. Pridmore, 2016, Seismic Exploration of Mineral Resources-An Australian Perspective: Presented at the Near Surface Geoscience 2016-First Conference on Geophysics for Mineral Exploration and Mining.

Van Schaack, M. A., and J. C. Costa, 1996, XSP-CDP mapping in complex media without raytracing: Presented at the 1996 SEG Annual Meeting, Society of Exploration Geophysicists.

Wang, Q., L. Schi⊘tte, and I. Campbell, 1996, Geochronological constraints on the age of komatiites and nickel mineralisation in the Lake Johnston greenstone belt, Yilgarn Craton, Western Australia: Australian Journal of Earth Sciences, **43**, 381-385.

White, D., D. Secord, and M. Malinowski, 2012, 3D seismic imaging of volcanogenic massive sulfide deposits in the Flin Flon mining camp, Canada: Part 1—Seismic results: Geophysics, **77**, WC47-WC58.

White, D. J., B. A. Kjarsgaard, C. J. Mwenifumbo, and G. Buffett, 2007, Seismic delineation of the Orion South (140/141) kimberlite Fort a la Corne Field, Saskatchewan: Presented at the Exploration 07: Fifth Decennial International Conference on Mineral Exploration; Toronto; CA; Sept 9-12, 2007.

Widess, M. B., 1973, How thin is a thin bed?: Geophysics, **38**, 1176-1180.

Wiggins, J. W., 1984, Kirchhoff integral extrapolation and migration of nonplanar data: Geophysics, **49**, 1239-1248.

Wiggins, W., P. Ng, and A. Manzur, 1986, The Relation Between the VSP-CDP Transformation And VSP Migration: Presented at the SEG Annual Meeting.

Williams, P., M. Urosevic, A. Kepic, and M. Whitford, 2012, Recent experience with use of high definition seismic reflection for nickel sulphide exploration in Western Australia: Presented at the 74th EAGE Conference and Exhibition incorporating EUROPEC 2012.

Williams, P. K., 2001, Exploration for Conductive Nickel Sulphide bodies under cover - recent Australian experiences: Presented at the SEG.

Williams, P. K., M. Urosevic, A. Kepic, M. Whitford, and E. Stolz, 2012, Seismic methods for hard rock mineral exploration; 34th IGC Brisbane

Wong, J., 2000, Crosshole seismic imaging for sulfide orebody delineation near Sudbury, Ontario, Canada: Geophysics, **65**, 1900-1907.

Wong, J., N. Bregman, G. West, and P. Hurley, 1987, Cross-hole seismic scanning and tomography: The Leading Edge, **6**, 36-41.

Wright, C., J. A. Wright, and J. Hall, 1994, Seismic reflection techniques for base metal exploration in eastern Canada: examples from Buchans, Newfoundland: Journal of applied geophysics, **32**, 105-116.

Wright, P. M., 1981, Seismic methods in mineral exploration: Economic Geology, 863-870.

Wyatt, K. D., and S. B. Wyatt, 1981, The determination of subsurface structural information using the vertical seismic profile: Presented at the 51st Annual International Meeting.

Wyllie, M. R. J., A. R. Gregory, and G. H. F. Gardner, 1958, An experimental investigation of factors affecting elastic wave velocities in porous media: Geophysics, **23**, 459-493.
Yilmaz, Ö., 1987, Seismic Data Processing: Investgations in Geophysics: Society of Exploration Geophysicists.
Yilmaz, Ö., 2001, Seismic Data Analysis: Processing, Inversion, and Interpretation of Seismic Data.: Society of Exploration Geophysicists.

Appendix A

Borehole sources and receivers - a recall

Since the onset of the reverse vertical seismic profiling (RVSP) and crosswell tomography, different downhole sources and downhole receivers have been used. For example, dynamite and borehole wall clamped 3-component geophones were used to study the form and laws of propagation of seismic wavelets (Ricker, 1953), to investigate the attenuation effect of compressional and shear waves in the subsurface rocks (McDonal et al., 1958), and for performing crosswell seismic measurements to deduce velocity structure between the boreholes in attempt to locate oil reservoirs (Bois et al., 1972). Detonating downhole seismic source and a 24-channel hydrophone streamer were deployed in crosshole tomography to delineate ore lodes (Cao and Greenhalgh, 1995). The McConnell crosshole data set collected in Ontario, Canada, to delineate the boundaries of an interwell ore-body by traveltime tomogram and migration image employed hydrophone receivers and explosive sources (Meng and MCGaughey, 1996). Field testing of borehole sparker with array of hydrophones has been carried out at an ultramafic-hosted nickel prospect near Widgemooltha, Western Australia, and output signal compared with that produced by a seismic detonator borehole energy source under the same conditions (Bierbaum and Greenhalgh, 1998). Again, Greenhalgh et al. (2000) used a detonating downhole seismic source and a slim-line multi-element hydrophone array string and 3C geophone sensors for both their crosshole tomography and VSP reflection imaging test survey at the underground Hunt mine in Kambalda, Western Australia. Wong (2000) applied a non-destructive piezoceramic vibrator source and high-sensitivity hydrophone detectors for his crosshole seismic tomography imaging of the McConnell ore-body near Sudbury, Ontario, Canada. With three pairs of near vertical diamond drill-holes, Cosma and Enescu (2003) deployed a piezoelectric source and a string of 24 hydrophones for p-wave velocity tomography and crosshole reflection surveys for inter-borehole imaging of massive Ni-Cu sulphide mineralization at Voisey's Bay, Labrador, Canada. The reflection imaging technique was based on the Image Point (IP) transform referred to in the main body of thesis.

Downhole sensors and slim-line hydrophones have been further used for other intentions with associated levels of success. For example, in New Brunswick Canada, 3C-VSP was trialled at the Half-mile Lake massive sulphide deposit to test the viability of VSP for imaging a known ore-body (Bellefleur et al., 2004). Other applications were implemented in Western Australia by Greenwood et al. (2010) and Greenwood et al. (2012) and in South Africa by Pretorius et al. (2011) and were mentioned in Section 1.5.

The developing of downhole seismic sources involves service companies, government research laboratories, research departments of specially major oil companies, and entrepreneurs (Hardage, 1992). Examples of downhole seismic sources include coupled cord downhole seismic source (Omnes, 1990), low-frequency drill bit seismic while drilling (Radtke et al., 2009), electrodes arc discharge or borehole sparkers (Mahrer and Zook, 1993; Rechtien et al., 1993; Dyer and Baria, 1996), and VIBSIST SPH54 – a piezoelectric borehole source based on the Swept Impact Seismic Technique (SIST) that produces signals with levels of energy comparable to explosives (Park et al., 1996; Cosma and Enescu, 2003). Li (1994) captured some trialled experiments done in North America by some major oil companies with different downhole sources and receivers utilizing different borehole geometries with the main purpose of testing downhole seismic sources and receivers.

The application and further developments of the above mentioned borehole seismic energy sources and alternative seismic energy sources are captured by other authors and researchers such as Kramer et al. (1969), Hardage (1992), and Heigl et al. (2012). Hardage (1992) classified the downhole seismic sources as impulsive – which includes explosives, sparker, water gun, air gun, perforating gun, weight drop, and drill bit –, and controlled frequency – which includes resonant cavity, vibrator, and piezoelectric transducers. There are many downhole seismic sources available.

Generally, downhole seismic energy sources have sufficient bandwidth and high power output (Hardage, 1992; Rechtien et al., 1993). In particular, the downhole sparker source can be configured to generate acoustic signals with peak frequencies from 2 to far over 1000 Hz with high power up to 1000 Joules (Baria et al., 1989; Heigl et al., 2012). Such relatively broad bandwidth is suitable for high-resolution

short-spaced borehole-to-borehole data acquisition as well as capable of transmitting sufficient energy over long distances in borehole-to-borehole geometry (Baria et al., 1989; Omnes, 1990; Bierbaum and Greenhalgh, 1998; Heigl et al., 2012).

To select which type of downhole seismic source should be used for real data acquisition, two important and interrelated considerations should be: the distance the source signal may travel (two way travel – from the source to the target and the reflected waves from the target to the receivers) and the kind of spatial resolution the data must prove (Hardage, 1992). If the target of interest is small and if source-target-receiver paths are relatively short, then usually it implies a high spatial resolution is required so that small features can be resolved. On the other hand, if a measurement involves only long travel paths, then a lower spatial resolution is acceptable which implies only sizeable features are to be detected. In many cases, the situation may lie in-between the two and there must be some sort of balance. In the various case histories analyzed, considering the targets of interest and the distance the source signal may travel, the source wavelet I used has central frequency varying from 80 Hz to 120 Hz depending on each case study.

In collection of synthetic data in this research, string of receivers in the form of slim-line hydrophones is used with user defined receiver spacing. For practical purposes, however, the choice between sensitive broadband pressure sensors, which are slim-line hydrophones, and particle motion sensors, which are slim-line components shuttle sensors, may need to be decided. And when deciding, there is the need to consider factors such as the borehole diameter, weight, cost, rapidly deployable, repeatability, and the wave components to be collected.

Even-though downhole seismic sources are built to provide sufficient energy for high-resolution inter-borehole imaging, the general requirements met by such downhole seismic sources suffice for CSR imaging. As envisaged and provided in this research, for mainly steeply dipping massive sulphide ore-bearing structures of interest, the CSR method will be capable of obtaining high-resolution images tens to hundreds of metres of such ore-bearing structures up-dip of/away from the exploration boreholes as well as providing high-resolution images of small-volume, high density ore deposits. Thus, target of interest should inform us of the downhole

seismic source to employ to give the necessary amount of energy sufficient to meet the expected requirements.

With reference to Omnes (1990), Hardage (1992), Bierbaum and Greenhalgh (1998), and Heigl et al. (2012), downhole seismic sources must meet the following requirements if they are to be adopted for routine borehole seismic surveys.

1. Sufficient bandwidth: the high frequencies beyond the general limits for surface seismic reflection data acquisition are required for borehole-to-borehole acquisition to take advantage of the capability of transmitting moderate frequencies over relatively long distances beyond the borehole walls and high frequencies for high-resolution inter-borehole imaging in a crosshole configuration.
2. Applicable in different lithologies: it will be advantageous if a downhole seismic energy source has adjustable bandwidth which can be fine-tuned to different lithologies.
3. Sufficient energy: it should be possible to produce a sufficient SNR within an affordable time interval.
4. No damage should be caused to the well (formations, cement, casing): the well or the cementing or both can easily be damaged especially with explosive source. It may be advisable, in some cases, to operate before cementing the borehole wall.
5. Cost efficient: for reasons of cost-efficiency, a sufficient number of source stations should be covered before the need to remove the device from the well.
6. The diameter of the device should be adequate for operations in most boreholes. (The diameter of diamond core drill holes which are typically drilled with HQ – 96 mm, NQ – 76 mm, and BQ – 61 mm has been one of the initial setbacks to the application of borehole seismology for ore and mineral exploration).
7. Reliability of source: the seismic energy source must be reliable for the data acquisition.
8. Repeatability of signal: signal generated at all shot points need to be identical and should remain so should shooting at a point is repeated. Also, if the source could enable wavelet repeatability of multiple shots at a single source, it will lead to data quality.
9. Controllability from the surface.
10. Directionality to focus the acoustic energy to where it is needed.

References

Baria, R., P. D. Jackson, and D. M. McCann, 1989, Further development of a high-frequency seismic source for use in boreholes: Presented at the Geophysical Prospecting.

Bellefleur, G., L. Matthews, B. Roberts, B. McMonnies, M. Salisbury, G. Perron, D. Snyder, and J. McGaughey, 2004, Downhole seismic imaging of the Victor kimberlite, James Bay Lowlands, Canada: A feasibility study: Presented at the 2004 SEG Annual Meeting, Society of Exploration Geophysicists.

Bierbaum, S. J., and S. A. Greenhalgh, 1998, A high-frequency downhole sparker sound source for crosswell seismic surveying: Presented at the Exploration Geophysics.

Bois, P., M. La Porte, M. Lavergne, and G. Thomas, 1972, Well-to-well seismic measurements: Geophysics, **37**, 471-480.

Cao, S., and S. Greenhalgh, 1995, High-resolution seismic tomographic delineation of ore deposits: Exploration Geophysics, **26**, 315-318.

Cosma, C., and N. Enescu, 2003, Ore delineation by crosshole seismics, transmission and reflection imaging at Voisey's Bay, Canada: The 7th International Symposium on Recent Advances in Exploration Geophysics (RAEG 2003).

Dyer, B. C., and R. Baria, 1996, Development of the CSMA Mark II high temperature borehole sparker source: Scientific Drilling, v. 5: IODP.

Greenhalgh, S. A., I. M. Mason, and C. Sinadinovski, 2000, In-mine seismic delineation of mineralization and rock structure: Geophysics, **65**, 1908-1919.

Greenwood, A., C. Dupuis, A. Hashemi, and M. Urosevic, 2010, Hydrophone VSP Imaging in the Agnew Wiluna Belt, Western Australia: ASEG Extended Abstracts, **2010**, 1-4.

Greenwood, A., C. J. Dupuis, M. Urosevic, and A. Kepic, 2012, Hydrophone VSP surveys in hard rock Geophysics 77(5), **5**, WC223-WC234.

Hardage, B. A., 1992, Crosswell Seismology & Reverse VSP: Geophysical Press Ltd.

Heigl, W. M., R. P. Radtke, R. H. Stokes, and D. A. Glowka, 2012, Development of a Downhole Sparker Source With Adjustable Frequencies: Presented at the 2012 SEG Annual Meeting, Society of Exploration Geophysicists.

Kramer, F., R. Peterson, and W. Walter, 1969, Seismic energy sources: Proceedings Offshore Technology Conference: Paper.

Li, G., 1994, Crosswell Seismic Processing: Automatic Velocity Analysis, Filtering, and Reflection Imaging: MSc, Calgary, Alberta, Canada.

Mahrer, K. D., and B. J. Zook, 1993, A field test of an electrodeless arc discharge, borehole seismic source: Geophysics, **58**, 1558-1564.

McDonal, F., F. Angona, R. Mills, R. Sengbush, R. Van Nostrand, and J. White, 1958, Attenuation of shear and compressional waves in Pierre shale: Geophysics, **23**, 421-439.

Omnes, G., 1990, Experimental study of the coupled cord downhole seismic source: Presented at the Expanded. Abstracts, Paper BG6.

Park, C. B., R. D. Miller, D. W. Steeples, and R. A. Black, 1996, Swept impact seismic technique (SIST): Geophysics, **61**, 1789-1803.

Pretorius, C. C., M. A. Gibson, and Q. Snyman, 2011, Development of high resolution 3D vertical seismic profiles: Journal of the South African Institute of Mining and Metallurgy, **111**, 117.

Radtke, R. P., J. E. Fontenot, D. A. Glowka, and R. H. Stokes, 2009, Low-frequency drill bit seismic while drilling: Proceedings Offshore Technology Conference: Paper.

Rechtien, R. D., K. L. Hambacker, and R. F. Ballard Jr, 1993, A high-frequency sparker source for the borehole environment: Geophysics, **58**, 660-669.

Ricker, N., 1953, The form and laws of propagation of seismic wavelets: Geophysics, **18**, 10-40.

Wong, J., 2000, Crosshole seismic imaging for sulfide orebody delineation near Sudbury, Ontario, Canada: Geophysics, **65**, 1900-1907.

Appendix B

Rayleigh's and Ricker's limit of resolution

In optics, Rayleigh states that the capability of an optical instrument to distinguish separate images of objects that are lying close together reaches its limit when the two diffracted images are separated by a distance equal to the peak-to-trough distance of the instrument's diffraction pattern (Jenkins and White, 1957). The two diffracted images cannot be resolved when their distance apart is below this limit. This statement is often referred to as Rayleigh's criterion for optical instrument resolution and the limit for resolution has much in common with the Ricker's limit of resolution of a seismic wavelet.

In 1953, Ricker studied the composite waveform as a function of separation. In a diffraction pattern, a point exhibits a central maximum point and, thus, two near points exhibit two central maxima points. As separation between these points decreases, the central maxima exhibit two lesser peaks and will finally merge into single major peak with no subsidiary maximum. Ricker (1953) chose the limit of resolvability as that separation at which the composite waveform has a zero curvature, also called a flat spot, at its central maximum. Any two points with separation less than this limit become unresolved. For a convolving wavelet, a flat spot condition is said to occur when two spikes – a reflection spike similar to a source point in optical analogy – are separated by a distance equal to the separation between the inflexion points on central maximum or lobe of the convolving wavelet (Kallweit and Wood, 1982).

The above can be directly related to the frequency content for vertical resolution of acquired data. The smaller the source frequency, the longer the wavelength of waves generated. Long wavelength wavelets have long interval of separation between the inflexion points of the convolving wavelet and hence the lesser the resolving capability of geologic features. On the other hand, very high-frequency shot-wavelength wavelets, as can be generated with crosshole geometry, have very short interval separating the inflexion points and are therefore capable to resolve small geologic features.

Figure B.1 shows the relationship between Rayleigh's criterion for optical instrument resolution and Ricker's criterion for seismic vertical resolution.

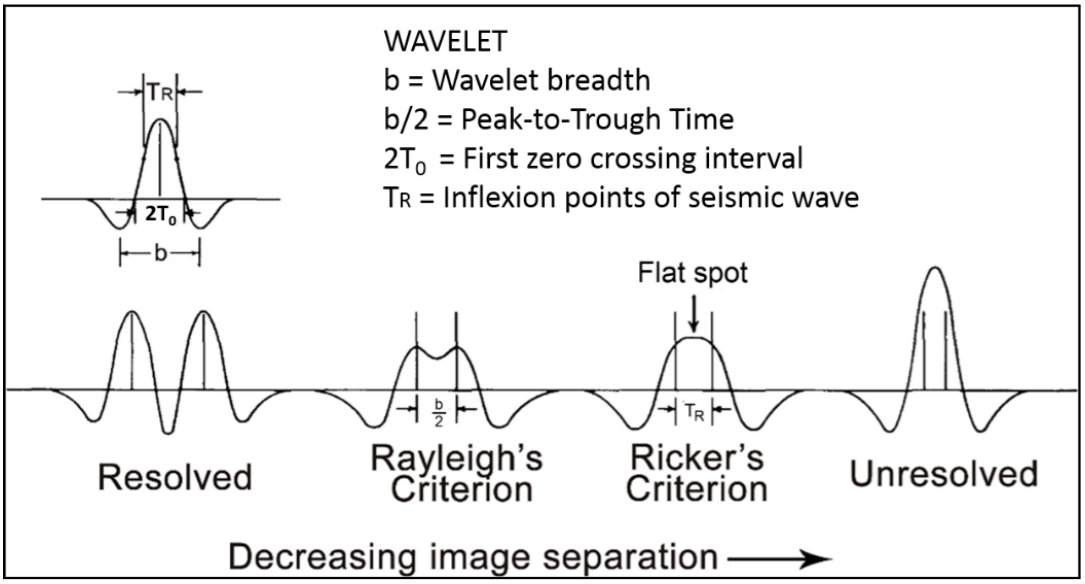

Figure B. 1. Rayleigh's limit of optical resolution and Ricker's limit of seismic vertical resolution. Rayleigh's limit occurs when images are separated by the peak-to-trough time interval; Ricker's limit occurs when the closely spaced images are separated by time interval equals to the separation between the inflexion points (after Kallweit and Wood (1982)).

The limitations of the vertical resolution also depend on the thickness of the layers. By Ricker's criteria, a layer with thickness less than the first zero-crossing interval of the wavelet cannot be resolved (Kallweit and Wood, 1982). Target of interest delineation with seismic reflection techniques depends on the vertical and horizontal resolution capability of seismic. The added advantage of the crosshole seismic geometry over surface seismic and conventional VSP techniques for vertical and horizontal resolution of ore-bearing structures, of even low-volume but high-grade ore deposits, at depth are discussed in Subsection 2.1.1.

References

Jenkins, F. A., and H. E. White, 1957, Fundamentals of optics: Tata McGraw-Hill Education.

Kallweit, R. S., and L. C. Wood, 1982, The limits of resolution of zero-phase wavelets: Geophysics, **47**, 1035-1046.

Ricker, N., 1953, Wavelet contraction, wavelet expansion, and the control of seismic resolution: Geophysics, **18**, 769-792.